

BLDSC no:- DX 208630



**Pilkington Library**

Author/Filing Title ..... Lovkos, G.I.

Accession/Copy No. 040160839

Vol. No. ....	Class Mark .....
---------------	------------------

~~Loan copy~~

~~25 JUN 1999~~

**FOR REFERENCE ONLY**

0401608395



BADMINTON PRESS  
UNIT 1 BROOK ST  
SYSTEM  
LEICESTER LE7 1GD  
ENGLAND  
TEL 0116 260 2917  
FAX 0116 269 6639



**PROPAGATION CHARACTERISTICS OF CYLINDRICAL FREQUENCY  
SELECTIVE GUIDES**

by


**Georgios I. Loukos, Diploma, M.Sc.**

**A Doctoral Thesis**

Submitted in partial fulfilment for the requirements for the award of the degree of  
Doctor of Philosophy of Loughborough University

September 1997

© by G. Loukos 1997

 Loughborough University Pitt Rivers Library
Date <u>May 98</u>
Class
Acc No. <u>040160839</u>

V0630534

To all the people I have missed

The social condition does not apply, the boundary condition does

## ABSTRACT

Recent experimental investigation on FSS arrays forming waveguides (FSGs) and horns showed that incident electromagnetic energy can be guided and radiated at specific frequencies. This thesis aims to provide the theoretical understanding of the waves propagating inside a cylindrical FSS waveguide. With immediate applications on horn antennas the research deals with cylindrical guides, made entirely from double periodic arrays. The theoretical analysis begins as a standard electromagnetic boundary value problem. The formulated system of algebraic equations is solved either for the complex propagation constant, by an iterative procedure or, for the fields. The analysis makes use of the Floquet modal expansion, the current representation as a set of sub-domain basis functions and the Method of Moments. Initially, the thesis is concerned with single periodic structures, which is a special case to the analysis. The efficiency of the model to provide stable and valid results is examined. Next the elements are finite dipoles. The effects of the dipole resonance to the propagating and radiating characteristics of the FSS is closely investigated. Other aspects include the effects of the periodicity and the element size. The investigation concludes with an FSG with square loop elements. Validation of the results for some designs is made by comparison with measured data.

## ACKNOWLEDGMENTS

I wish to express my gratitude to my supervisor Dr. J.C. Vardaxoglou, for his guidance and his continuous encouragement throughout this research project. His ideas, his experience and managing of the research work within the Antennas Group have been outstanding and I would like to wish him further success in his work.

I would like to acknowledge the financial support of my fees and research expenses by EPSRC.

The measurements at the finishing stage of the project were conducted by Mr J. Eade, to whom I am thankful for. Many wishes and good luck on propelling this research to the next stage.

I am thankful to Dr. D. Trincherio and the people at Polytecnico di Torino for their collaboration in the publishing of joint papers and their hospitality.

I would also like to thank my friends and research students in the Antennas Group especially, N. Tilemma, M. Jaywardene, J. Eade and Anoosh; not forgetting Juan and my dearest Ourani.

Finally, I express my gratefulness to my parents for their constant support of any kind throughout the period of my studies.



## CONTENTS

### CHAPTER 1

#### INTRODUCTION

1.1.1 Introduction to Frequency Selective Surfaces (FSS)	1
1.1.2 Introduction to Frequency Selective Guides (FSG)	2
1.1.3 Introduction to Leaky Wave Antennas	4
1.2 Structure of the thesis	5
<i>References</i>	7

### CHAPTER 2

#### ANALYSIS OF A CYLINDRICAL PERIODIC OPEN WAVEGUIDE

2.1 Introduction	11
2.2 Cylindrical periodic structures (FSGs)	15
2.3 Floquet modal description	16
2.4 Field expansions	19
2.5 The Method of Moments	27
2.5.1 Sub-domain basis functions	27
2.5.2 Roof-top functions in the Method of Moments	29
2.6 Deriving a solution	35
2.7 Complex roots introduced in open periodic structures	35
2.7.1 On the choice of the transverse wavenumber $k_{\rho q}$	36
2.8 Deriving the fields	39
2.9 Numerical considerations	41
2.10 Conclusions	42
<i>References</i>	43

### CHAPTER 3

#### CYLINDRICAL FSG - ONE DIMENSIONAL CASE

3.1 Introduction	46
3.2 Longitudinal geometry	47
3.2.1 The 1-D analysis	48
3.2.2 Solving for the real propagation constant	51
3.2.3 Calculation of the fields	53
3.2.4 The 2-D model on a single periodic FSG	55
3.2.4.1 Predicted results for complex waves	56
3.2.5 The highly attenuated EH modes	58
3.2.6 Checking of boundary condition	59
3.3 Transverse geometry	61
3.3.1 The 1-D analysis	62

3.3.2 Solving for the real propagation constant	63
3.3.3 Complex waves inside the FSG	64
3.3.4 Field patterns for transverse geometry	66
3.4 Conclusions	67
<i>References</i>	68

## CHAPTER 4

### CYLINDRICAL FSG WITH DIPOLE ELEMENTS

4.1 Introduction	69
4.2 FSG with $\phi$ -dipoles	71
4.2.1 Roof-top functions and convergence tests	72
4.2.2 Numerical results for representative array	73
4.2.3 The dipole array as a leaky wave antenna	77
4.2.4 Parametric study on $\phi$ -dipole arrays	78
4.3 FSG with z-dipoles	90
4.3.1 Roof-top functions and convergence ratios	91
4.3.2 Numerical results for representative arrays	91
4.3.3 The grating lobes	95
4.4 Closing remarks	97
<i>References</i>	99

## CHAPTER 5

### CYLINDRICAL FSG WITH SQUARE LOOP ELEMENTS

5.1 Introduction	100
5.2 Square loop geometry	101
5.3 Current functions on the square loop	102
5.4 Numerical results for representative arrays	106
5.4.1 Boundary condition checking	112
5.4.2 The hybrid factor	114
5.4.3 Square loop results compared with results from dipole arrays	116
5.4.4 Square loop array with different periodicity	117
5.4.5 Measured results	120
5.5 Conclusions	123
<i>References</i>	124

<b>CHAPTER 6</b>	
<b>CONCLUSIONS AND FUTURE CONSIDERATIONS</b>	125
<b>APPENDICES</b>	
<b>APPENDIX A: General wave analysis in cylindrical; coordinates: an overview</b>	130
<i>References</i>	132
<b>APPENDIX B Grating lobes and mode coupling effect</b>	133
<i>References</i>	134
<b>APPENDIX C Asymptotic expansions for Bessel</b>	135
<i>References</i>	139

# CHAPTER 1

## Introduction

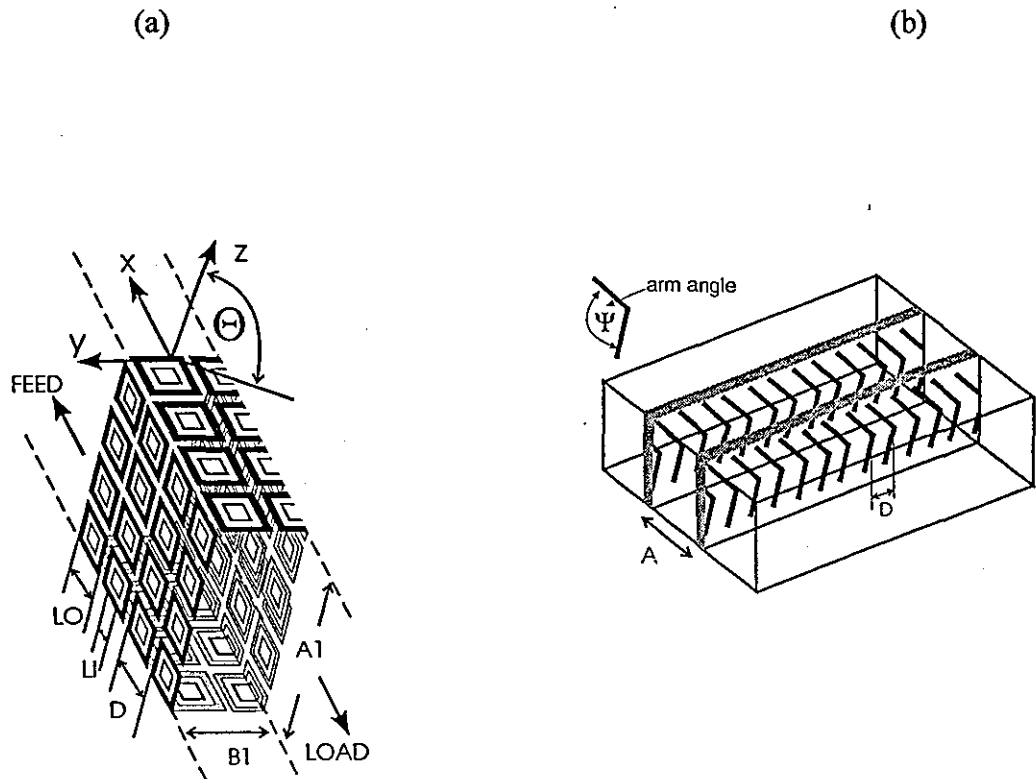
### *1.1.1 Introduction to Frequency Selective Surfaces (FSS)*

FSSs are essentially array structures which consist of a plurality of resonant conducting elements (or apertures), often printed on a dielectric for support. The elementary principle of operation of FSS is, that they exhibit bandstop or bandpass properties when excited with an incident electromagnetic wave. Planar and curved FSS have found applications as antenna components in reflector or sub-reflector systems for dual band operation and beam shapers. The frequencies at which the bandstop or bandpass phenomena occur, are usually dictated by the element and

lattice geometry. Planar FSS have been extensively analysed, see for example [1-6], and their attractive properties have been well established both in academic research and microwave industry.

### 1.1.2 Introduction to Frequency Selective Guides (FSG)

The Antennas and Microwave Group at Loughborough University, has been investigating the properties of FSS both theoretically and experimentally. Novel contributions arising from the said group include Frequency Selective Guides (FSGs) and Frequency Selective Horns (FSHs). Fig. 1 depicts an FSG with double squares [7], a waveguide with the array inserts [8, 9], and an FSH [10].



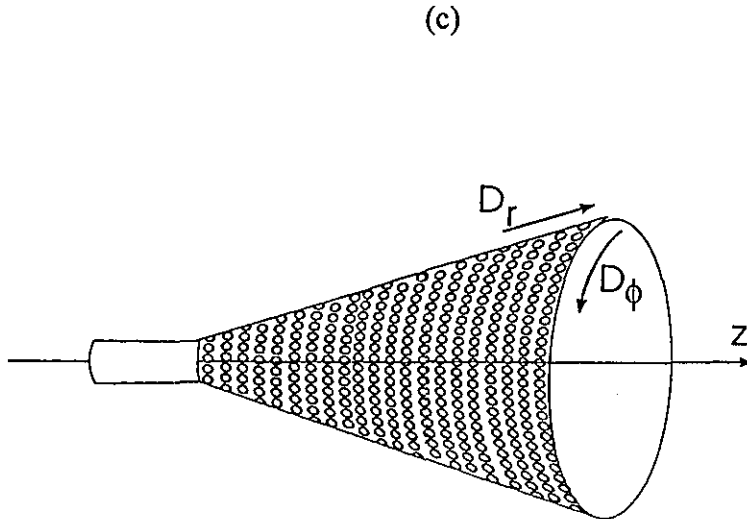


Figure 1: Various FSS geometries: a) Frequency Selective Guide, b) waveguide with array inserts, c) Frequency Selective Horn.

Frequency Selective Waveguides (FSGs), as the name suggests, are waveguides which embody the general properties of Frequency Selective Surfaces (FSSs). In principle they take the shape and size of traditional rectangular or cylindrical waveguides, but their walls are replaced by an FSS. For the rectangular hollow tube of Fig. 1.a., measured data revealed frequencies of guidance and radiation [7]. In collaborating study with the Politecnico di Torino, results from the geometry in Fig. 1.b using a transverse resonance model, agreed well with measurements conducted at Loughborough [8,9].

Due to their ease in fabrication and their performance Frequency Selective Horns (FSHs), find many applications where, lightweight and inherent multiband capabilities are desired (e. g. conical radomes). The lightweight soft horn can be easily fabricated by wrapping a planar section of printed dielectric. At the resonant

frequency the performance is very close to that of a metallic wall while, away from resonance the horn becomes inert [10]. A multiband structure results by collocating two soft horns coaxially; the outer horn dictating the low frequency operation and the inner horn the high frequency. The integration of FSHs into image processing for medical diagnostics is underway by the referred group [11-13].

The most salient feature of the FSGs and FSHs is that electromagnetic energy can be guided inside an open structure due to the element resonance. Horns with cylindrical cross section are relatively easy to make. This thesis aims to provide the theoretical analysis and modelling, as well as explain the main operation properties of FSGs with circular cross section. The impetus behind the present study came from two factors:

1. Lack of the mode content of FSGs  
and,
2. Design features of FSGs

### ***1.1.3 Introduction to Leaky Wave Antennas***

So, what if electromagnetic energy is launched into an FSS that is formed as a waveguide? Is energy going to propagate by some sort of mode configuration, will it leak through? Undoubtedly, some will leak through at some frequencies since the guide is not closed. The latter lead to the introduction of another well known type of antenna family, '*leaky wave antennas*'. Historically, they are first mentioned in the early '30s, but their existence was questioned until Marcuvitz supplied a mathematical interpretation of leaky waves in 1956 [14,15]. Since then, as Oliner notes [14], the leaky wave theory played a significant role in the explanation of many physical effects e.g. radiation from plasma sheaths surrounding vehicles re-entering the atmosphere, blind spots in the radiation from large phased arrays, grating coupling and Wood's anomalies in integrated optics. A large number of the

leaky wave antennas result from open waveguides [16-30]. One class of these leaky wave structures involves periodic modulations on a dielectric, the modulations due to grooves in the dielectric or metallic strips printed on it.

## *1.2 Structure of the thesis*

This thesis is organised as follows:

In Chapter 2 the contribution is a method which provides the characteristic equation for doubly periodic cylindrical arrays. The solution of this equation yields the propagation constants of all possible modes existing inside the FSG. Initially, Maxwell's equations are used to provide the field solutions for a wave excited inside a cylindrical FSG structure. Based on the assumption that the structure is infinite in the axial direction and has a natural periodicity of  $2\pi$ , the tangential electromagnetic field components are expressed as an infinite series of orthogonal wave functions, the Floquet modes. In order to account for the radiation from the open FSG, the wavenumbers are considered complex. The application of the boundary conditions enables the formation of the characteristic equation, where the unknown is the surface current. This equation is solved using the Method of Moments (MoM). Roof-top basis functions are used to expand the surface current.

Chapter 3 deals with one dimensional cases of cylindrical periodic arrays. Predicted results for the propagation constant are presented for free standing one dimensional arrays. Initially, the analysis is formulated, by collapsing the periodicity in one axis from the two dimensional analysis given in Chapter 2. The efficiency and the computational requirements of the computer model are discussed. Predicted results are presented for both the imaginary and the real part of the propagation constant. The results in this Chapter are useful in extracting the general set of rules of more complicated two dimensional geometries.



In Chapter 4, two examples of double periodic cylindrical guides are presented. The array elements are longitudinal and transverse resonant dipoles. The predicted propagation characteristics of the novel FSS guide, are presented by plotting the complex propagation constant. The convergence behaviour of the model is closely examined. Each mode configuration is identified and discussed. The effects of the dipole periodicity and length on the guide's propagation and radiation behaviour are studied.

In Chapter 5, double square loops are proposed as array elements. New interesting results regarding the complex wavenumbers are derived and presented for this FSG. The guiding and radiating properties of the square loop array are evaluated, by comparing the results with the dipole arrays shown in Chapter 4. The correspondence between the resonance and attenuation of the structure is discussed. Effects of the periodicity and element dimensions on the dominant mode are shown. The hybrid factor, which is a prime factor in designing balanced antenna feeds, is calculated and discussed. A representative design is also compared with measured data.

The conclusions and future work evolving from this thesis are presented in Chapter 6.

Finally, there are three Appendices included at the end of this thesis. Appentix A, briefly presents the standard wave analysis in cylindrical coordinates. Appentix B is concerned with two aspects common to open periodic antennas: the formation of radiating beams and the mode coupling effect. Finally, in Appendix C, asymptotic expressions are given for the Bessel functions used in the analysis.

### *References*

- [1] SCHENNUM, G. H.: 'Frequency selective surfaces for multiple frequency antennas', *Microwave J.*, Vol. 16, 1973, pp. 55-57.
- [2] AGRAWAL, V. D. and IMBRIALE, W. A.: 'Design of a dichroic casegrain subreflector', *IEEE Transactions on Antennas and Propagation*, Vol. AP-27, No. 4, July 1979, pp. 466-473.
- [3] ANDO, M., UENO, K., KUMAZAWA, H., and LAGOSHIMA, K.: 'AK/C/S bands satellite antenna with frequency selective surface', *Electronics and Communications in Japan*, Vol. 66-B, 1983, pp. 1665-1680.
- [4] COMTESSE, L. E., LANGLEY, R. J., PARKER, E. A., and VARDAXOGLU, J. C.: 'Frequency selective surfaces for dual and triple band offset reflector antennas', *Proc. 17<sup>th</sup> Microwave European Conference*, Rome, Sept. 1987, pp. 208-211.
- [5] VARDAXOGLU, J. C.: 'Frequency Selective Surfaces-analysis and design', 1997 Research Studies Press, Taunton, UK
- [6] CWIK, T. A.: 'Scattering from general periodic screens', Ph.D. thesis, University of Illinois at Urbana-Champaign, May, 1986.
- [7] ROBINSON, A. J., VARDAXOGLU, J. C, and SEAGER, R. D.: 'Waveguide guidance and radiation from a hollow tube formed from frequency-selective surfaces', *Electronics Letters*, 29, 1993, pp.1531-1533.
- [8] ORTA, R., TASCONE, R., TRINCHERO, D., LOUKOS, G. and VARDAXOGLU, J.C: 'Dispersion curves and modal fields of a waveguide with FSS inserts', *Electronics Letters*, 1995, 30, pp.1073-1074.
- [9] ORTA, R., TASCONE, R., TRINCHERO, D., LOUKOS, G. and VARDAXOGLU, J. C: 'Propagation Characteristics of Frequency Selective

Guides', Proceedings of the International Conference on Electromagnetics in Advanced Applications (ICEAA 95), Sep., Politecnico di Torino, Italy.

[10] VARDAXOGLU, J. C., SEAGER, R. D. and ROBINSON, A. J.: 'Novel soft horn antenna for multiband operation', Proc. IEE Colloquium on multiband Antennas, 1992, IEE Digest No: 1992/181, pp.4/1-4/6.

[11] VARDAXOGLU, J. C., LOUKOS, G. and SEAGER, R. D. 'Waveguiding Structures with FSS as side Walls', 1995, 23rd Automated and RF and Microwave Measurement Society, ARMMS Conference Digest, Windermere, Cambria.

[12] VARDAXOGLU, J. C. and LOUKOS, G.: 'Frequency Selective Horns', poster presentation in EPSRC's ITEC Conference '96, Leeds University, April '96.

[13] VARDAXOGLU, J. C., SEAGER, R. D., LOUKOS, G., JAYWARDENE, M.: 'Recent advances in frequency selective waveguides and horn antennas', Invited presentation, 1996, PIER's Conference in Innsbruck, Austria.

[14] OLINER, A. A.: 'Historical perspectives on microwave field theory', IEEE Trans. Microwave Theory Techniques, Vol. MTT-32, No 9, Sep. 1984, pp. 1022-1045.

[15] MARCUVITZ, N.: 'On field representations in terms of leaky wave modes or eigenmodes', IRE Trans. Antennas Propagation, Vol. AP-4, July 1956, pp.192-194.

[16] GOLDSTONE, O., and OLINER, A. A.: 'Leaky wave antennas I: Rectangular waveguides', IRE Trans. On Antennas and Propagation, Vol. Ap-7, Oct. 1959, pp.307-319.

[17] GOLDSTONE, O., and OLINER, A. A.: 'Leaky wave antennas II: Circular waveguides', IRE Trans. On Antennas and Propagation, Vol. 9, May 1961, pp.280-291.

- [18] MITTRA, R. and JONES, K. E.: 'Theoretical Brillouin ( $k$ - $\beta$ ) diagrams for monopole and dipole arrays and their application to log-periodic antennas', IEEE Trans. On Antennas Propagat., Vol. AP-12, Sept. 1964, pp.533-539.
- [19] SIGELMANN, R. A., and ISHIMARU, A.: 'Radiation from periodic structures excited by an aperiodic source', IEEE Trans. On Antennas Propagat., Vol. AP-13, May 1965, pp.354-364.
- [20] LI, R., C., M., OLINER, A., A.: 'Scattering resonances on a fast-wave structure', IEEE Trans. On Antennas Propagat., AP-13, No. 6, Nov. 1965, pp 948-959.
- [21] COLLIN, R. E. and ZUCKER, F. J. E.: 'Antenna Theory: Part 2', McGraw-Hill Book Company, New York 1969.
- [22] JACOBSEN, J.: 'Analytical, numerical, and experimental investigation of guided waves on a periodically strip-loaded dielectric slab', IEEE Trans. On Antennas Propagat., Vol. AP-18, No. 3, May 1970, pp. 379-388.
- [23] SCHWERING, F. and PENGH, S. T.: 'Design of dielectric grating antennas for millimeter wave applications', IEEE Trans. Microwave Theory Techniques, Vol. MTT-31, Feb. 1983, pp. 199-209.
- [24] MATSUMOTO, M., TSUTSUMI, M., and KUMAGAI, N.: 'Radial characteristics of a dielectric slab waveguide periodically loaded with thick metal strips', IEEE Trans. Microwave Theory Techniques, Vol. MTT-35, No. 2, Feb. 1987, pp. 89-95.
- [25] HADJICOSTAS, G., BUTLER, J. K., EVANS, G. A., CARLSON, N. W., and AMANTEA, R.: 'A numerical investigation of wave interactions in dielectric waveguides with periodic surface corrugations', IEEE J. of Quantum Electronics, Vol. 26, No. 5, May 1990, pp.893-902.

[26] ENCINAR, J. A.: 'Mode-matching and point-matching techniques applied to the analysis of metal-strip-loaded dielectric antennas', IEEE Trans. On Antennas Propagat., Vol. 38, No. 9, Sep. 1990, pp.1405-1412.

[27] PEIXEIRO, C., and BARBOSA, A. M.: 'Leaky and surface waves in anisotropic printed antenna structures', IEEE Trans. On Antennas Propagat., Vol. 40, No. 5, May 1992, pp.566-569.

[28] POTHARAZU, P. K., and JACKSON, D. R.: 'Analysis and design of a leaky-wave EMC dipole array', IEEE Trans. On Antennas Propagat., Vol 40, No. 8, Aug. 1992, pp.950-958.

[29] RONG, Y.: 'Propagation characteristics of circular chirowaveguides periodically loaded with metal gratings', IEE Proceedings-H, Vol. 140, No. 4, Aug. 1993, pp.254-258.

[30] YAMASHITA, E. and MA, Z.: 'Leakage characteristics of groove guide having a conductor strip', IEEE Transactions on Microwave Theory and techniques, Vol. 42, No. 10, Oct. 1994, pp.1925-1931.

# CHAPTER 2

## Analysis of a cylindrical periodic open waveguide

### *2.1 Introduction*

In this Chapter, the analysis is given for an FSG with cylindrical cross section and arbitrary element geometry. The aim is to determine the propagation characteristics of the FSG. The requirements are

1. The structure is double periodic.
2. The analysis must be flexible in that it should provide answers for any periodicity, wavelength and element geometry, including single periodic FSG.

3. The analysis must account for radiation losses due to the fact that the FSG is an open structure.

To comply with the previous requirements, the analysis uses a two dimensional Floquet modal expansion in cylindrical coordinates whereby, the currents on the elements are expanded as a set of sub-domain basis functions. Additionally, the FSG is viewed as a leaky wave structure.

It is worth mentioning at this point that, as far as the writer is concerned, an analysis as such, has not appeared in previously published work. However, there are cases found in bibliography, of circular guides with some common attributes (open, periodic), to those of FSGs. The cases include open cylinders and circular guides loaded with strip-grids [1-7]. Despite the aforementioned similarities, two arguments can be drawn:

- i. Direct comparison of results found in [1-7] and results from the analysis in this thesis, is not appropriate.
- ii. The techniques used in [1-7] can not be applied for FSGs.

The previous arguments and similarities, become more clear in the discussion which follows.

In the '60s, longitudinally slotted circular waveguides, had been modelled using an equivalent circuit representation and perturbation techniques [1-3]. However, these techniques involve approximations for the fields in the slots and break down when the openings become large, or more than one slots are considered.

The work published by Cwik [4], used Floquet modes and subdomain basis functions to analyse the scattering from a free standing cylindrical array of strips. His analysis, provided solutions only for the reflection/transmission coefficients; for a plane wave incident on the surface. This is an easier problem than that of the current study, as complex wavenumbers are not involved.

Lier [5], used modal analysis and entire domain current functions, to find the propagation inside strip-loaded waveguides. However, the array of strips, was singularly periodic and confined within a cylindrical plate.

Rong, [6], obtained the propagation and radiation of surface waves, for a cylindrical chiral core, periodically loaded with metal grids. His analysis involved Floquet expansion and mode expansion and avoided the expansion of the currents. For a more complicated geometry though, suitable expansions may not be easily found.

Kishk et. al. [7], introduced an asymptotic boundary condition to find the scattering from circular dielectric guides loaded with strip-grids. The condition by-passed the more complicated Floquet expansion, but it was accurate only when the periodicity was much smaller than the wavelength.

This Chapter, is organised as follows

In Section 2.2, infinitely long, cylindrical FSGs are introduced. The periodicity is defined in both the  $\varphi$  and  $z$  axis. Because the boundary area is not uniform, all six field components exist - hybrid modes. Since the array is periodic, the fields are assigned in the area of a unit cell only. This type of analysis is referred as modal field analysis, or Floquet modal expansion. Floquet expansion is explained in detail in Section 2.3. The tangential total electric field components are expanded in Floquet modes at each interface in Section 2.4. In the same Section, the application of the electromagnetic boundary conditions in conjunction with the orthogonality properties of the Floquet modes enable the spectral representation of the current and the formulation of an eigenvalue equation. The latter can be solved with the application of Method of Moments (MoM). A brief discussion on the MoM applications in boundary value problems is given in Section 2.5 whereby, the current is expressed as a series of sub-domain basis functions, the so called roof-top bases.

The application of the MoM yields a homogeneous system of algebraic equations. The homogeneous equations are reconstructed in a computer program, written in FORTRAN 77, so they can be solved by the computer. Section 2.6 deals with an iterative procedure which locates the solutions of the system.



In Section 2.7, a decision making for the radial propagation constant - a key factor to the analysis of open structures - is outlined. Due to the fact that the FSG is open, the propagation constant in the direction of propagation is complex [8] hence, the radial propagation constant is also complex and should belong to the appropriate Riemann sheet. Riemann sheets are extensively used in leaky wave antennas, [9-12]. Here, a discussion on Riemann sheets is provided, as additional information to the analysis of an open periodic structure.

If the propagation constant is known, then the fields and currents can be found, provided a voltage excitation is introduced [13]. This is discussed in Section 2.8. Finally, Section 2.9 deals with various numerical problems arising when using the computer model to study a representative array. Some numerical recipes are given that are useful to overcome such problems.

## 2.2 Cylindrical periodic structures (FSGs)

Fig 2.1 shows a section of an infinite periodic surface in cylindrical coordinates. Periodicity is assumed in the  $\phi$  and  $z$  directions. The surface consists of infinitely thin, perfectly conducting elements which are arranged on a cylindrical array. The array is located in free space, (free standing FSG), or on a dielectric rod.

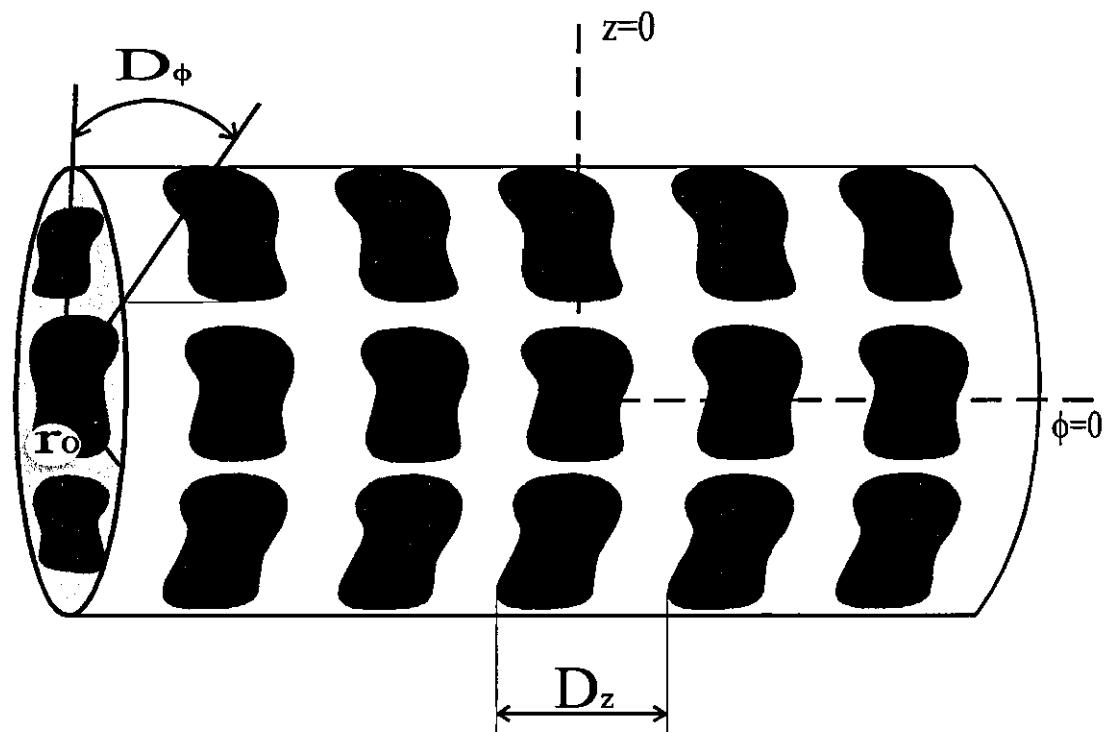


Figure 2.1: Cylindrical FSG with elements of arbitrary shape

The minimum distance of translation along each co-ordinate axis on the surface defines the period. The cylinder is also a structure with natural periodicity of  $2\pi$ . For  $N$  metallic patches around the cylinder the periodicity in  $\phi$  is equal to  $D_\phi = 2\pi / N$ .

### 2.3 Floquet modal description

Named after the nineteenth century French mathematician for his studies in periodic solutions to differential equations, the Floquet harmonics or Floquet modes are a complete orthogonal set of periodic functions. For infinite periodic arrays, each element of the array is associated with a unit cell. A boundary value problem can therefore, be defined and solved in the area of the unit cell only. In that area as well as in all space, the fields are fully described by an infinite summation of Floquet harmonics, with associated coefficients [14,15]. In the cylindrical coordinate system, each individual harmonic represents a cylindrical plane wave.

The expressions for the Floquet harmonics are found by solving the vector wave equation in cylindrical coordinates. The vector equation is solved for the electric and magnetic vector potentials so that the fields can be divided into TE and TM. By assuming the vector potential in one axis only, the vector equation is reduced to the scalar Helmholtz equation. The solutions to the scalar equation, are the wave functions. These wave functions, must also satisfy the Floquet condition which is defined in Eqn. 2.2.

It is assumed that the structure is excited by a mode with an  $e^{jn_0\varphi}$  variation (circular polarisation) and unit amplitude.  $n_0$  is an integer and it appears as an index, denoting the azimuthal variation of mode configurations (e.g. for  $n_0 = 1$ , the fields can be TE<sub>1m</sub> or, TM<sub>1m</sub>). The fields are time dependent as  $e^{j\omega t}$ , a factor which is assumed throughout this analysis. The reduced scalar wave equation in cylindrical coordinates is (Appendix A)

$$(\nabla^2 + k^2)\Xi(\rho, \varphi, z) = 0 \quad (2.1)$$

The propagation is assumed along the  $z$  axis. Since the periodicity is in both the  $\varphi$  and  $z$  axes,  $\Xi$  can be expressed as a periodic function

$$\Xi(\rho, \varphi + D_\varphi, z + D_z) = \Xi(\rho, \varphi, z)e^{jn_0D_\varphi}e^{-jk_{z0}D_z} \quad (2.2)$$

According to Eqn. (2.2), all field quantities differ between adjacent cells only by the linear phase shifts  $n_0 D_\varphi$  and  $k_{z0} D_z$ . Eqn. (2.1) can be solved by the separation of variables method. In so doing,  $\Xi$  is expressed as

$$\Xi(\rho, \varphi, z) = R(\rho)\Phi(\varphi)Z(z) \quad (2.3)$$

Assuming a periodic function  $\Phi'(\varphi) = \Phi(\varphi)e^{-jn_0\varphi}$ , then

$$\Phi'(\varphi + D_\varphi) = \Phi(\varphi + D_\varphi)e^{-jn_0(\varphi + D_\varphi)} = \Phi(\varphi)e^{-jn_0\varphi} = \Phi'(\varphi) \quad (2.4)$$

so it can be expanded as a Fourier series,

$$\Phi'(\varphi) = \sum_{p=-\infty}^{\infty} a_p e^{j\frac{2\pi}{D_\varphi} p \varphi} \quad (2.5)$$

Substituting Eqn. (2.5) into Eqn. (2.4) results

$$\Phi(\varphi) = \sum_{p=-\infty}^{\infty} a_p e^{j(\frac{2\pi}{D_\varphi} p + n_0)\varphi} \quad (2.6)$$

where each harmonic is

$$\Phi_p(\varphi) = a_p e^{jn_p \varphi} \quad (2.7)$$

and

$$n_p = \frac{2\pi}{D_\varphi} p + n_0 \quad (2.8)$$

Similarly, for the  $z$  components

$$Z(z) = \sum_{q=-\infty}^{\infty} a'_q Z_q(z) \quad (2.9)$$

where

$$Z_q(z) = e^{-jk_{zq}z} \quad (2.10)$$

and

$$k_{zq} = \frac{2\pi}{D_z}q + k_{z0} \quad (2.11)$$

$\Xi$  then, is a periodic function with each individual harmonic being a solution to Eqn. (2.1). Each harmonic is expressed as

$$\Xi_{pq}(\rho, \varphi, z) = R_p(\rho)\Psi_{pq}(\varphi, z) \quad (2.12)$$

where

$$R_p(\rho) = B_{n_p}(k_{\rho q}\rho) \quad (2.13)$$

are Bessel functions (see Appendix A) and,

$$\Psi_{pq} = e^{jn_p\varphi} e^{-jk_{zq}z} \quad (2.14)$$

For each  $p$  and  $q$  in Eqn. (2,14), the following dispersion relation holds

$$k_{\rho q}^2 = k^2 - k_{zq}^2 \quad (2.15)$$

$k$  is the free space propagation constant.

## 2.4 Field expansions

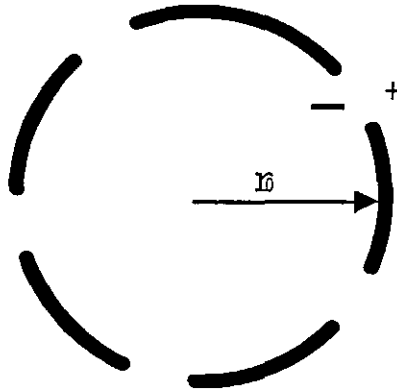


Figure 2. 2: A cylindrical cross section of the FSG, denoting the outer (+) and the inner (-) regions.

The total fields (scattered and incident), are expanded as an infinite series of periodic functions inside, as well as outside the waveguide. From this point onwards, the region inside the guide is denoted by the negative sign -, and the one outside the FSS limits by the positive sign +. In the negative region the medium has a permittivity  $\epsilon = \epsilon_0 \epsilon_r$  and a permeability  $\mu_0$ . The characteristic impedance of free space is denoted as

$$\eta_0 = \sqrt{\mu_0 / \epsilon_0}$$

**Total fields in the negative region ( $r < r_0$ )**

$$\underline{E}^- = \sum_{pq=-\infty}^{\infty} \underline{E}_{pq}^- , \quad \underline{H}^- = \sum_{pq=-\infty}^{\infty} \underline{H}_{pq}^- \quad (2.16)$$

There are three field components - one in each axis- for every field harmonic

$$\underline{E}_{pq} = E_{\rho pq} \hat{u}_\rho + E_{\phi pq} \hat{u}_\phi + E_{z pq} \hat{u}_z \quad (2.17)$$

$\hat{u}$  is a unit vector. The dispersion relation for the medium inside the guide is given by the equation

$$k_{\rho q}^2 = \epsilon_r k^2 - k_{zq}^2 \quad (2.18)$$

The  $z$ -directed  $E$ -field component, is found according to Eqn. (A.5) in Appendix A

$$E_{zpq}^- = -j \frac{(\omega^2 \epsilon \mu - k_{zq}^2)}{\omega \epsilon} A_{pq}^- J_{n_p}(k_{\rho q}^- \rho) \Psi_{pq} \quad (2.19)$$

In the latter equation,  $A_{pq}^\pm$  are amplitude coefficients for the TM wave potential.

To simplify the field expressions, the following are substituted in Eqn. (2.19)

$$A_{pq}^- = a_{pq}^- \frac{j\omega\epsilon}{k_{\rho q}^-} \quad (2.20)$$

Then Eqn. (2.19) becomes

$$E_{zpq}^- = a_{pq}^- J_{n_p}(k_{\rho q}^- \rho) \Psi_{pq} \quad (2.21)$$

The  $z$ -directed  $H$ -field component is found following Eqn. (A.9) (assuming  $B_{pq}^\pm$  are amplitude coefficients for the TE wave potential)

$$F_z^\pm = B_{pq}^\pm \Xi_{pq}$$

$$H_{zpq}^- = -\frac{j}{\eta_0} b_{pq}^- J_{n_p}(k_{\rho q}^- \rho) \Psi_{pq} \quad (2.22)$$

where

$$B_{pq}^- = \frac{k}{k_{\rho q}^-} b_{pq}^- \quad (2.23)$$

The  $\varphi$  components of the electric and magnetic fields are (referred Eqns. (A.6)-(A.10))

$$E_{\varphi pq}^- = \left[ A_{pq}^- \frac{-j(-jk_{zq})(jn_p)}{\omega \varepsilon \rho} J_{n_p}(k_{\rho q}^- \rho) + B_{pq}^- k_{\rho q}^- J'_{n_p}(k_{\rho q}^- \rho) \right] \Psi_{pq}$$

or

$$E_{\varphi pq}^- = \left[ a_{pq}^- \frac{k_{zq} n_p}{k_{\rho q}^- \rho} J_{n_p}(k_{\rho q}^- \rho) + b_{pq}^- \frac{k}{k_{\rho q}^-} J'_{n_p}(k_{\rho q}^- \rho) \right] \Psi_{pq} \quad (2.24)$$

and

$$H_{\varphi pq}^- = \left[ -A_{pq}^- \varepsilon_r k_{\rho q} J'_{n_p}(k_{\rho q}^- \rho) + B_{pq}^- \frac{-j(-jk_{zq})(jn_p)}{\omega \mu_0 \rho} J_{n_p}(k_{\rho q}^- \rho) \right] \Psi_{pq}$$

or

$$H_{\varphi pq}^- = -\frac{j}{\eta_0} \left[ a_{pq}^- \frac{k \varepsilon_r}{k_{\rho q}^-} J'_{n_p}(k_{\rho q}^- \rho) + b_{pq}^- \frac{k_{zq} n_p}{k_{\rho q}^- \rho} J_{n_p}(k_{\rho q}^- \rho) \right] \Psi_{pq} \quad (2.25)$$

$J$  is the Bessel function of first kind, of order  $n_p$  and of complex argument.  $J'$  is the derivative of the Bessel function with respect to the whole argument. Bessel functions of complex arguments, represent localised standing waves [16]. In the region ( $\rho > r_0$ ) similar expressions are used except that the Bessel functions are replaced by Hankel functions of the second kind ( $H^{(2)}$ ). The latter represent outward travelling waves only.  $a_{pq}^+$  and  $b_{pq}^+$  are the unknown coefficients of the TM and TE components respectively.

### Total fields in the positive region ( $r > r_0$ )

The total tangential field components are expressed as an infinite series of modal harmonics. The harmonics are



$$E_{zpq}^+ = a_{pq}^+ H_{n_p}^{(2)}(k_{\rho q}^+ \rho) \Psi_{pq} \quad (2.26)$$

$$H_{zpq}^+ = -\frac{j}{\eta_0} b_{pq}^+ H_{n_p}^{(2)}(k_{\rho q}^+ \rho) \Psi_{pq} \quad (2.27)$$

$$E_{\phi pq}^+ = \left[ a_{pq}^+ \frac{k_{zq} n_p}{(k_{\rho q}^+)^2 \rho} H_{n_p}^{(2)}(k_{\rho q}^+ \rho) + b_{pq}^+ \frac{k}{k_{\rho q}^+} H_{n_p}'^{(2)}(k_{\rho q}^+ \rho) \right] \Psi_{pq} \quad (2.28)$$

$$H_{\phi pq}^+ = -\frac{j}{\eta_0} \left[ b_{pq}^+ \frac{k_{zq} n_p}{(k_{\rho q}^+)^2 \rho} H_{n_p}^{(2)}(k_{\rho q}^+ \rho) + a_{pq}^+ \frac{k}{k_{\rho q}^+} H_{n_p}'^{(2)}(k_{\rho q}^+ \rho) \right] \Psi_{pq} \quad (2.29)$$

The total fields can be found by summing all the field harmonics over  $p$  and  $q$  from  $-\infty$  to  $+\infty$ . Next, the expressions can be obtained for the unknown amplitude coefficients. In doing so, the first step is to apply the continuity condition for the tangential electric field components across the waveguide boundary, at  $\rho = r_0$ . The boundary condition is expressed as

$$E_z^-(r_0) = E_z^+(r_0) \quad (2.30)$$

$$E_\phi^-(r_0) = E_\phi^+(r_0) \quad (2.31)$$

It should be noted that Eqns (2.30) and (2.31) refer to the air boundary; the metallic interface boundary conditions are covered by Eqn. (2.56) in Section 2.5.1.

Using the boundary condition, Eqn. (2.30), in conjunction with Eqn. (2.26) and Eqn. (2.21) yields

$$a_{pq}^- = a_{pq}^+ \frac{H_{n_p}^{(2)}(k_{\rho q}^+ r_0)}{J_{n_p}(k_{\rho q}^- r_0)} \quad (2.32)$$

For brevity, the following substitution is used in place of the argument in the Bessel functions:  $z_q^\pm = k_{\rho q}^\pm r_0$ . Eqn (2.31) in conjunction with Eqns. (2.24) and (2.28) yields

$$b_{pq}^+ = a_{pq}^- \frac{z_q^+}{k} \frac{J_{n_p}(z_q^-)}{H_{n_p}^{(2)}(z_q^+)} \left[ \frac{1}{z_q^{-2}} - \frac{1}{z_q^{+2}} \right] + b_{pq}^- \frac{J'_{n_p}(z_q^-)}{H_{n_p}^{(2)}(z_q^+)} \frac{z_q^+}{z_q^-} \quad (2.33)$$

The next step, is to apply the boundary condition which relates the tangential magnetic field components to the conductor's induced surface current. This is expressed as

$$\hat{\rho} \times (\underline{H}^- - \underline{H}^+) = \underline{I} \quad (2.34)$$

Braking the last equation to its component parts results

$$H_z^-(r_0) - H_z^+(r_0) = I_\varphi(\varphi, z) \quad \rho=r_0 \quad (2.35)$$

$$H_\varphi^-(r_0) - H_\varphi^+(r_0) = I_z(\varphi, z) \quad \rho=r_0 \quad (2.36)$$

The following simplifications of the magnetic field expressions at  $\rho=r_0$  will now be introduced

$$H_{zpq}^- - H_{zpq}^+ \Big|_{\rho=r_0} = \left( b_{pq}^- \mathcal{B}_{zpq} + a_{pq}^- \mathcal{A}_{zpq} \right) e^{jn_p \varphi} e^{-jk_{zq} z} \quad (2.37)$$

$$H_{\varphi pq}^- - H_{\varphi pq}^+ \Big|_{\rho=r_0} = \left( b_{pq}^- \mathcal{B}_{\varphi pq} + a_{pq}^- \mathcal{A}_{\varphi pq} \right) e^{jn_p \varphi} e^{-jk_{zq} z} \quad (2.38)$$

where

$$\mathcal{B}_{zpq} = -\frac{j}{\eta_0} \left[ J_{n_p}(z_q^-) - J'_{n_p}(z_q^-) \frac{H_{n_p}^{(2)}(z_q^+) z_q^+}{H_{n_p}^{(2)}(z_q^+) z_q^-} \right] \quad (2.39)$$

$$\mathcal{A}_{\varphi pq} = -\frac{j}{\eta_0} \left\{ \frac{k\epsilon_r}{k_{\rho q}} J'_{n_p}(z_q^-) - \right.$$

$$J_{n_p}(z_q^-) \left\{ \frac{kr_0}{z_q^+} \frac{H_{n_p}^{(2)}(z_q^+)}{H_{n_p}^{(2)}(z_q^+)} + \frac{(kz_q r_0)^2}{kr_0 z_q^+} \frac{H_{n_p}^{(2)}(z_q^+)}{H_{n_p}^{(2)}(z_q^+)} \left[ \frac{1}{z_q^{-2}} - \frac{1}{z_q^{+2}} \right] \right\} \quad (2.40)$$

$$\mathcal{B}_{\phi pq} = -\frac{j}{\eta_0} \frac{kz_q n_p r_0}{z_q^-} \left[ \frac{1}{z_q^-} J_{n_p}(z_q^-) - \frac{1}{z_q^+} J'_{n_p}(z_q^-) \frac{H_{n_p}^{(2)}(z_q^+)}{H_{n_p}^{(2)}(z_q^+)} \right] \quad (2.41)$$

$$\mathcal{A}_{zpq} = -\frac{j}{\eta_0} \frac{kz_q z_q^+}{k} J_{n_p}(z_q^-) \frac{H_{n_p}^{(2)}(z_q^+)}{H_{n_p}^{(2)}(z_q^+)} \left( \frac{1}{z_q^{-2}} - \frac{1}{z_q^{+2}} \right) \quad (2.42)$$

If the medium inside and outside the guide, is the same, then  $z_q^- = z_q^+$ , and

$$\mathcal{A}_{zpq} = 0.$$

The tangential components,  $\Psi_{pq}$ , of the harmonics are orthogonal over the area of the periodic cell due to

$$\frac{1}{r_0 D_\phi D_z} \int_{\partial s} \Psi_{pq} \Psi_{p'q'}^* ds = \delta_{pp'} \delta_{qq'}$$

where the delta function is 1 for  $p = p'$  only; 0 otherwise.  $\Psi_{p'q'}^*$  is the complex conjugate of the tangential field  $\Psi_{pq}$ , of harmonic number  $p', q'$ . The integration is over the area of the periodic cell.

The field coefficients  $a_{pq}^\pm$  and  $b_{pq}^\pm$  can be expressed in terms of the unknown surface current by combining Eqns (2.35)-(2.38). Moreover, due to the orthogonality, each side of the Eqns. (2.37), (2.38), is multiplied by the complex conjugate of  $\Psi$ ,  $(e^{-jn_p \phi} e^{jkz_q z})$  and integrated over the area of the periodic cell  $r_0 D_\phi D_z$  with respect to  $\phi$  and  $z$ . This procedure yields the spectral coefficients of the current

$$a_{pq}^- \mathcal{A}_{\varphi pq} + b_{pq}^- \mathcal{B}_{\varphi pq} = \tilde{I}_{zpq} \quad (2.43)$$

where

$$\tilde{I}_{zpq} = \int_{\text{unit cell}} I_z r_0 d\phi dz \quad (2.43a)$$

$\tilde{I}_{zpq}$ , is the spectral coefficient of the  $z$  directed current, and

$$b_{pq}^- \mathcal{B}_{zpq} - a_{pq}^- \mathcal{A}_{zpq} = \tilde{I}_{\varphi pq} \quad (2.44)$$

where

$$\tilde{I}_{\varphi pq} = \int_{\text{unit cell}} I_\varphi r_0 d\phi dz \quad (2.44a)$$

$\tilde{I}_{\varphi pq}$ , is the spectral coefficient of the  $\varphi$  directed current. The tilde denotes the Fourier transformation of the expanded current over the periodic cell. Eqns. (2.43) and Eqn. (2.44), are written as a linear system of equations, in matrix form, which can be solved for the unknown field amplitude coefficients

$$\begin{bmatrix} \mathcal{A}_{\varphi pq} & \mathcal{B}_{\varphi pq} \\ -\mathcal{A}_{zpq} & \mathcal{B}_{zpq} \end{bmatrix} \begin{bmatrix} a_{pq}^- \\ b_{pq}^- \end{bmatrix} = \begin{bmatrix} \tilde{I}_{zpq} \\ \tilde{I}_{\varphi pq} \end{bmatrix} \quad (2.45)$$

$$a_{pq}^- = \frac{\begin{vmatrix} \tilde{I}_{zpq} & \mathcal{B}_{\varphi pq} \\ \tilde{I}_{\varphi pq} & \mathcal{B}_{zpq} \end{vmatrix}}{\begin{vmatrix} \mathcal{A}_{\varphi pq} & \mathcal{B}_{\varphi pq} \\ -\mathcal{A}_{zpq} & \mathcal{B}_{zpq} \end{vmatrix}} \quad (2.46)$$

$$b_{pq}^- = \frac{\begin{vmatrix} \mathcal{A}_{\varphi pq} & \tilde{I}_{zpq} \\ -\mathcal{A}_{zpq} & \tilde{I}_{\varphi pq} \end{vmatrix}}{\begin{vmatrix} \mathcal{A}_{\varphi pq} & \mathcal{B}_{\varphi pq} \\ -\mathcal{A}_{zpq} & \mathcal{B}_{zpq} \end{vmatrix}} \quad (2.47)$$

From the two last equations the coefficients  $a_{pq}^-$  and  $b_{pq}^-$  can also be expressed as

$$a_{pq}^- = \mathcal{B}'_{zpq} \tilde{I}_{zpq} + \mathcal{B}'_{\varphi pq} \tilde{I}_{\varphi pq} \quad (2.48)$$

$$b_{pq}^- = \mathcal{A}'_{zpq} \tilde{I}_{zpq} + \mathcal{A}'_{\varphi pq} \tilde{I}_{\varphi pq} \quad (2.49)$$

where

$$\mathcal{B}'_{zpq} = \mathcal{B}_{zpq} / U \quad (2.50)$$

$$\mathcal{A}'_{zpq} = \mathcal{A}_{zpq} / U \quad (2.51)$$

$$\mathcal{A}'_{\varphi pq} = \mathcal{A}_{\varphi pq} / U \quad (2.52)$$

$$\mathcal{B}'_{\varphi pq} = -\mathcal{B}_{\varphi pq} / U \quad (2.53)$$

and

$$U = \mathcal{B}_{\varphi pq} \mathcal{A}_{zpq} + \mathcal{B}_{zpq} \mathcal{A}_{\varphi pq} \quad (2.54)$$

## 2.5 The Method of Moments

Since it is not possible to know the actual current distribution on the unit cell *a-priori*, a set of suitable current expansions is employed, to approximate the total current. These current expansions, are given as a set of weighted functions, say  $\{h_n\}$ , which also form a complete set. The current may therefore, be expanded as

$$\underline{I} = \underline{I}_z + \underline{I}_\varphi = \sum_{n=-\infty}^{\infty} c_{zn} \underline{h}_{zn} + \sum_{n=-\infty}^{\infty} c_{\varphi n} \underline{h}_{\varphi n} \quad (2.55)$$

The condition for completion is met when  $\{h_n\}$  converges for  $|n| \rightarrow \infty$ , and there is always a finite limit in the domain in which they are defined. The domain is the same as that for the current, and is important that the functions are linearly independent. If the functions are linearly independent, then the Method of Moments generates a system of linearly independent equations. The Moments Method analysis has been dealt extensively elsewhere, for example [17,18]. In the following Section, a set of sub-domain basis functions is employed to analyse the currents on the elements of the FSG.

### 2.5.1 Sub-domain basis functions

The remaining boundary condition on the waveguide surface is that the total, tangential electric field components, vanish on the conductor

$$E_z^- = 0 \quad (2.56)$$

$$E_\varphi^- = 0 \quad (2.57)$$

$E_z^-$  and  $E_\varphi^-$ , are found by summing an infinite number of the field harmonics given in Eqn. (2.21) and Eqn. (2.24) respectively. Since it is not possible to perform an

infinite summation by means of a digital machine, the summations are truncated. The truncated limits are  $P$  and  $Q$  and Eqns. (2.56), (2.57) become

( $z$ - component)

$$\sum_{p=-P/2}^{P/2} \sum_{q=-Q/2}^{Q/2} a_{pq}^- J_{n_p}(z_q^-) \Psi_{pq} = 0 \quad (2.58)$$

( $\varphi$ - component)

$$\sum_{p=-P/2}^{P/2} \sum_{q=-Q/2}^{Q/2} \left[ \left( a_{pq}^- \frac{k_{zq} n_p r_0}{z_q^-} J_{n_p}(z_q^-) + b_{pq}^- \frac{k}{k_{\rho q}^-} J'_{n_p}(z_q^-) \right) \right] \Psi_{pq} = 0 \quad (2.59)$$

or with Eqn. (2.48) and Eqn. (2.49)

$$\sum_{pq} \left( \mathcal{B}'_{zpq} \tilde{I}_{zpq} + \mathcal{B}'_{\varphi pq} \tilde{I}_{\varphi pq} \right) J_{n_p}(z_q^-) \Psi_{pq}(z, \varphi) = 0 \quad (2.60)$$

$$j\eta \sum_{p=-P/2}^{P/2} \sum_{q=-Q/2}^{Q/2} \left[ \left( \mathcal{B}'_{zpq} \frac{k_{zq} n_p r_0}{z_q^-} J_{n_p}(z_q^-) + \mathcal{A}'_{zpq} \frac{k}{k_{\rho q}^-} J'_{n_p}(z_q^-) \right) \tilde{I}_{zpq} + \right. \\ \left. \left( \mathcal{B}'_{\varphi pq} \frac{k_{zq} n_p r_0}{z_q^-} J_{n_p}(z_q^-) + \mathcal{A}'_{\varphi pq} \frac{k}{k_{\rho q}^-} J'_{n_p}(z_q^-) \right) \tilde{I}_{\varphi pq} \right] \Psi_{pq}(\varphi, z) = 0 \quad (2.61)$$

The last two homogeneous equations, are weighted (or *tested*), by the same current basis function, (*Ritz-Galerkin* case) and in an average sense, by taking the inner product. Eqns. (2.60) and (2.61) become

$$\sum_{pq} \left( \mathcal{B}'_{zpq} \tilde{I}_{zpq} + \mathcal{B}'_{\phi pq} \tilde{I}_{\phi pq} \right) J_{n_p} \left( z_q^- \right) \tilde{h}_{nzpq}^* = 0 \quad (2.62)$$

$$j\eta \sum_{p=-P/2}^{P/2} \sum_{q=-Q/2}^{Q/2} \left[ \left( \mathcal{B}'_{zpq} \frac{k_{zq} n_p r_0}{z_q^-} J_{n_p} \left( z_q^- \right) + \mathcal{A}'_{zpq} \frac{k}{k_{\rho q}^-} J'_{n_p} \left( z_q^- \right) \right) \tilde{I}_{zpq} + \left( \mathcal{B}'_{\phi pq} \frac{k_{zq} n_p r_0}{z_q^-} J_{n_p} \left( z_q^- \right) + \mathcal{A}'_{\phi pq} \frac{k}{k_{\rho q}^-} J'_{n_p} \left( z_q^- \right) \right) \tilde{I}_{\phi pq} \right] \tilde{h}_{nzpq}^* = 0 \quad (2.63)$$

where,  $h_{nzpq}$  is the testing function.

The last two equations form a homogeneous system where, the unknowns are the currents in both directions. The analysis presented in this thesis, uses the so called 'roof-top' basis functions to expand the currents (see Section 2.5.2). In theory, an infinite number of bases must be used to equal the actual current distribution. Since, it is not possible to represent an infinite series by means of a computer, a truncated number of roof-top functions is used. The Method of Moments will then produce a number of linearly independent equations as the number of the truncated bases.

### 2.5.2 Roof-top functions in the Method of Moments

Roof-top bases have been used extensively in the past to analyse the current on the elements in periodic screens. A plethora of communications have dealt with roof-top functions analysis, of which only a representative part is cited in this thesis [19-22]. The roof-top functions, are defined as a product of triangular (piecewise linear) functions along the direction of current flow and of step (piecewise constant) functions in the orthogonal direction. As shown in Fig. 2.3, in the direction of current flow, the triangular function goes to zero smoothly at the edges of the



conductor whereas, the current flowing parallel with the edges is not zero. Therefore, the singularity at the edges is preserved [19].

The linear element in Fig. 2.3, centred at the origin with dimensions  $L_\varphi$  and  $L_z$ , is discretised in the  $z$  and  $\varphi$  directions as

$$\begin{aligned} L_\varphi &= S\Delta\varphi \\ L_z &= K\Delta z \end{aligned} \quad (2.64)$$

then, the representations for the  $\varphi$  current take the form

$$I_\varphi(\varphi, z) = \sum_{-(S-1)/2}^{(S-1)/2-1} \sum_{-(K-1)/2}^{(K-1)/2} c_{sk\varphi} \Lambda_{s+0.5}(\varphi) \Pi_k(z), \quad (2.65)$$

There are  $K(S-1)$  unknown current functions for the  $\varphi$ -directed current. Each roof-top occupies an area  $2\Delta z\Delta\varphi$ , in a manner so that adjacent roof-tops overlap to allow the continuation of the current. Moreover, each of the roof-top functions is weighted by unknown current coefficients  $\{c_{sk\varphi}\}$ . Note that, in order to signify the two dimensions involved, the subscript  $n$  in Eqn. (2.55) has been substituted by the subscripts  $k$  and  $s$ ; both  $k$  and  $s$  are used to index the roof-top basis. The  $z$  directed roof-top functions are defined over rectangles of area equal to those of the  $\varphi$  directed roof-tops, but having  $z$ -orientation. For the  $z$ -directed current the representation is as follows

$$I_z(\varphi, z) = \sum_{-(K-1)/2}^{(K-1)/2-1} \sum_{-(S-1)/2}^{(S-1)/2} c_{ksz} \Lambda_{k+0.5}(z) \Pi_s(\varphi), \quad (2.66)$$

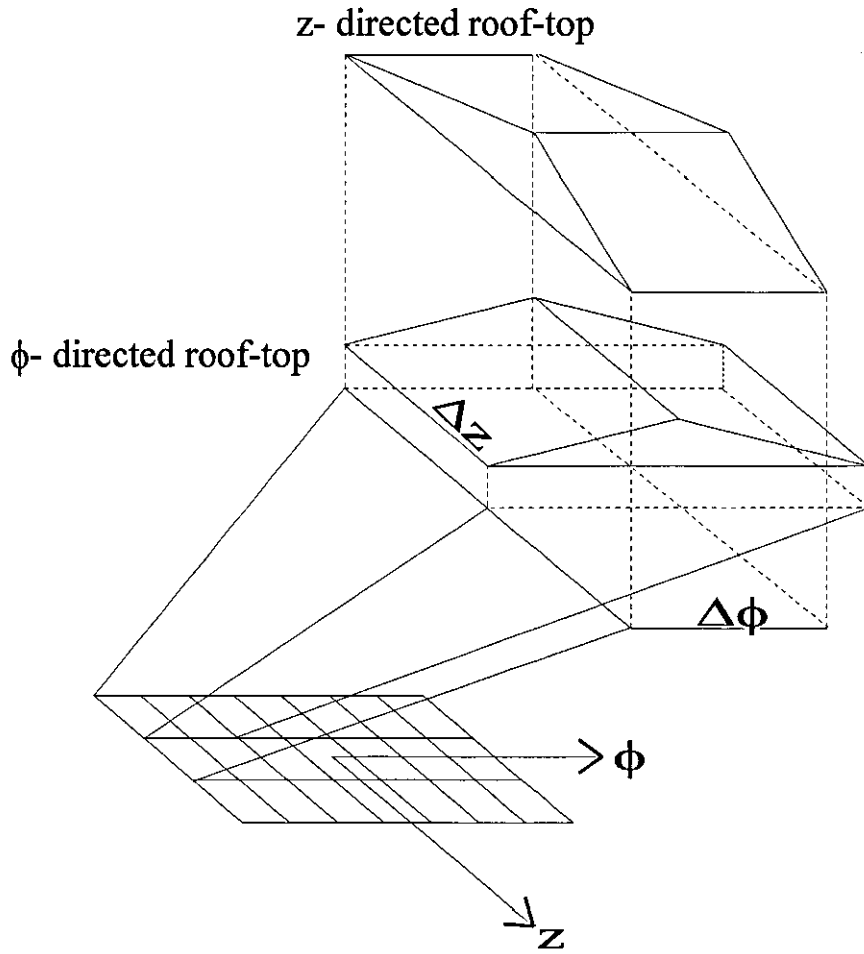


Figure 2.3: Roof-tops for the current expansion on a linear element  $K=3$ ,  $S=7$

$\Lambda$ , is the triangular function which is defined as

$$\Lambda_I(x) = \begin{cases} 1 - \frac{|x-IDx|}{Dx}, & |x-IDx| < Dx \\ 0, & \text{elsewhere,} \end{cases} \quad (2.67)$$

and  $\Pi$  is the step function defined as

$$\Pi_I(x) = \begin{cases} 1, & |x-IDx| < \frac{Dx}{2} \\ 0, & \text{elsewhere,} \end{cases} \quad (2.68)$$

The transforms of the roof-top functions required in Eqns. (2.48) and (2.49), are

$$\begin{aligned}\tilde{I}_{skpq\varphi} &= \frac{1}{r_0 D_z D_\varphi} \int_{(-s+0.5)\Delta\varphi}^{(s+0.5)\Delta\varphi} \Lambda_{s\varphi}(\varphi) e^{-jn_p\varphi} d\varphi \int_{-k\Delta z/2}^{k\Delta z/2} c_{sk\varphi} \Pi_{kz}(z) e^{jk_{zq}z} dz \\ &= \frac{\Delta\varphi}{r_0 D_\varphi} \text{sinc}^2\left(\frac{n_p\Delta\varphi}{2}\right) e^{j(s+0.5)n_p\Delta\varphi} \frac{1}{D_z} \text{sinc}\left(\frac{k_{zq}\Delta z}{2}\right) c_{sk\varphi} e^{-jk_{zq}\Delta z}\end{aligned}\quad (2.69)$$

$$\begin{aligned}\tilde{I}_{kspqz} &= \frac{1}{r_0 D_z D_\varphi} \int_{-s\Delta\varphi/2}^{s\Delta\varphi/2} \Pi_{s\varphi}(\varphi) e^{-jn_p\varphi} d\varphi \int_{(-k+0.5)\Delta z}^{(k+0.5)\Delta z} c_{ksz} \Lambda_{kz}(z) e^{jk_{zq}z} dz \\ &= \frac{\Delta\varphi}{r_0 D_\varphi} \text{sinc}\left(\frac{n_p\Delta\varphi}{2}\right) e^{jsn_p\Delta\varphi} \frac{1}{D_z} \text{sinc}^2\left(\frac{k_{zq}\Delta z}{2}\right) c_{ksz} e^{-jk_{zq}\Delta z}\end{aligned}\quad (2.70)$$

Following Eqns. (2.69) and (2.70), the transformation of the current in each direction, when using roof-top functions expansion, is

$$\sum_{-(S-1)/2}^{(S-1)/2-1} \sum_{-(K-1)/2}^{(K-1)/2} \tilde{I}_{skpq\varphi} = \tilde{I}_{\varphi pq} \quad (2.71)$$

$$\sum_{-(K-1)/2}^{(K-1)/2-1} \sum_{-(S-1)/2}^{(S-1)/2} \tilde{I}_{kspqz} = \tilde{I}_{z pq} \quad (2.72)$$

By substituting Eqns. (2.71), (2.72) back in Eqns. (2.60) and (2.61) and using roof-top bases as the testing functions,  $2SK-(S+K)$  equations are obtained. These equations can be written in a matrix form as

$$[Z][C] = [0] \quad (2.73)$$

where

$$[C] = \begin{bmatrix} c_{ksz} \\ c_{sk\varphi} \end{bmatrix} \quad (2.74)$$

Is the unknown column matrix of the current coefficients and  $[Z]$  is the  $2SK - (S+K) \times 2SK - (S+K)$  impedance matrix with submatrices

$$[Z] = \begin{bmatrix} [Z_{1k's'ksz}] & [Z_{1k's'sk\varphi}] \\ [Z_{2s'k'ksz}] & [Z_{2s'k'sk\varphi}] \end{bmatrix} \quad (2.75)$$

where

$$Z_{1k's'ksz} = \sum_{-\frac{Q}{2}}^{\frac{Q}{2}} \sum_{-\frac{P}{2}}^{\frac{P}{2}} \mathcal{B}'_{zpq} J_{n_p}(z_q) \tilde{I}_{kspqz} \tilde{I}_{k's'pqz}^* \quad (2.76)$$

$$Z_{1k's'sk\varphi} = \sum_{-\frac{Q}{2}}^{\frac{Q}{2}} \sum_{-\frac{P}{2}}^{\frac{P}{2}} \mathcal{B}'_{\varphi pq} J_{n_p}(z_q) \tilde{I}_{skpq\varphi} \tilde{I}_{k's'pqz}^* \quad (2.77)$$

$$Z_{2s'k'ksz} = \sum_{-\frac{Q}{2}}^{\frac{Q}{2}} \sum_{-\frac{P}{2}}^{\frac{P}{2}} \left( \mathcal{B}'_{zpq} \frac{k_{zq} n_p r_0}{z_q} J'_{n_p}(z_q^-) + \mathcal{A}'_{zpq} \frac{k}{k_{\rho q}^-} J'_{n_p}(z_q^-) \right) \tilde{I}_{kspqz} \tilde{I}_{s'k'pq\varphi}^* \quad (2.78)$$

$$Z_{2s'k'sk\varphi} = \sum_{-\frac{Q}{2}}^{\frac{Q}{2}} \sum_{-\frac{P}{2}}^{\frac{P}{2}} \left( \mathcal{B}'_{\varphi pq} \frac{k_{zq} n_p r_0}{z_q} J'_{n_p}(z_q^-) + \mathcal{A}'_{\varphi pq} \frac{k}{k_{\rho q}^-} J'_{n_p}(z_q^-) \right) \tilde{I}_{skpq\varphi} \tilde{I}_{s'k'pq\varphi}^* \quad (2.79)$$

In order to ensure reliability of the results when MoM is applied, the relative convergence phenomenon should be studied. The phenomenon stems from the double truncation; the first truncation is on the number of bases and the second on the number of Floquet harmonics. Depending on the choice of these numbers, the results may not converge. The issue of relative convergence phenomenon has been dealt extensively elsewhere, e.g. when solving a boundary value problem for a rectangular waveguide [23] or, when calculating the reflection from microstrip-patch arrays [24] and planar FSS [20]. The transform of the bases is important as it enters the calculations for the matrix elements in Eqn. (2.76) to Eqn. (2.79). To guarantee stable results, one should include in the summations, the spectral components of each basis that contribute the most to the series. If the transform of the bases exhibits tendency to converge after a few terms, then higher spectral components will decay rapidly. Therefore, if these terms are left out from the summations, there will be no significant effect and convergence of the result is easily assured with only a few terms. However, it is known, that roof-top functions are smooth enough to produce convergent series [19,20].

In order to ensure convergence, the practice is, to start with a given number of bases and increase the number of Floquet harmonics until there is no change in the results. Then, try with a different number of bases and increase the Floquet harmonics until there is no change in the obtained results. Also, one can find a criterion for convergence, this ratio:  $2SK-(S + K)/PQ$  (number of bases/number of Floquet modes), [15]. This ratio will be defined in later Sections, for particular FSGs. It should be noted though, that convergence tests add to the expense of computational time. In this thesis, such tests constitute an important part in the presentation of the results.

## ***2.6 Deriving a solution***

When the determinant of  $[Z]$  in Eqn. (2.73) is zero, the homogenous system has non-zero solutions. The mode content is then found using an iterative procedure in which the determinant is computed with the help of an appropriate numerical routine. Here, the F04ADF Numerical Algorithm Group routine, is employed. The determinant is calculated as a function of both the real propagation constant  $\beta$  and the attenuation constant  $\alpha$ . The numerical procedure, uses different values of  $\beta$  and  $\alpha$  as inputs until it finds a zero for the determinant.  $\beta$  and  $\alpha$  are usually normalised with respect to the free space propagation constant  $k$  or, the periodicity in  $z$ . In order to reduce computational time each mode can be derived individually. In doing so, it is sufficient to find an initial point on a dispersion curve and then follow that point closely. Naturally, other parameters such as the number of Floquet harmonics and the number of total roof-top bases add to the computational time. These parameters are quantified in the numerical results in the following Chapters.

## ***2.7 Complex roots introduced in open periodic structures***

In open structures, the electromagnetic energy is carried along the direction of propagation by waves, which are not only confined inside the guiding structure. These waves can also radiate energy outside at a particular angle (see Appendix B). Mathematically this radiation leakage is expressed in terms of complex waves or, waves with complex wavenumbers.

In the case of periodic arrays, the Floquet modal analysis introduces an infinite spectrum of wave harmonics. These harmonics may possess different propagation characteristics or the same, i.e. mode coupling effect (see Appendix B). Electromagnetic energy propagating inside the periodic structure, is associated with all of these harmonics, resulting in a complex wave or Bloch wave [9]. Individual harmonics may represent fast waves or slow waves, which depending on the

operating frequency may become significant. Slow waves, are usually referred to as surface waves. These are waves which propagate longitudinally to a surface whilst, transversely to this surface, they decay as they travel towards infinity. Since they satisfy the radiation condition (radiated field is zero at infinity), slow waves represent the proper discrete spectrum of the radiated field. Pure radiation though, is associated with fast waves. Fast waves travel inside the guide with speeds greater than the speed of light and since the structure is unbounded, they loose energy in the direction of propagation. This energy loss should be compensated as energy gain in the transverse (radial) direction where, the wave is increased in amplitude as it travels towards infinity. This mathematical representation describes leaky waves which are known to characterise the improper, or non-spectral radiated field [10].

According to the dispersion relation, Eqn. (2.15), the radial wavenumber  $k_{\rho q}$  is a doubled-value function of  $k_{zq}$ . For each value of  $k_{zq}$  on the complex plane,  $k_{\rho q}$  can be uniquely specified if two Reimann sheets can be visualised. Together, they define an unusual surface, the Reimann surface. The top Reimann sheet corresponds to proper or surface waves with  $\text{Im}\{k_{\rho q}\} \leq 0$ . The bottom, corresponds to non-spectral or leaky wave solutions with  $\text{Im}\{k_{\rho q}\} > 0$ . In the following Section, the decision making for the choice of the complex radial wavenumbers is presented.

### 2.7.1 *On the choice of the transverse wavenumber $k_{\rho q}$*

The procedure for choosing the correct square root value for the radial wavenumber, is closely related to the iterative procedure which finds the zero of the determinant. For every value of  $\beta$ , the choice of  $k_{\rho q}$  must provide a better physical interpretation of the waves travelling outside the guide. The other solution is on a different Reimann sheet. If chosen, it yields another set of wavenumbers that also stands as a mathematical solution to the formulated characteristic equation.

Consider the complex propagation constant  $\beta - ja$ , of the fundamental harmonic.

If  $\frac{\beta}{k} < 1$ , then the harmonic is a fast wave. Assuming  $\epsilon_r = 1$ , Eqn. (2.15) results

$$k_{\rho 0}^2 = k^2 - \beta^2 + \alpha^2 + j2\alpha\beta \quad (2.80)$$

$\alpha$  is positive to denote attenuation in  $z$ . Also

$$k_{\rho 0}^2 = \text{Re}\{k_{\rho 0}\}^2 - \text{Im}\{k_{\rho 0}\}^2 + j2\text{Re}\{k_{\rho 0}\}\text{Im}\{k_{\rho 0}\} \quad (2.81)$$

This means that  $\text{Im}(k_{\rho 0}^2) > 0$  so the real and imaginary parts of  $k_{\rho}$  must be of the same sign. The two possible solutions are in the first and the third quadrant of the complex plane respectively. The first represents a leaky outward travelling wave that increases in amplitude as it travels away from the guide. The other solution represents an inward travelling wave. Since, second kind Hankel functions of complex argument represent the fields outside the FSG region, the first solution is suitable. The full decision making when all harmonics are considered in [25]

$$\text{a. } \text{Im}(k_{\rho q}) > 0 \text{ and } \text{Re}(k_{\rho q}) > 0 \text{ if } q = 0 \quad \beta/k < 1 \quad (2.82)$$

It represents a wave that is gaining power as it travels to infinity. Otherwise called an improper wave.

$$\text{b. } \text{Im}(k_{\rho q}) < 0 \text{ and } \text{Re}(k_{\rho q}) < 0 \text{ if } q = 0 \quad \beta/k > 1 \quad (2.83)$$

Represents a proper surface wave travelling in the forward direction with speed less than the speed of light (slow wave). It decays away from the structure.

$$\text{c. } \text{Im}(k_{\rho q}) < 0 \text{ and } \text{Re}(k_{\rho q}) < 0 \text{ if } q > 0 \quad (2.84)$$

Usually, for a representative design, there are several periodicities considered per wavelength. This means that the real part of the wavenumber for a higher harmonic, as calculated in Eqn. 2.11, is greater than  $k$ . For  $q > 0$ ,  $k_{\rho q}$  is located in the third



quadrant of the complex plane and on the top Reimann sheet. It represents a surface wave that decays away from the structure. The radiation is end-fire.

$$d. \quad \left. \begin{array}{l} \text{Im}(k_{\rho q}) < 0 \text{ and } \text{Re}(k_{\rho q}) > 0 \text{ if } \text{Re}\{k_{zq}\} \leq 0 \\ \text{Im}(k_{\rho q}) > 0 \text{ and } \text{Re}(k_{\rho q}) > 0 \text{ if } k > \text{Re}\{k_{zq}\} > 0 \end{array} \right\} \text{if } q < 0 \quad (2.85)$$

Consider first in Eqn (2.85), the case  $\text{Re}\{k_{zq}\} < -k < 0$ . In this case, the choice of  $k_{\rho q}$  represents a proper surface wave travelling in the backward direction (radiation angle  $-90^\circ$ ). As frequency increases,  $\text{Re}\{k_{zq}\}$  is in the range:  $-k < \text{Re}\{k_{zq}\} < 0$ . In this case, the  $q^{\text{th}}$  harmonic becomes fast and radiates energy in the backward direction but it remains proper ( $\text{Im}\{k_{\rho q}\} < 0$ ). When  $\text{Re}\{k_{zq}\} = 0$ , the radiation is from broadside  $0^\circ$ . As  $\text{Re}\{k_{zq}\}$  becomes greater than 0 and if it is less than  $k$ , the choice for  $k_{\rho q}$  represents a wave radiating in the forward direction (improper leaky wave). Usually, the preceding case for which the wavenumber for a negative harmonic is positive, is met when the periodicity is large enough; greater than half the wavelength.

## 2.8 Deriving the fields

In order to solve for the fields the current coefficients must be found. Therefore, a voltage excitation matrix is formed in the right hand side of Eqn. (2.73). The procedure is to set  $a_{00}^- = 1$ , and normalise all field quantities with respect to it [13]. Eqn. (2.73) becomes

$$[Z'] [C] = [V] \quad (2.86)$$

Similarly, Eqns. (2.76)-(2.79) become

$$Z'_{1k's'ksz} = Z_{1k's'ksz} - \mathcal{B}'_{z00} J_{n_0}(x_0) \tilde{I}_{ks00z} \tilde{I}_{k's'00z}^* \quad (2.87)$$

$$Z'_{1k's'sk\phi} = Z_{1k's'sk\phi} - \mathcal{B}'_{\phi00} J_{n_0}(x_0) \tilde{I}_{sk00\phi} \tilde{I}_{k's'00z}^* \quad (2.88)$$

$$Z'_{2s'k'ksz} = Z_{2s'k'ksz} - \mathcal{B}'_{z00} \frac{k_{z0}^- n_0 r_0}{z_0^{-2}} J_{n_0}(z_0^-) \tilde{I}_{ks00z} \tilde{I}_{s'k'00\phi}^* \quad (2.89)$$

$$Z'_{2s'k'sk\phi} = Z_{2s'k'sk\phi} - \mathcal{B}'_{\phi00} \frac{k_{z0}^- n_0 r_0}{z_0^{-2}} J_{n_0}(z_0^-) \tilde{I}_{sk00\phi} \tilde{I}_{s'k'00\phi}^* \quad (2.90)$$

$$V_{1t} = -J_{n_0}(x_0) \tilde{I}_{00ksz}^* \quad (2.91)$$

$$V_{2t} = -\frac{j}{\eta} \frac{k_{z0}^- n_0 r_0}{z_0^{-2}} J_{n_0}(z_0^-) \tilde{I}_{00sk\phi}^* \quad (2.92)$$

The linear system of algebraic equations Eqn. (2.86) can be solved with the help of an appropriate NAG library routine for matrix inversion. More specifically, the routine S17AEF is employed, which inverts complex matrices using Crout's factorisation [26]. Substitution of the resulted current coefficients into Eqn. (2.47)

and Eqn. (2.48) yields the normalised (to  $a_{00}^-$ ) amplitude field coefficients. The fields can then be calculated.

The  $\rho$  components for the electric and magnetic fields, have not been used so far in the analysis but they are useful for deriving the field lines. Their expressions are

$$E_{\rho}^- = -j \sum_{pq} \left[ a_{pq}^- \frac{k_{zq}}{k_{\rho q}^-} J'_{n_p}(k_{\rho q}^- \rho) + b_{pq}^- \frac{kn_p}{k_{\rho q}^- \rho} J_{n_p}(k_{\rho q}^- \rho) \right] e^{jn_p \phi} e^{-jk_{zq} z} \quad (2.93)$$

$$H_{\rho}^- = -\frac{1}{\eta} \sum_{pq} \left[ b_{pq}^- \frac{k_{zq}}{k_{\rho q}^-} J'_{n_p}(k_{\rho q}^- \rho) + a_{pq}^- \frac{kn_p}{k_{\rho q}^- \rho} J_{n_p}(k_{\rho q}^- \rho) \right] e^{jn_p \phi} e^{-jk_{zq} z} \quad (2.94)$$

## 2.9 Numerical considerations

This section deals with a discussion about any potential difficulties which may arise in the computations. For instance, a machine overflow may arise when trying to calculate a high order field harmonic;  $n_p \gg 1$  and/or  $q \gg 1$ . Then, the corresponding Bessel function will be one of a large order and/or of a large argument. Bessel functions of very large order and/or very large arguments have values which may cause the computer to overflow. The possibility for overflow becomes more pronounced, if the periodicities of the structure are small (i.e. close packing of the elements). Then, the order and/or the argument of the Bessel functions becomes large, rapidly. Quite often, restrictions are also imposed by the NAG algorithms which are used to evaluate the Bessel functions. For all the results presented in this thesis the programs were run in the VPX Fujitsu machine at Manchester Computer Centre. The argument (modulus) of the Bessel, should not exceed the value of 167 every time the S17 family of NAG routines is called by the VPX [16]. Another factor which can result to numerical difficulties is, the limitation by the computers to represent very large or, very small numbers. For example, the limits in the representation of a number in the VPX computer, span from  $\pm 10^{-75}$  to  $\pm 10^{77}$ . To overcome the aforementioned adversities, the following have been used:

1.  $\mathcal{B}_{zpq}, \mathcal{B}_{\varphi pq}, \mathcal{A}_{\varphi pq}$  and  $\mathcal{A}_{zpq}$  given in Eqns. (2.39) to (2.42) are divided by  $J_{n_p}(z_q^-)$ . Following this throughout the next set of equations, the left hand terms in Eqns. (2.58) - (2.63) as well as the right ones in Eqns. (2.76) to (2.79) are divided by  $J_{n_p}(z_q^-)$ .
2. When the limits for the machine overflow are reached, asymptotic expressions are employed to calculate the Bessel functions [27].

A detailed description of the asymptotic expansions for Bessel functions is given in the end of this thesis, in Appendix C.

### ***2.10 Conclusions***

In this Chapter, the theoretical analysis and some numerical aspects needed to describe the problem of propagation inside an FSG's were given. The starting point, was the modal expansion of the total electric and magnetic fields. Next, the induced surface current was expressed by an infinite series of sub-domain basis functions. Using the orthogonal properties of the Floquet series over the periodic unit cell, the spectral coefficients of the current modes were derived. Since an infinite series can not be represented in a digital computer, the total number of Floquet harmonics, as well as the total number of current functions, are defined as a truncated sum. The total field vanishes on the conductor. The latter is tested by the *Galerkin* procedure, and a system of equations is derived. The number of the equations equals the number of the unknown current coefficients. An iterative procedure locates the values of the complex propagation constant for which the determinant is zero. By setting one harmonic to unit amplitude, the resulting non-homogeneous system is solved for the unknown current coefficients and fields. In order to overcome numerical difficulties associated with computers, all field harmonics are normalised to the corresponding Bessel function whereby, analytic asymptotic expressions are employed to calculate higher order field harmonics.

**REFERENCES**

- [1] GOLDSTONE, O., and OLINER, A. A.: 'Leaky wave antennas II: Circular waveguides', IRE Trans. On Antennas and Propagation, Vol. 9, May 1961, pp.280-291.
- [2] CLARRICOATS, P. J. B. and SLINN, K., R.: 'Computer method of determining the propagation coefficient of slotted waveguides', Electron. Lett., Vol. 3, No. 5, May 1967, pp. 191-192.
- [3] SHAFAI, L. and HASSAN, E., E., M.: 'Field solution and electrical characteristics of slotted waveguides', IEE Proceedings-H, Vol. 128, No. 2, April. 1981, pp.87-94.
- [4] CWIK, T. A.: 'Scattering from general periodic screens', Ph.D. thesis, University of Illinois at Urbana-Champaign, May 1986.
- [5] LIER, E.: 'Analysis of soft and hard strip-loaded horns using a circular cylindrical model', IEEE Trans. On Antennas Propagat., Vol. 38, No. 6, June 1990, pp.783-793.
- [6] RONG, Y.: 'Propagation characteristics of circular chirowaveguides periodically loaded with metal gratings', IEE Proceedings-H, Vol. 140, No. 4, Aug. 1993, pp.254-258.
- [7] KISHK, A., A, and KILDAL, P.: 'Asymptotic boundary conditions for strip-loaded scatterers applied to circular dielectric cylinders under oblique incidence', IEEE Trans. On Antennas Propagat., Vol. 45, No. 1, Jan. 1997, pp.51-56.
- [8] OLINER, A. A.: 'Historical perspectives on microwave field theory', IEEE Trans. Microwave Theory Techniques, Vol. MTT-32, No 9, Sep. 1984, pp. 1022-1045.

- [9] COLLIN, R. E. and ZUCKER, F. J. E. 'Antenna Theory, Part 2', Chapter 19, Appendix B, McGraw-Hill, New York 1969.
- [10] MARCUVITZ, N.: 'On field representations in terms of leaky wave modes or eigenmodes', IRE Trans. Antennas Propagation, Vol. AP-4, July 1956, pp.192-194.
- [11] POTHARAZU, P. K., and JACKSON, D. R.: 'Analysis and design of a leaky-wave EMC dipole array', IEEE Trans. On Antennas Propagat., Vol 40, No. 8, Aug. 1992, pp.950-958.
- [12] JACOBSEN, J.: 'Analytical, numerical, and experimental investigation of guided waves on a periodically strip-loaded dielectric slab', IEEE Trans. On Antennas Propagat., Vol. AP-18, No. 3, May 1970, pp. 379-388.
- [13] CLARRICOATS, P. J. B., OLVER, A. D.: 'Corrugated horns for microwave antennas', Peter Peregrinus Ltd., 1984.
- [14] AMITAY, N., GALINDO, V. and WU, C.P.: 'Theory and analysis of phased array antennas', John Wiley, N.Y. 1972.
- [15] VARDAXOGLU, J.C.: 'Frequency Selective Surfaces-analysis and design', 1997 Research Studies Press, Taunton, UK
- [16] HARRINGTON, R. F.: 'Time harmonic electromagnetic fields', Ch. 5, McGraw Hill, New York 1961.
- [17] HARRINGTON, R. F.: 'Matrix methods for field problems', Proc. IEEE, Vol. 55, Feb. 1967, pp. 136-149.
- [18] BALANIS, C. A.: 'Advanced engineering electromagnetics', Wiley, N.Y. 1989.

- [19] RUBIN, B. and BERTONI, H. L.: 'Reflection from a periodically perforated plane using a subsectional current approximation', IEEE Trans. On Antennas Propagat, AP-31, No. 6, Nov. 1983, pp. 829-836.
- [20] MITTRA, R., CHAN, C. H., CWIK, T.: 'Techniques for analysing Frequency selective Surfaces- a review', Proceedings of the IEEE, Vol. 76, No. 12, Dec. 1988, pp. 1593-1615.
- [21] PEARSON, W. L.: 'A technique for organising large moment calculations for use with iterative solution methods', IEEE Trans. On Antennas Propagat, Vol. Ap-33, No 9, Sep. 1985, pp.1031-1033.
- [22] STYLIANOU, A.: 'Iterative computation of scattering from finite and multi-layer frequency selective surfaces', Ph. D. thesis, Loughborough University, June 1992.
- [23] MITTRA, R.: 'Relative convergence of the solution of a doubly infinite set of equations', Journal of Research of the Nat. Bureau of standards-D. Radio Prop., Vol. 67D, No. 2, March-April 1963, pp. 245-254.
- [24] LIU, C-C., SHMOYS, J., HESSEL, A., HANFLING, J. D. and USOFF, J. M.: 'Plane wave reflection from microstrip-patch arrays-theory and experiment', IEEE Trans. On Antennas Propagat, Vol. Ap-33, No 4, April 1984, pp. 426-435.
- [25] MATSUMOTO, M., TSUTSUMI, M., and KUMAGAI, N.: 'Radial characteristics of a dielectric slab waveguide periodically loaded with thick metal strips', IEEE Trans. Microwave Theory Techniques, Vol. MTT-35, No. 2, Feb. 1987, pp. 89-95.
- [26] FUJITSU's 'FORTRAN reference manual for VPX'.
- [27] ABRAMOWITZ, M. and STEGUN, I.: 'Handbook of mathematical functions', Dover Publications Inc., New York, 1954.



# CHAPTER 3

## Cylindrical FSG - one dimensional case

### *3.1 Introduction*

This Chapter deals with the guiding characteristics of cylindrical FSGs, whereby the array is periodic in one direction only. The elements of the FSG are infinitely longitudinal strips or transverse rings. The FSGs are shown in Fig. 3.1 and Fig. 3.8.

The cylindrical FSG geometry with longitudinal strips is presented in Section 3.2. Initially, the analysis is formulated by using the periodicity in one axis for the Floquet expansion whereby, one dimensional triangular or step basis functions are used to approximate the surface current. To simplify things, the propagation

constant is considered real. Predicted dispersion curves are presented for a set of geometric parameters. The convergence of the results is assured by increasing the number of bases and the number of Floquet modes. The propagation constant is then used to derive the fields and the mode patterns. The aforementioned results- assuming real propagation constant- have also been presented in publications [1,2]. Having established some familiarity with the model of single periodic FSG, the following task is to search for the complex propagation constant using the two dimensional analysis. In doing so, a dummy periodicity in the  $z$  direction is assumed. The strips result from dipoles that have their length equal to the dummy periodicity. Two dimensional roof-top basis functions are employed to approximate the current on the dipoles. Predicted results for the complex propagation constant are presented. In order to validate the results, a boundary condition checking is performed.

In Section 3.3 the orientation of the strips is shifted by  $90^0$ , so it produces the FSG with a transverse geometry. As for the longitudinal geometry, one dimensional Floquet and current analysis are employed to model the transverse geometry. Predicted results for real  $\beta$ , are presented and the convergence behaviour of the one dimensional model is closely examined. The two dimensional model, is also applied by assuming a dummy periodicity in the  $\varphi$  axis. Predicted results, obtained by the latter model, are presented for the complex propagation constant and the mode patterns.

Finally, some conclusive remarks are given in Section 3.4.

### ***3.2 Longitudinal geometry***

Fig 3.1 shows the geometry of the one dimensional FSG. The periodicity is defined in the  $\varphi$  axis as  $D_\varphi = 2\pi / N$ ,  $N$  the number of strips placed around  $2\pi$ . The strips are of infinite length, width  $w$  and infinitesimal radial thickness. It should be noted that from this point of the thesis on, metal conductivity is infinite and that in all

cases the arrays are free standing (no dielectric in the body of the waveguide). Hence, the array of strips is considered to be free standing.

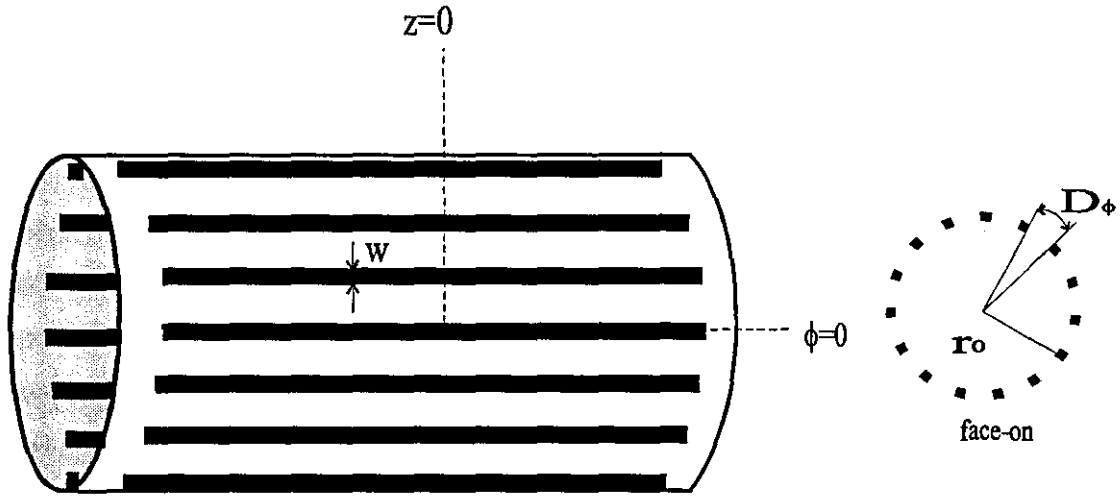


Figure 3.1: Geometry of cylindrical Frequency Selective Guide with  $z$ -directed strips (longitudinal geometry).

### 3.2.1 The 1-D analysis

Floquet modal expansion of the fields, is employed. Due to the absence of the periodicity in  $z$ , the summation over  $q$  in Eqn. (2.16) is removed ( $Q = 0$ ). The summation over  $p$ , indicates the number of wave harmonics, (Floquet modes), in  $\phi$ . The azimuthal variation of these harmonics is determined by the Floquet number

$$n_p = n_0 + N$$

In the above relation, the subscript  $n_0$  denotes the excitation field and  $N$  is the number of strips.

Current is induced in the  $z$  and  $\phi$  directions for a  $z$ -directed TM and a  $z$ -directed TE respectively. Because the strips are infinite in length, there is no dependency in  $z$  for the current. Fig. 3.2 shows the one dimensional triangular and step functions, which are used to expand the current on the strips.

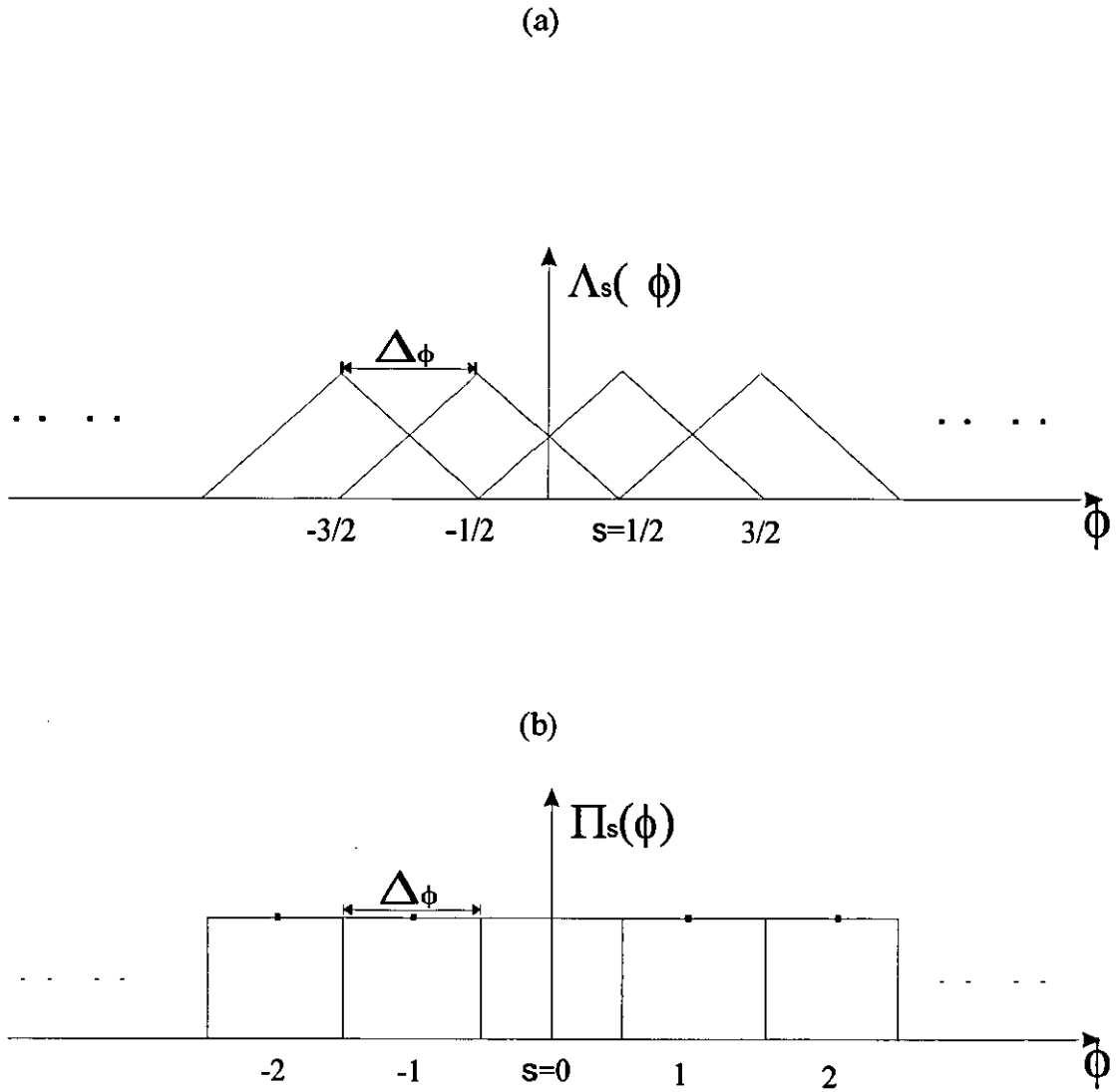


Figure 3.2: Triangular (a) and step (b), basis functions

The strip width is discretised to  $S$  equal subsections. The  $\varphi$  current component is written as a series of  $S-1$  triangular functions weighted by unknown amplitude coefficients  $c_{S\varphi}$ . At the edges this current component, approaches zero.

$$I_{\varphi}(\varphi) = \sum_{-(S-1)/2}^{(S-1)/2-1} c_{S\varphi} \Lambda_{s+0.5}(\varphi) \tag{3.1}$$

The  $z$  current component, is written as a series of  $\mathbf{S}$  step functions, weighted by  $\mathbf{S}$  unknown amplitude coefficients  $c_{sz}$ . Since the current flowing parallel with the strip axis is not zero near the edge, the edge singularity is preserved.

$$I_z(\varphi) = \sum_{-(S-1)/2}^{(S-1)/2} c_{sz} \Pi_S(\varphi) \quad (3.2)$$

The transform of the basis functions (or more accurately the spectral coefficient of the bases), enters the solution process through the calculation of the total fields at the boundary in Eqns (2.60) and (2.61). For the  $s^{\text{th}}$  triangular function the  $p$  spectral coefficient is found from the transform

$$\begin{aligned} \tilde{I}_{sp\varphi} &= \frac{1}{r_0 D_\varphi} \int_{-(s+0.5)\Delta\varphi}^{(s+0.5)\Delta\varphi} c_{s\varphi} \Lambda_{s\varphi}(\varphi) e^{-jn_p\varphi} d\varphi \\ &= \frac{\Delta\varphi}{r_0 D_\varphi} \text{sinc}^2\left(\frac{n_p\Delta\varphi}{2}\right) c_{s\varphi} e^{j(s+0.5)n_p\Delta\varphi} \end{aligned} \quad (3.3)$$

and similarly for the  $s^{\text{th}}$  step function the transform is

$$\tilde{I}_{spz} = \frac{\Delta\varphi}{r_0 D_\varphi} \text{sinc}\left(\frac{n_p\Delta\varphi}{2}\right) c_{sz} e^{jsn_p\Delta\varphi} \quad (3.4)$$

The expression for the spectrum of the  $\varphi$  and  $z$  current, as in Eqns. (2.71) and (2.72) is

$$\sum_{-(S-1)/2}^{(S-1)/2-1} \tilde{I}_{sp\varphi} = \tilde{I}_{\varphi p} \quad (3.5)$$

$$\sum_{-(S-1)/2}^{(S-1)/2} \tilde{I}_{spz} = \tilde{I}_{zp} \quad (3.6)$$

### 3.2.2 Solving for the real propagation constant

In this Section, the mode content for the FSG with longitudinal strips is found by ignoring the attenuation constant. The assumption here is, that the attenuation constant  $a$  for the propagating modes is small so, it can be ignored by the solution without affecting the actual values for  $\beta$ . In so doing, the results are obtained with less calculation effort since, the numerical procedure scans only in  $\beta$ .

There are 36 strips around  $2\pi$  for the free standing array, and the strip width to periodicity ratio is 0.1. The latter parameters appear in reference [3], for a strip loaded circular waveguide. It is assumed that the waveguide is excited by a mode having an  $e^{jn_0\varphi}$  variation with  $n_0 = 0, 1, 2$ . This  $n_0$  appears later as an index in the identification of the modes for example  $H_{n_0m}$ -type or  $E_{n_0m}$ -type.

The width of the strip is discretised in seven equal subsections. Six triangular functions represent the current flowing in the  $\varphi$  direction. For the other current component, there are seven step functions. To calculate the impedance matrix elements in Eqn. (2.75), 701 Floquet modes have been used, in the summations over  $p$ . The ratio number of Floquet modes to number of bases,  $\Delta$ , is about 100. In Fig. 3.3 the dispersion curves are shown for the lowest order hybrid modes. For the 300 frequency steps used to obtain the curves, approximately 1.5 hrs of CPU time was needed. The iterative procedure, scans in  $\beta/k$  between 0.0001 and 1.5 (any solutions above 1 indicate a surface wave) with a step  $\Delta(\beta/k) = k/5000$ , and locates the zeros of the determinant.

For all  $n_0$ , a TEM mode is found to be a solution. This mode is due to the coupling between the strips as, such TEM are found in parallel plate waveguides and coupled striplines, [4]. The other mode solutions found, are fast  $E$ -type hybrid modes.

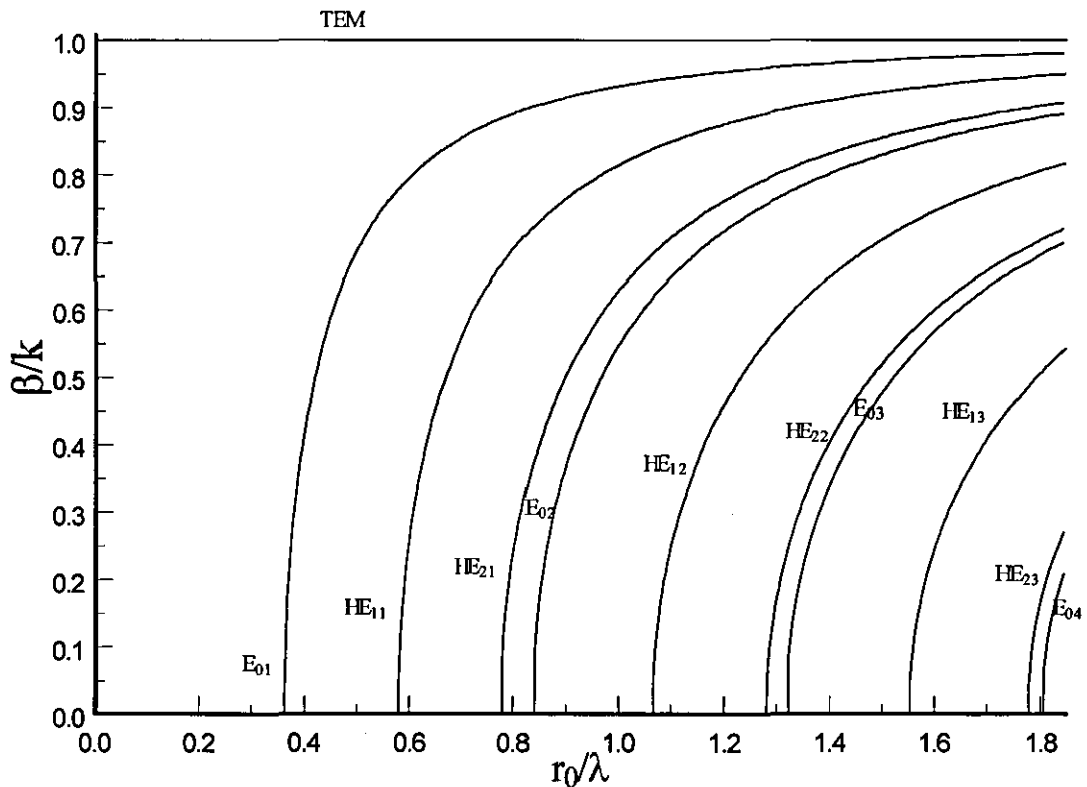


Figure 3.3 :Hybrid modes inside the FSG with longitudinal strips

The numerical convergence of the values of  $\beta$  in Fig. 3.3, is examined by running the program with a different set of input parameters. With  $S=1$ ,  $p=-25$  to 25 (51 Floquet modes) and  $\Delta(\beta/k) = k/500$  the saving in CPU time is massive; the program takes less than 2 minutes to produce the dispersion curves (instead of 1.5 hrs). Moreover, the curves are identical to the ones of Fig.3.3. The latter is justified since, the width of the strips is narrow and one current term is sufficient to represent the current flowing across. Additionally, 51 spectral harmonics are sufficient, to include the spectra of the current which mostly contributes to the summation (see also Section 2.5.2).

### 3.2.3 Calculation of the fields

The predicted propagation constant can be used in order to solve for the current coefficients and the fields, following the method described in Section 2.8. The electric field lines on a transverse plane for each mode are plotted and the modes are identified by observing the patterns.

The transverse electric field components of the single-periodic structure, are written as

$$E_{\varphi}^{-} = \sum_p \left[ a_{p0}^{-} \frac{k_{z0} n_p}{k_{\rho 0}^{-2} \rho} J_{n_p}(k_{\rho 0}^{-} \rho) + b_{p0}^{-} \frac{k}{k_{\rho 0}^{-}} J'_{n_p}(k_{\rho 0}^{-} \rho) \right] e^{jn_p \varphi} e^{-jk_{z0} z} \quad (3.7)$$

$$E_{\rho}^{-} = -j \sum_p \left[ a_{p0}^{-} \frac{k_{z0}}{k_{\rho 0}^{-}} J'_{n_p}(k_{\rho 0}^{-} \rho) + b_{p0}^{-} \frac{kn_p}{k_{\rho 0}^{-2} \rho} J_{n_p}(k_{\rho 0}^{-} \rho) \right] e^{jn_p \varphi} e^{-jk_{z0} z} \quad (3.8)$$

To calculate the fields outside, Bessel functions have to be substituted by Hankel functions of second kind and of the same order. The transverse components of the electric field in Cartesian coordinates are

$$\begin{aligned} E_x &= E_{\rho} \cos \varphi - E_{\varphi} \sin \varphi \\ E_y &= E_{\varphi} \cos \varphi + E_{\rho} \sin \varphi \end{aligned} \quad (3.9)$$

Following Eqns. (3.7) to (3.9), the electric field lines on a transverse plane inside the FSG are plotted for  $\beta = 0$  (cut-off) and for each mode. From these patterns is concluded that the hybrid modes are *E*-type modes, due to their resemblance with the TM modes in a complete cylinder. The mode patterns shown in Fig. 3.4, belong to the HE<sub>11</sub>, HE<sub>21</sub>, HE<sub>12</sub> and HE<sub>22</sub>. In these plots, the disturbances of the lines near the boundary at  $\rho = r_0$ , are due to the fact that the condition for the tangential



electric field to vanish on the conductor is not entirely satisfied. In Section 3.2.6, a boundary condition checking is performed.

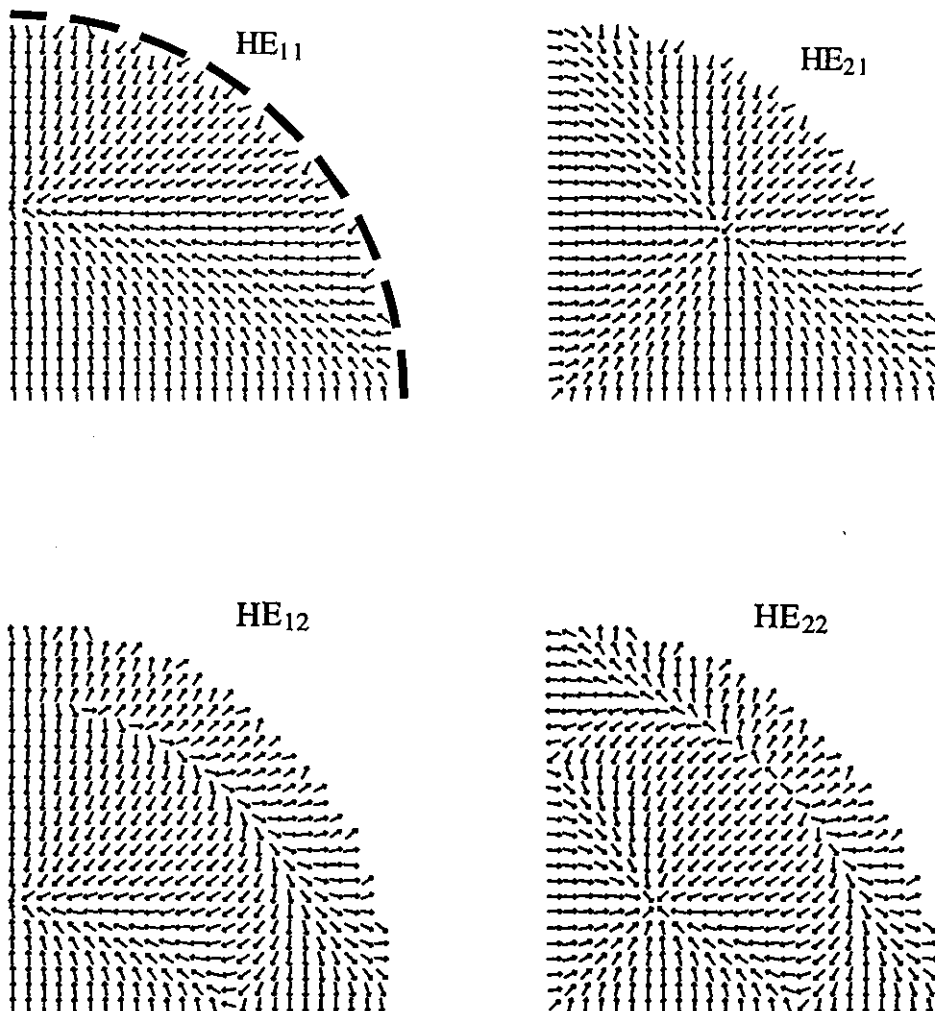


Figure 3.4: Transverse electric field patterns for hybrid modes at cut-off frequency.

### 3.2.4 The 2-D model on a single periodic FSG

The theoretical analysis in Chapter 2, can be applied to model the FSG with longitudinal strips, by considering a dummy periodicity in  $z$ . The parameters are:  $D_\phi = 2\pi r_0 / 36$ ,  $D_z = 0.2r_0$  and  $w = 0.1D_\phi$ . The strips result from an infinite number of joint dipoles. One roof-top function in each direction is used to approximate the currents on the dipole. The roof-top functions, are shown in Fig. 3.5.

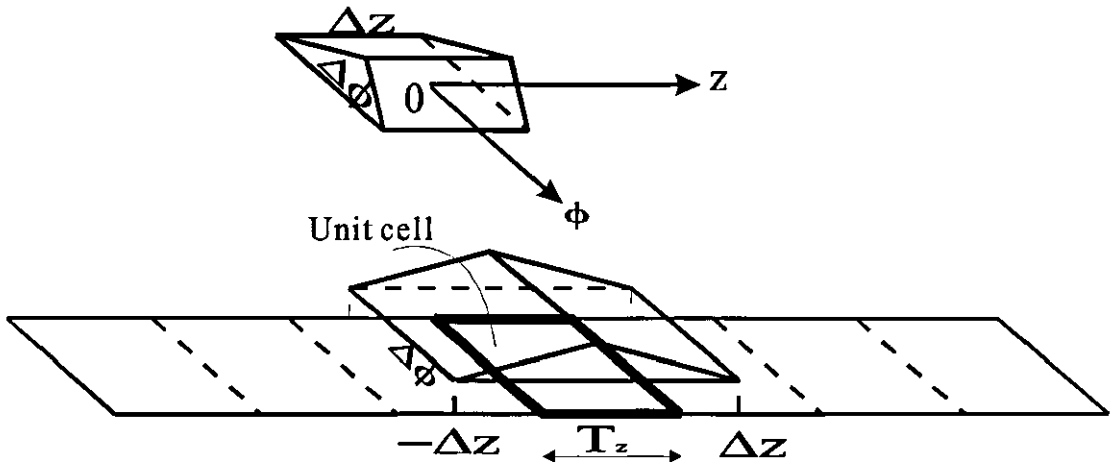


Figure 3.5: Roof-top bases for the currents on joint dipoles (1-D case)

Following from Chapter 2, Section 2.5.2.,  $S = 1$ ,  $K = 1$ . The  $z$ -directed roof-top top extends to the adjacent cell, in order to represent the continuation of the current. The roof-top bases, are centred at the points  $\phi = 0$ ,  $z = 0$ .  $51 \times 51$  Floquet modes are used in the summations over  $p$  and  $q$ , in Eqn. (2.75).

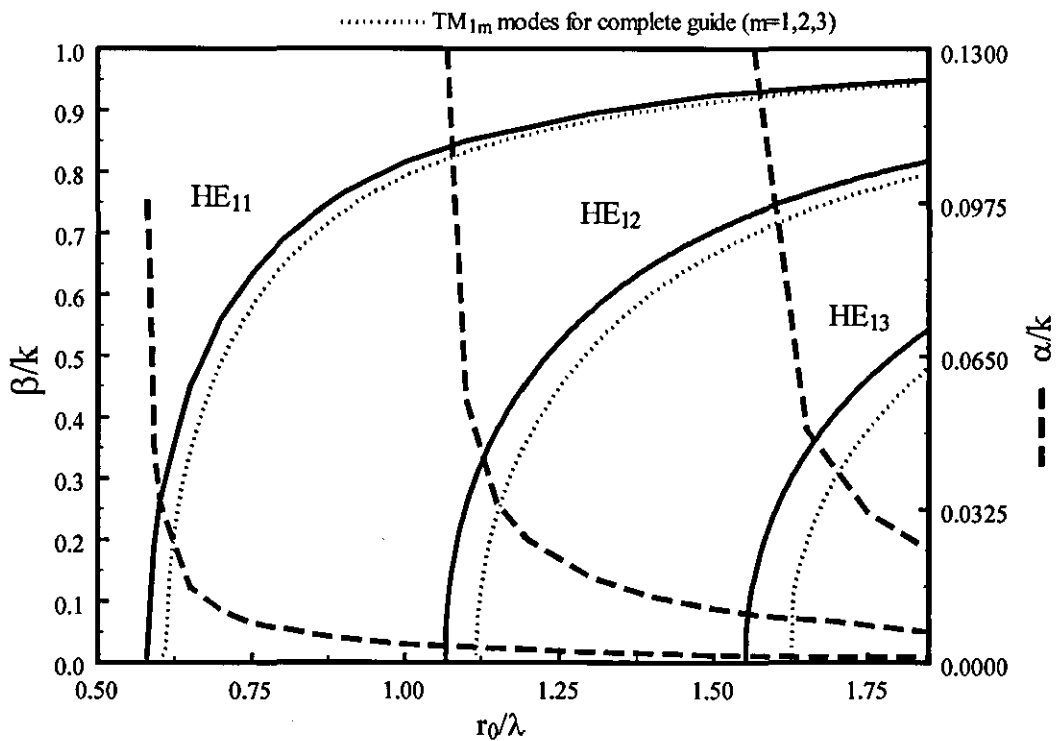
### 3.2.4.1 *Predicted results for complex waves*

Fig. 3.6 illustrates the normalised complex propagation constant versus  $r_0 / \lambda$  of the lowest order hybrid modes and for different excitations. The upper  $x$  axis corresponds to the normalised attenuation constant. The results are obtained by using the two dimensional model with the dummy periodicity. The numerical procedure of Chapter 2, Section 2.6, scans for different values of  $\beta - j\alpha$ , and locates the zero of the determinant. It is evident from this graph, that the values of  $\beta$  are identical to those predicted by the one dimensional model (referred to Fig.3.3).

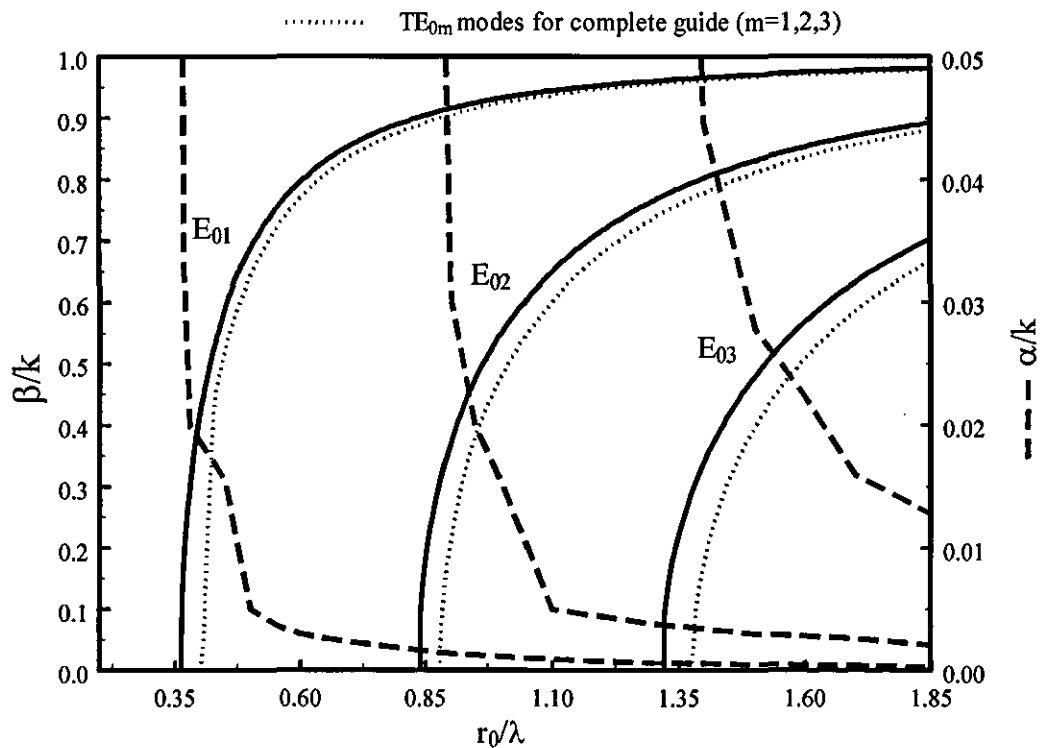
In the same graph, the normalised dispersion curves of the TM modes inside a complete cylinder are also shown. They are obtained from the two dimensional model, by setting  $\Delta\varphi = D_\varphi$ , and extending the  $\varphi$  roof-top function to the adjacent cell. Since the curves are identical with those found in literature [4], the conclusion is that the two dimensional model can be used successfully in the case of a complete cylinder.

The cut-off frequencies of the hybrid HE modes, are below the cut-off frequencies of the TM modes in a closed waveguide. The attenuation constant for these modes in the region near cut-off is high. As frequency increases, the attenuation drops exponentially and tends to zero as frequency increases further. Therefore, the FSG can be used as a uniform leaky wave antenna having the dominant  $HE_{11}$  mode, radiating in free space.

(a)



(b)



(c)

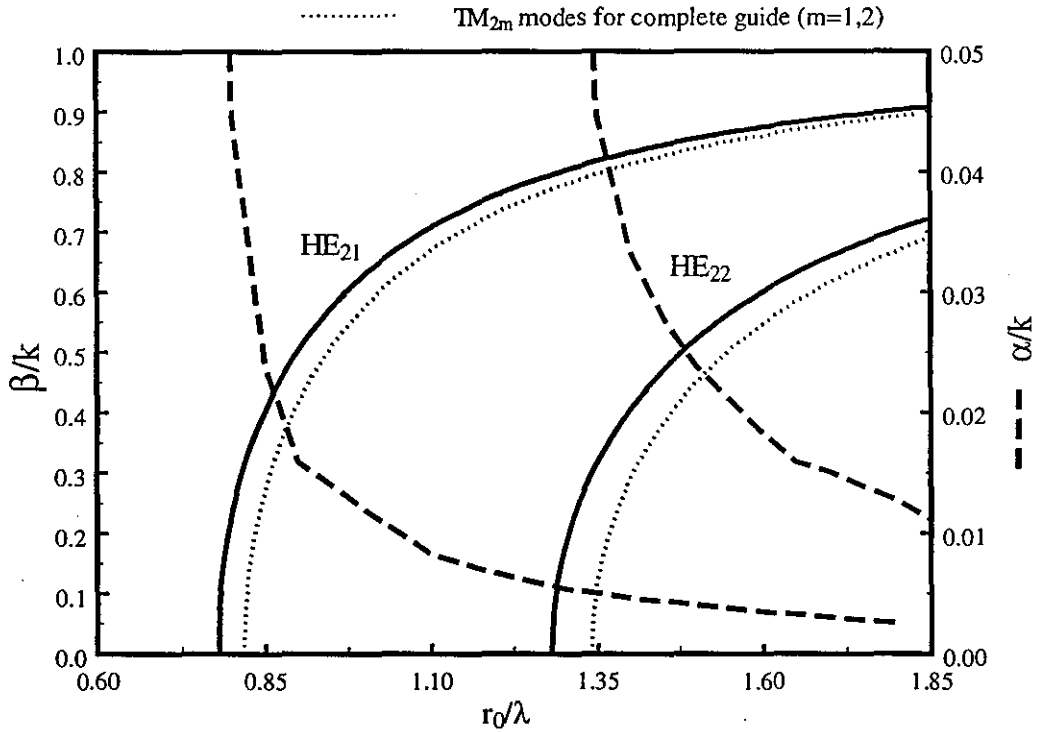


Figure 3.6: Normalised complex propagation constant versus  $r_0/\lambda$  for different excitations (a)  $n_0 = 1$ , (b)  $n_0 = 0$ , (c)  $n_0 = 2$ . ( $N = 36$ ,  $w = 0.1 D_\varphi$ ).

### 3.2.5 The highly attenuated EH modes

EH modes have not been plotted in Fig. 3.6. Such modes are found to be solutions, but are highly attenuated. Their attenuation constant is much greater than for the one shown in the range of Fig. 3.6. An explanation for the weak guidance of EH ( $H$ -type) modes, can be found in previously published references for strip-grids, for example [5]. In EH modes the polarisation is TE-like (electric field along  $\varphi$ ). An incident plane wave having its electric field polarised vertically to a planar grid is transmitted; if the electric field is parallel with the grid then is reflected. Therefore, more than the EH, HE modes will be reflected, (and finally guided), by the internal

walls of the FSG. As shown in Fig. 3.7,  $E_z$  is the dominant electric field component, i.e. TM polarisation.

### 3.2.6 *Checking of boundary condition*

For all the predicted values of  $\beta ja$ , the tangential  $E$ -field components must vanish on the conducting strip, to ensure the validity of the answer. Fig 3.7 shows these components for the  $HE_{11}$  mode at cut-off frequency ( $\beta = 0$ ,  $a = 0.75k$ ). Each component is shown across the strip width (enlarged plot) and across one period. The results for these graphs, have been obtained by using the one dimensional model. Different number of current bases are considered and in each case, the number of bases to number of harmonics ratio is 1/51. It becomes apparent from this graph, that the main electric field component is the one parallel with the strip axis. For the orthogonal electric field component, an edge singularity is observed. An immediate conclusion, from this graph also is, that even though convergence has been accomplished for the values of  $\beta ja$ , with one basis and 51 Floquet modes, the boundary condition is better satisfied if the number of bases and Floquet modes is increased.

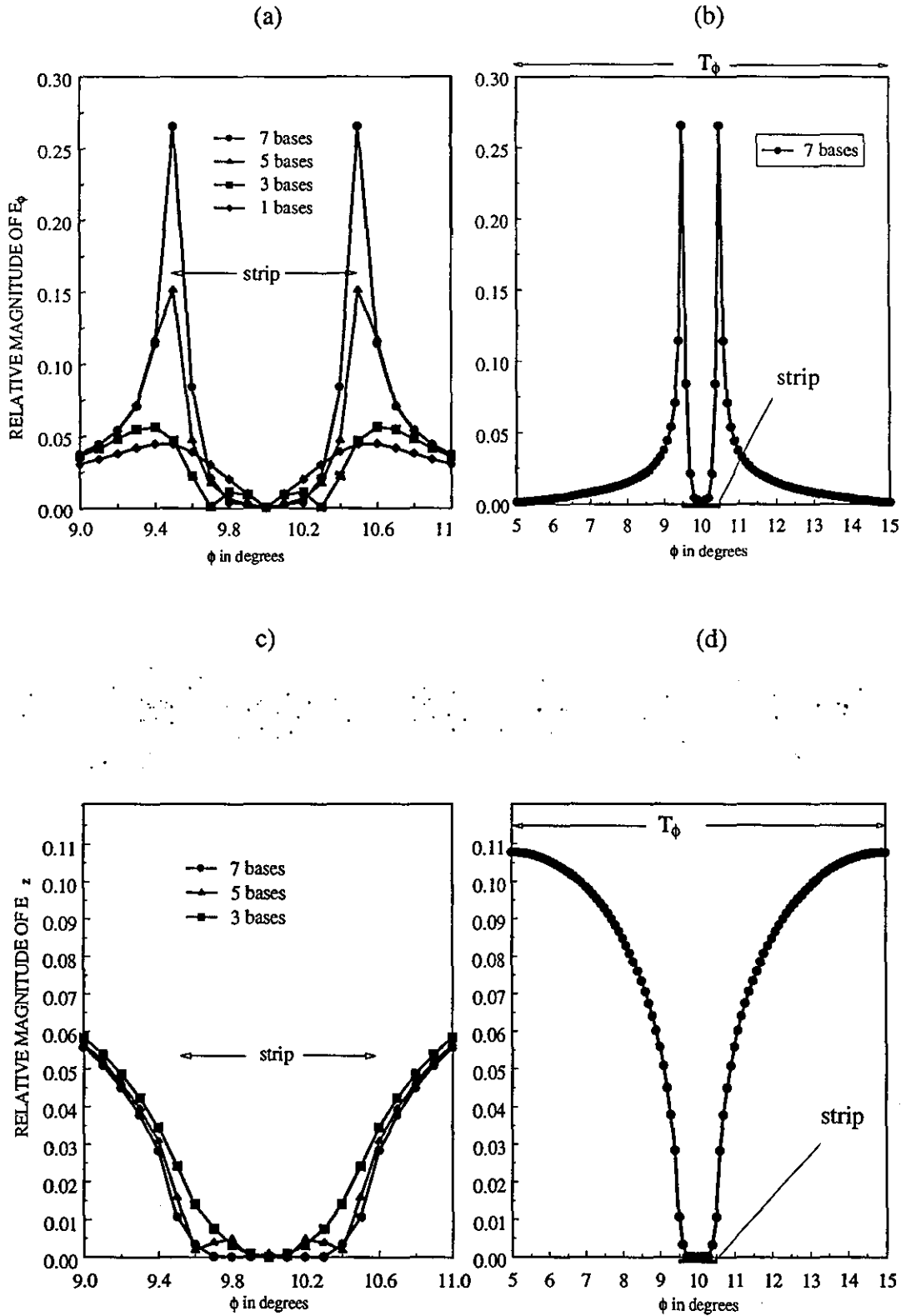


Figure 3.7: Tangential electric field components on the strip for the  $HE_{11}$  mode at cut-off. a)  $E_{\phi}$ -enlarged plot, b)  $E_{\phi}$ , c)  $E_z$ -enlarged plot, d)  $E_z$ .

### 3.3 Transverse geometry

The geometry is shown below in Fig 3.8. The FSG, is a free standing array of circular rings. The distance between successive rings in  $z$ , is the periodicity  $D_z$ . In the same direction the FSG is infinite in extent. The rings have a width  $w$  and  $2\pi r_0$  circumference. They also have infinitesimal radial thickness so that resistive losses can be ignored.

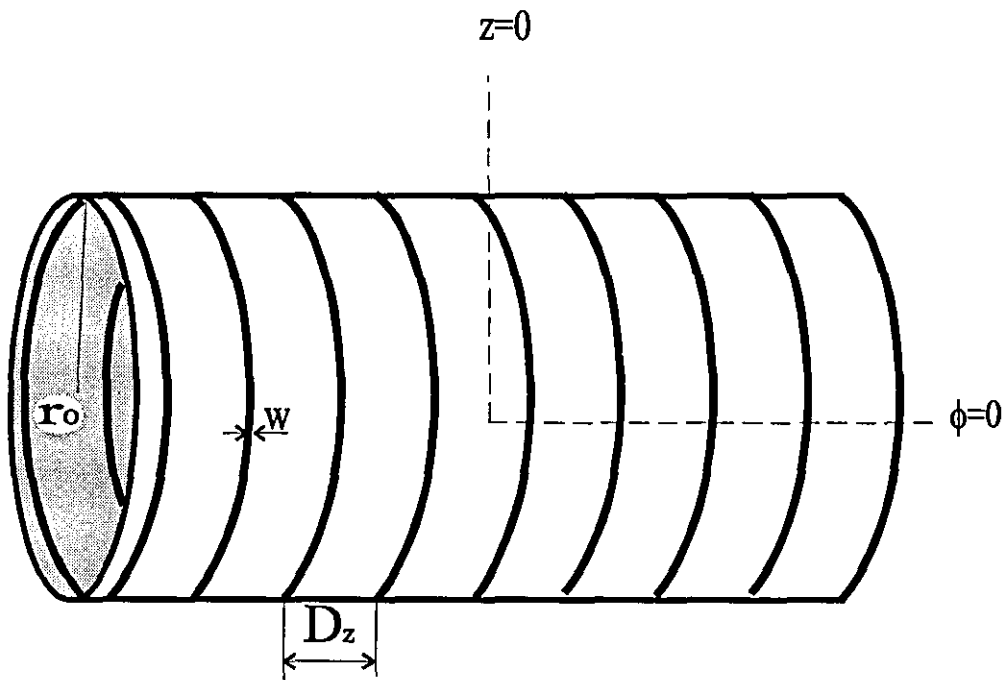


Figure 3.8: Geometry of cylindrical Frequency Selective Guide with  $\phi$ -directed rings.



### 3.3.1 The 1-D analysis

The transverse strip geometry can be analysed similarly to the one with longitudinal strips. As in Section 3.2, the fields are expanded in a series of Floquet harmonics but in the  $z$  direction. The Floquet wavenumber in  $z$  is

$$k_{zq} = k_{z0} + \frac{2\pi}{D_z} q \quad (3.10)$$

Due to the absence of the periodicity in  $\varphi$ , (except the natural  $2\pi$ ), only the basic azimuthal harmonic is present. In the summation in Eqn. 2.16,  $P = 0$ , and  $n_p$  is changed to  $n_0$ .

The current expansion follows also from the longitudinal geometry, by changing the summation limit for the bases from  $\mathbf{S}$  to  $\mathbf{K}$  and the dependency from  $\varphi$  to  $z$ .  $\mathbf{K}$  is the number of subsections across the width of the ring. Triangular functions are used to expand the  $z$  current component and step functions to expand the  $\varphi$ .

$$I_z(z) = \sum_{-(\mathbf{K}-1)/2}^{(\mathbf{K}-1)/2-1} c_{\mathbf{k}z} \Lambda_{\mathbf{k}+0.5}(z) \quad (3.11)$$

$$I_\varphi(z) = \sum_{-(\mathbf{K}-1)/2}^{(\mathbf{K}-1)/2} c_{\mathbf{k}\varphi} \Pi_{\mathbf{k}}(z) \quad (3.12)$$

The transforms of the basis functions,  $\tilde{I}_{\mathbf{k}qz}$  and  $\tilde{I}_{\mathbf{k}q\varphi}$ , are

$$\tilde{I}_{\mathbf{k}qz} = \frac{\Delta z}{D_z} \text{sinc}^2\left(\frac{k_{zq} \Delta z}{2}\right) c_{\mathbf{k}z} e^{-j(k+0.5)k_{zq} \Delta z} \quad (3.13)$$

and

$$\tilde{I}_{\mathbf{k}q\varphi} = \frac{\Delta z}{D_z} \text{sinc}\left(\frac{k_{zq} \Delta z}{2}\right) c_{\mathbf{k}\varphi} e^{-jk_{zq} \Delta z} \quad (3.14)$$

### 3.3.2 Solving for the real propagation constant

For the array in Fig. 3,  $D_z = 0.2r_0$  and  $w$  is  $0.1 D_z$ . It is assumed that the waveguide is excited by a mode having  $e^{jn_0\varphi}$  variation, with  $n_0 = 0, 1, 2$ . This  $n_0$  also appears later, as an index in the identification of the modes. Since the width is small, one triangular function represents the current flowing in the  $z$  direction and one step function represents the current flowing in  $\varphi$ . The limits for the number of Floquet harmonics  $q$ , are  $-25$  and  $25$ ; 51 modes in total. The ratio bases/Floquet modes is  $1/51$ . The convergence for  $\beta$  was examined by i) increasing the number of harmonics to 101 and ii) by increasing the number of bases and Floquet modes to 13 ( $K = 7$ ) and 351 respectively. However, the difference in the results was negligible. Fig. 3.9 shows the dispersion diagrams of the lowest order, fast hybrid modes. The modes are  $H$ -type and their patterns are shown in the following Section 3.3.4.

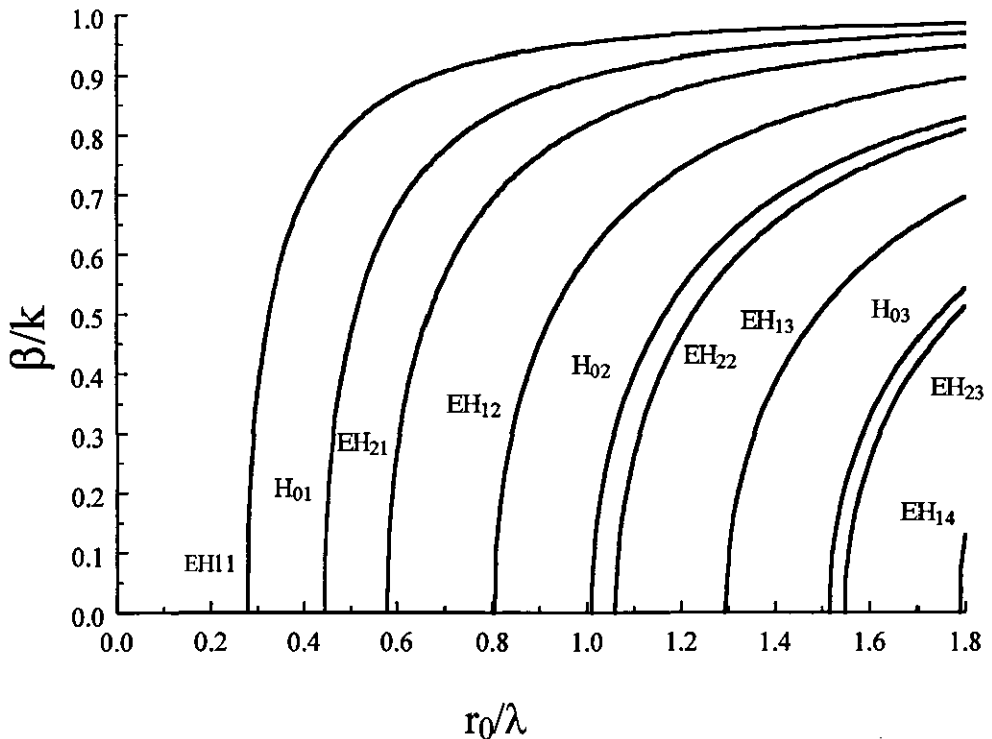


Figure 3.9: Dispersion curves for the hybrid modes inside an FSG with transverse rings.

A surface wave mode, is also found to be a solution for  $n_0 = 1$  (Fig 3.10). This mode is excited by the discontinuity (in  $z$ ) at the boundary, due to the rings. The surface wave does not have a cut-off frequency and at  $r_0/\lambda = 0.1685$ , it reaches a higher cut-off, due to the coupling between the -1 order harmonic and the 0, i.e.  $k_{z0} = -k_{z-1}$  (see Appendix B).

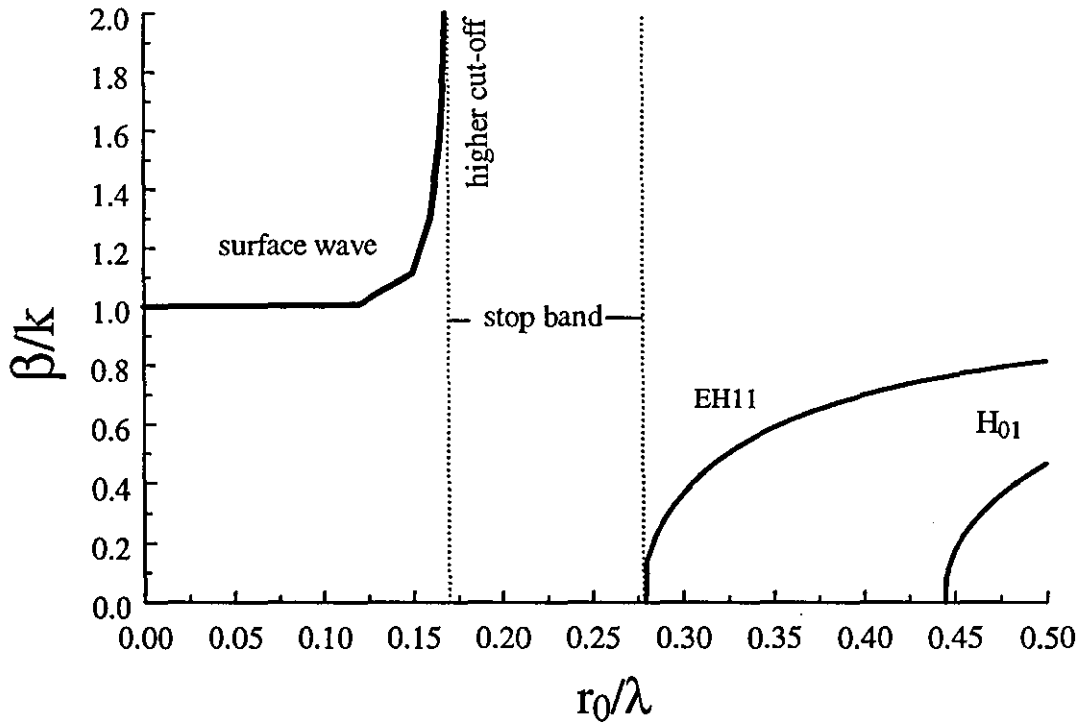


Figure 3.10: Plot showing the surface wave mode, the Bragg condition for this mode and the stop band for the FSG of Figure 3.8 ( $n_0 = 1$ ).

### 3.3.3 Complex waves inside the FSG

The excitation is chosen for  $n_0 = 1$  which is the excitation producing the dominant  $TE_{11}$  mode inside a complete guide. Figure 3.11 illustrates the predicted complex wavenumbers. One roof-top basis is employed for each current and  $51 \times 51$  Floquet modes. The attenuation of the lowest order mode,  $EH_{11}$ , has a minimum at cut-off

( $\beta = 0$ ) and, starts increasing with frequency until  $\beta = 0.6k$ . From this point onwards, the attenuation decreases exponentially as frequency increases. The minimum of the attenuation at cut-off, can be identified as a kind of resonance, due to the sensitivity of the mode to the internal angle of incidence (normal incidence at cut-off). For the other modes, the attenuation is relatively high at cut-off and then decreases rapidly as frequency increases. In the same graph the TE modes of the complete cylinder are also shown. These modes are found by the two dimensional model, setting  $w = D_z$  and adding an extra basis function in  $z$ , which crosses to an adjacent cell. It should be noted, that the cut-off frequencies of TE, occur after those of EH.

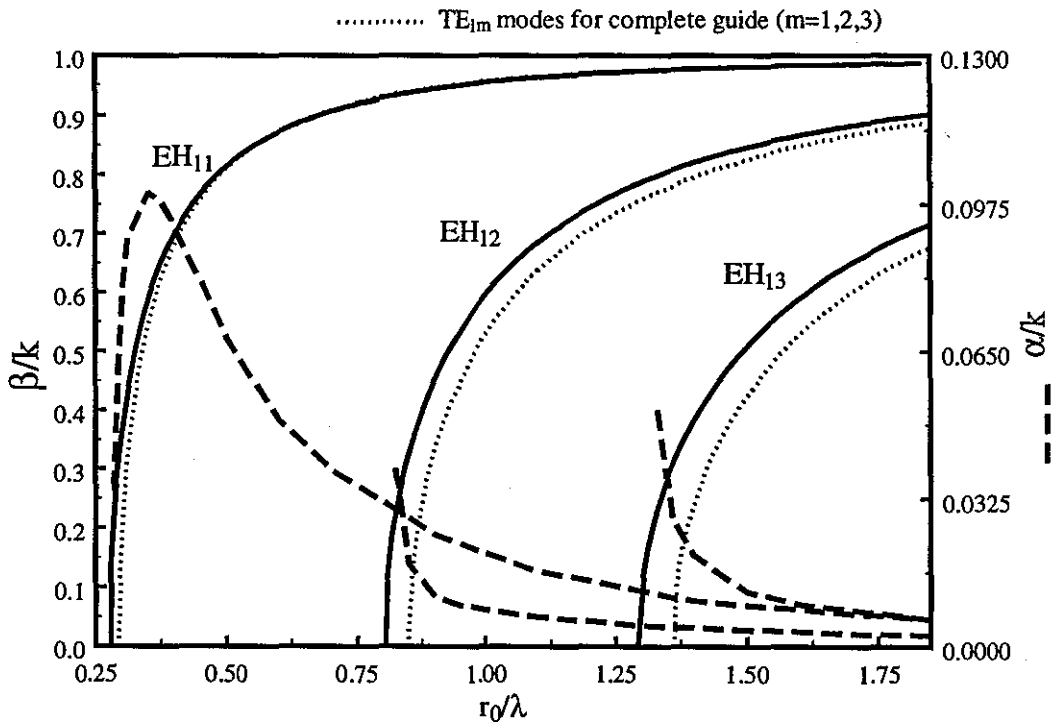


Figure 3.11: Normalised complex propagation constant versus  $r_0/\lambda$  for the FSG ( $n_0 = 1, D_z = 0.2r_0, w = 0.1D_z$ )

### 3.3.4 Field patterns for transverse geometry

After solving for the fields inside the FSG and plotting the transverse electric field lines, the modes are classified as hybrid  $H$ -type modes. The illustrated patterns in Fig 3.12, belong to the  $\text{EH}_{11}$ ,  $\text{H}_{01}$ ,  $\text{EH}_{21}$ ,  $\text{EH}_{12}$  and  $\text{EH}_{22}$  modes. These modes exhibit TE properties at cut-off, i.e. similar patterns to those of TE modes inside a complete cylinder.

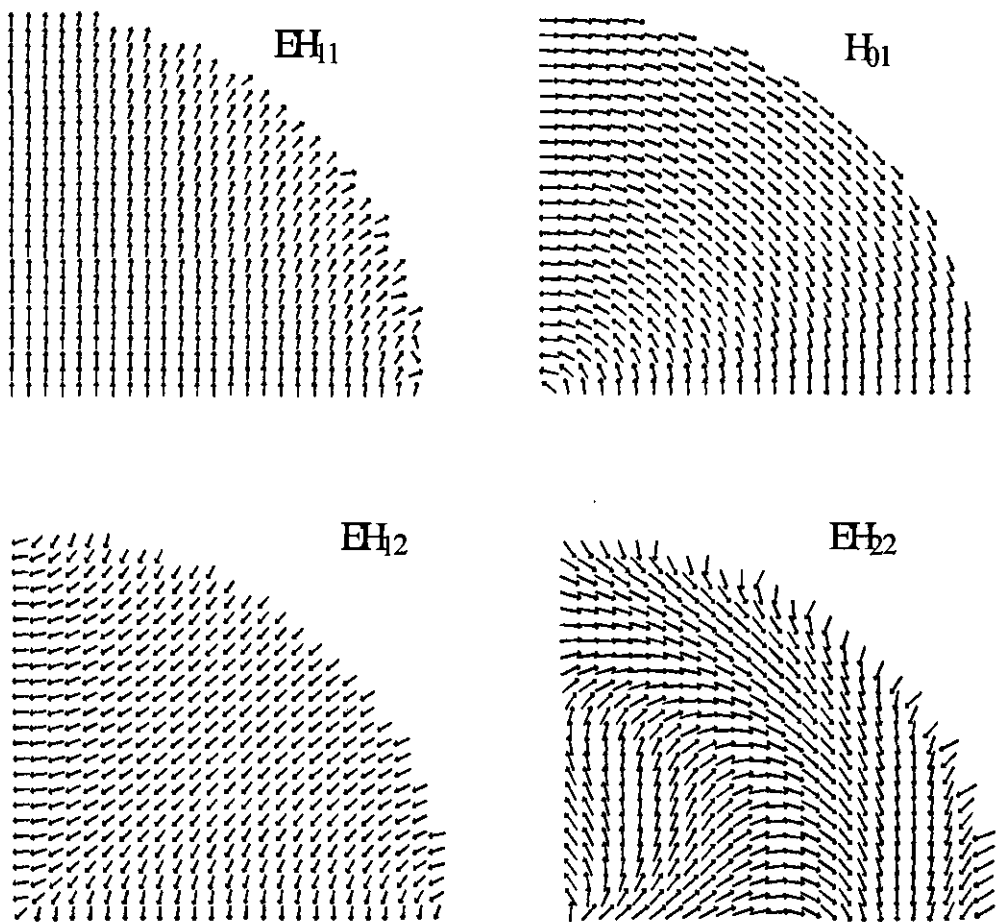


Figure 3.12: Transverse electric field lines of the modes inside the FSG of Figure. 3.8 ( $\beta = 0$ ,  $D_z = 0.1r_0$ ,  $w = 0.1D_z$ ,  $\alpha$  is taken from Fig.3.11)

### 3.4 *Conclusions*

In this Chapter, the propagation inside FSGs with longitudinal and transverse strips has been determined. The general two dimensional analysis, was applied. By collapsing the periodicity in one axis, the one dimensional model was also formed. It was shown, that one can begin to get the picture of  $\beta$  for the less radiating modes, by ignoring the imaginary part. The ability of the analysis to produced stable results was verified by convergence tests. With one basis function for each current, the results are predicted with very little demands in computational time. The modes are hybrid and share similarities for the patterns, with the modes of a complete cylinder. In the case of FSG with longitudinal strips, the TM-like modes are the less attenuated modes whereas for the transverse rings, the polarisation is shifted by  $90^\circ$ . At the examined frequency range, the modes were always leaky, i.e. leaky wave antenna. The attenuation reduces as frequency increases, except at the region near the cut-off of the  $\text{EH}_{11}$ . FSGs with strips also excite a TEM mode whereas, FSGs with rings, excite a surface wave.

Finally, it was concluded that in order to ensure that the electric field is zero on the conductor, more current bases and Floquet modes must be included in the calculations. In the calculation of the propagation constant, the number of current bases and Floquet modes is not so important as, convergence was easily reached.

*References*

- [1] LOUKOS, G. and VARDAXOGLU, J. C.: 'Propagation inside Strip Grating FSS Waveguides with Cylindrical Cross Section, *Electron. Lett.*, 1995, 31, pp. 778-779.
  
- [2] LOUKOS, G. and VARDAXOGLU, J. C.: 'Propagation Characteristics of Frequency Selective Waveguides with Circular Cross Section', *Proc. Joint URSI UK 12th National Radio Science Colloquium and QMW Antenna Symposium, Queen Mary and Westfield College, London 11th-13th July 1995.*
  
- [3] LIER, E.: 'Analysis of soft and hard strip-loaded horns using a circular cylindrical model', *IEEE Trans. On Antennas Propagat.*, Vol. 38, No. 6, June 1990, pp.783-793.
  
- [4] POZAR, D. M.: 'Microwave Engineering', Addison-Wesley Publishing Co., 1990.
  
- [5] KISHK, A. A. and KILDAL, P.: 'Asymptotic boundary conditions for strip-loaded scatterers applied to circular dielectric cylinders under oblique incidence', *IEEE Trans. On Antennas Propagat.*, Vol. 45, No. 1, Jan. 1997, pp.51-56.

# CHAPTER 4

## Cylindrical FSG with dipole elements

### *4.1 Introduction*

In this Chapter, the complex propagation constant is found for FSG with dipoles. The elements are aligned either transversely ( $\varphi$  dipoles) or, in parallel with the direction of propagation ( $z$  dipoles). Dipole elements have been previously used in FSS studies, e.g. [1,2], or, as elements in array antennas, [3-5]. They are an attractive choice due to their manufacture simplicity, resonant behaviour and polarisation purity. Additionally, as a radiator, dipole offers reasonably good bandwidth.



When dipoles constitute the FSG array, the geometry is simple and relatively straightforward to compute. The computational simplicity, is due to the fact that the roof-top function expansion on linear elements, such as dipoles, does not lead to an impedance matrix of large dimension. Arrays of more complex elements can be formed as a superposition of dipole elements, e.g. tripoles, square loops.

Section 4.2 begins with the introduction of the FSG geometry with  $\varphi$  dipoles. The expansion of the current on a dipole is presented in Section 4.2.1. Convergence tests are performed, in order to choose the proper number of basis functions and Floquet harmonics. In Section 4.2.2, predicted results are given for the complex propagation constant of a representative array. The array has 4 elements fitted around the circumference. The separating distance in  $z$  is  $1.047r_0$ . The knowledge of the complex propagation constant, is helpful in investigating the radiating properties of the FSG. This is shown in Section 4.2.3. In 4.2.4, the importance of the design parameters such as, dipole length and periodicity, on the propagation behaviour of the FSG, is studied.

Section 4.3, deals with FSGs with  $z$  dipoles. As in Section 4.2, the subsectional current expansion is outlined, followed by convergence ratios and numerical results for representative arrays. The propagation characteristics of the  $z$ -dipole FSGs are examined for different element lengths and periodicities in  $\varphi$ . In Section 4.3.3, the propagation of higher order harmonics is also investigated.

Finally, conclusions from this study of dipole arrays are presented in Section 4.4.

#### 4.2 FSG with $\phi$ -dipoles

Fig 4.1 shows the geometry of the FSG with transverse dipoles. The dipoles have a length  $L$  in  $\phi$ , narrow width  $w$  in  $z$ , and negligible radial thickness. The radius of the waveguide is 7.85mm, slightly bigger than the conventional  $J$ -band waveguide radius.

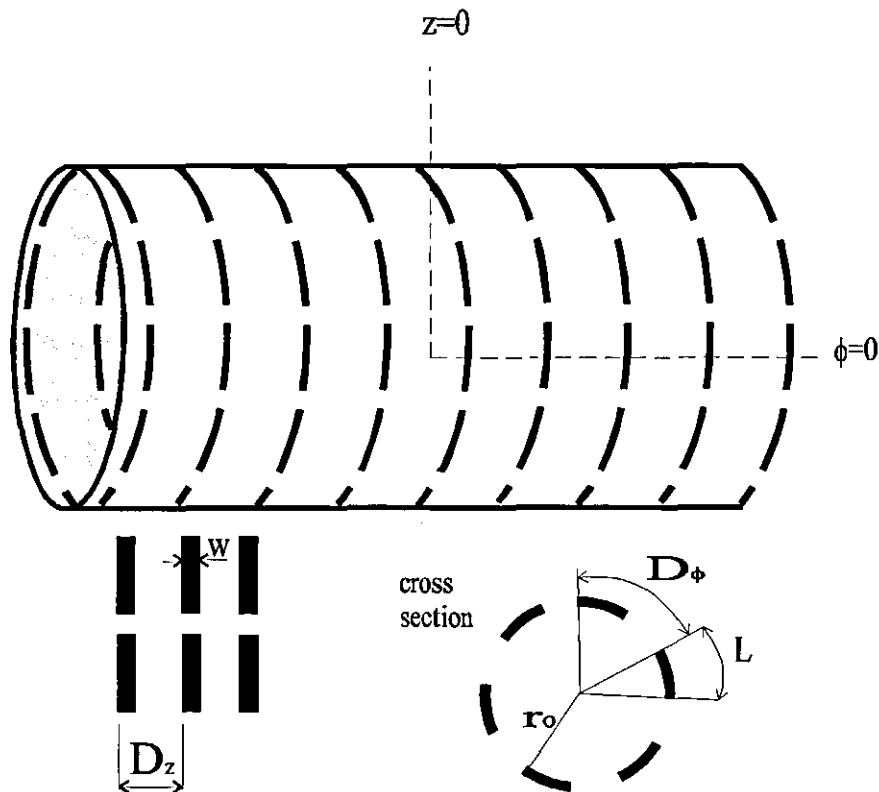


Figure 4.1: Geometry of cylindrical Frequency Selective Guide with  $\phi$ -directed dipoles.

### 4.2.1 Roof-top functions and convergence tests

The roof-top bases on a dipole are shown in Fig. 4.2. Following from Chapter 2, Section 2.5.2.1,  $K = 1$ ,  $S = 7$ . The dipole is discretized into seven equally sized segments. A total of six  $\phi$ -directed bases are defined in order to represent the current flowing along the length. These bases are centred at the points  $z = 0$ ,  $\phi = (s+0.5)\Delta\phi/2$ . For the current flowing in the  $z$ -direction, there are seven roof-top functions centred at  $z = 0$ ,  $\phi = s\Delta\phi/2$ . The  $z$ -directed bases are defined over a single segment whilst, the  $\phi$ -directed bases are defined over two, in order for the current to be zero outside the conductor.

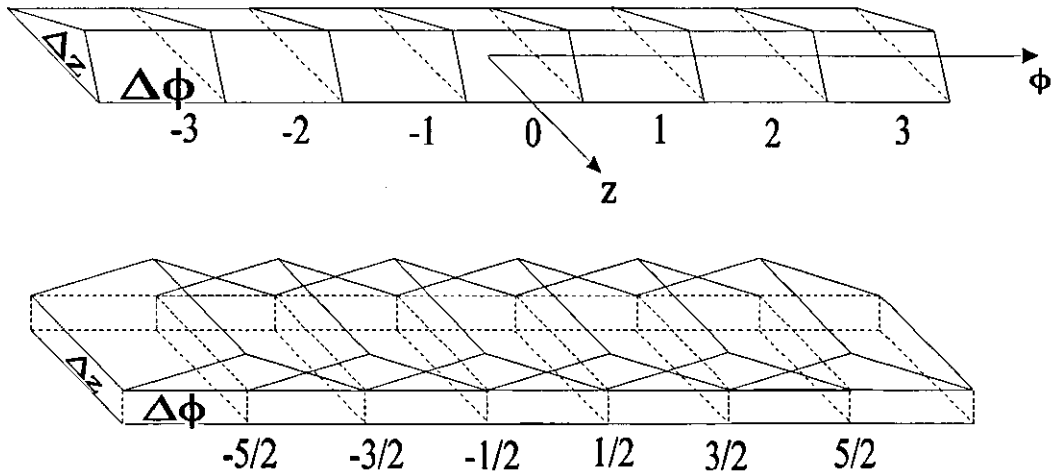


Figure 4.2: Roof top bases on a dipole element

In all simulations presented in the next Section, the parameters are  $K = 1$ ,  $S = 7$ ,  $P = Q = 30$ . With these parameters, results for the complex propagation constant were produced. Convergence of the results was verified by:

i.) changing the truncation limits  $P$  and  $Q$

and

ii) changing the number of bases.

A summation of  $17 \times 17$  Floquet terms, ( $P = Q = 16$ ), gave results for the complex propagation constant, slightly different (about 5%), from those obtained by a summation over  $31 \times 31$  modes whereas, the difference between results obtained by a summation over  $31 \times 31$ , and  $101 \times 101$  terms was found to be insignificant.

In order to increase the number of bases, the dipole length was discretised to 11, 15 and 21 subsections, ( $K = 1$ ,  $S = 11, 15, 21$ ). For each segmentation,  $101 \times 101$  Floquet modes were used, but the difference in the results was found to be insignificant.

To derive the points on a dispersion curve the iterative procedure proposed in Chapter 2, (Section 2.6), was used. Approximately 1 minute of CPU time in the VPX computer was needed for each frequency scan, when,  $31 \times 31$  Floquet modes and 13 bases were used.

#### 4.2.2 Numerical results for representative array

Plotted in Fig. 4.3 are predicted results for the propagation and attenuation characteristics, of the basic ( $q = 0$ ) harmonic, of an FSG with a  $\varphi$  dipole arrangement. The dipole array has the following parameters:  $L = 11.75\text{mm}$ ,  $D_\varphi = 12.33\text{mm}$ ,  $D_z = 8.22\text{mm}$ ,  $L/D_\varphi = 0.952$ .  $w = 0.1 D_z$  and there are 4 elements around  $2\pi$ .  $\beta$  and  $\alpha$  are normalised with respect to the periodicity.

At low frequencies the numerical procedure finds only real solutions. These solutions represent a proper surface wave mode with no cut-off. The surface wave is excited by the discontinuity of the dipole array. Due to the same discontinuity, the surface wave becomes unbounded and finally stops when mode coupling effect occurs. The condition for mode coupling is met at 11.3 GHz (upper cut-off). After this frequency, the surface wave becomes complex and a stop band occurs. The attenuation constant near the upper cut-off is depicted in Fig. 4.5.

The cut-off frequency of the first fast wave mode is at 12.4 GHz. The wave has complex propagation constant and at cut-off, the attenuation is high. The mode is identified as the hybrid  $EH_{11}$  mode, from the transverse electric field lines shown in Fig. 4.4. The other curve shown in Fig. 4.3 is the  $TE_{11}$  line of the complete cylinder having the same radius.

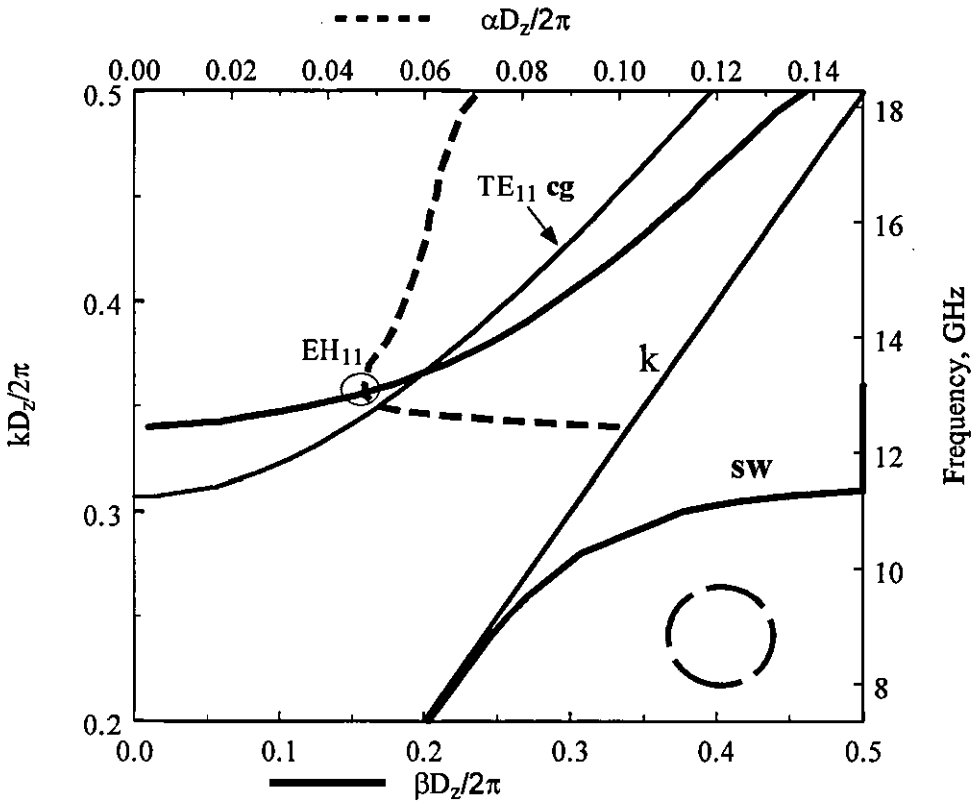


Figure 4.3: Dispersion curves for an FSG with 4 dipoles in  $\varphi$  ( $L = 11.75\text{mm}$ ,  $D_\varphi = 12.33\text{mm}$ ,  $D_z = 8.22\text{mm}$  apart,  $w = 0.1 D_z$ ).

The resonance of the element is identified by inspecting the dispersion curves. At 12.8 GHz, the imaginary part of the complex propagation constant goes to a minimum. Close to that frequency, at 13 GHz, the curve of the real propagation constant of the mode, crosses the  $TE_{11}$  line of the complete cylinder. The latter can

be justified, since at resonance the dipole array becomes more reflective, approaching the behaviour of a continuous wall. In this case, more power is guided inside the FSG and less is allowed to radiate outside. The element length to the wavelength of resonance ratio is  $\frac{L}{\lambda_r} \cong 0.5$ , which agrees with the resonance condition applied to general FSS dipoles.

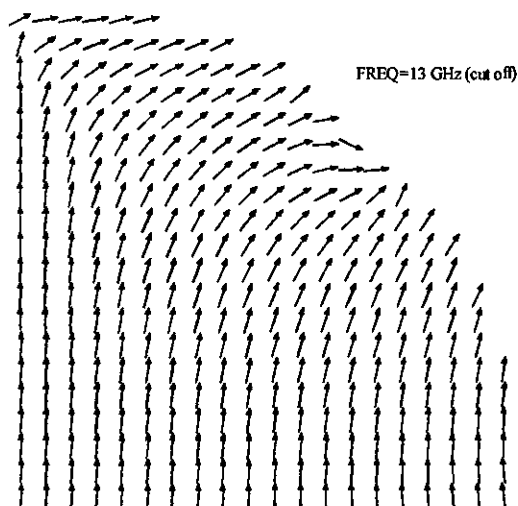


Figure 4.4: Transverse electric-field patterns of EH<sub>11</sub> mode at cut-off frequency (referred Fig. 4.3).

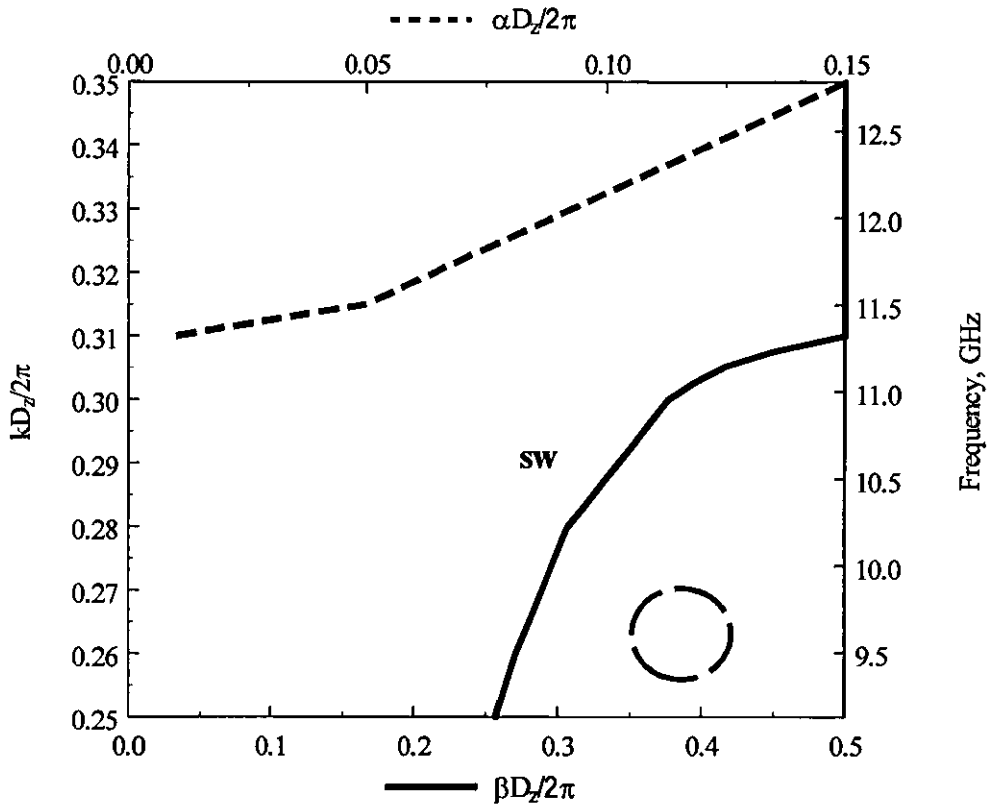


Figure 4.5: The imaginary part of the attenuation constant for the surface wave mode at the Bragg condition.

The complex coefficients of the roof-top bases can be found, by introducing a voltage excitation and inverting the impedance matrix. (Chapter 2, Section 2.8). Plotted in Fig. 4.6 is the calculated magnitude of a  $\varphi$ -directed roof-top function, against periodicity in  $z$  over wavelength. The roof-top basis is centred at  $z = 0$  and  $\varphi = \Delta\varphi/2$ . In the same figure the attenuation curve is also shown. The conclusion is that current reaches a maximum as the attenuation descends before the resonance thus, augmenting the reflecting properties of the FSS wall. The amplitude of the current function starts decreasing at resonance and continues to drop as  $a$  increases after resonance.

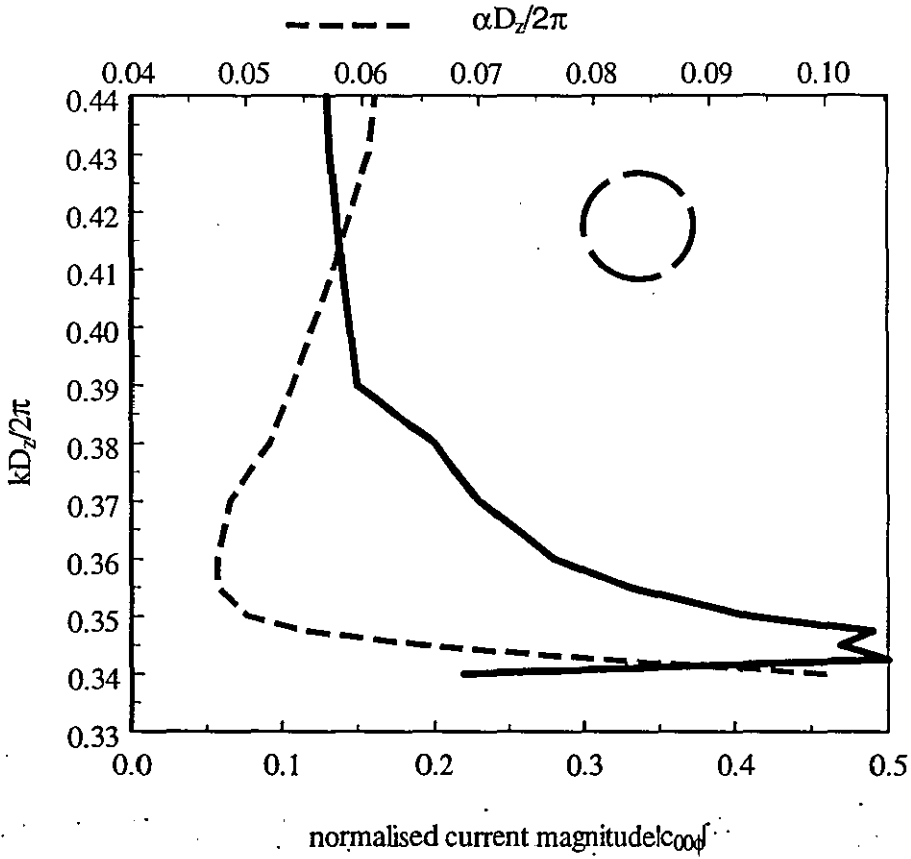


Figure 4.6: Relation between the main roof-top for the current flowing in the  $\phi$  direction and the attenuation constant

### 4.2.3 The dipole array as a leaky wave antenna

The knowledge of the complex propagation can yield the angles of the radiating beams from the FSG. The angle  $\theta$  (Appendix B) of the main radiating beam for the EH<sub>11</sub> mode, is found with the aid of the formula

$$\theta = \sin^{-1} \frac{\beta}{k}$$

and is plotted against frequency. At cut-off the radiation is from broadside at  $0^\circ$ . As frequency increases, there is always a radiating beam scanning in the forward



direction from  $0^{\circ}$  towards  $90^{\circ}$  as  $\beta$  approaches  $k$ . It should be noted, that in this frequency range, the only fast radiating harmonic is the basic (zero order). Higher order harmonics are slow and do not contribute to the radiating field, e.g. for the next higher order harmonic  $\text{Re}\{k_{z-1}\}D_z/2\pi = (\beta D_z/2\pi) - 1 < -0.5$  (slow).

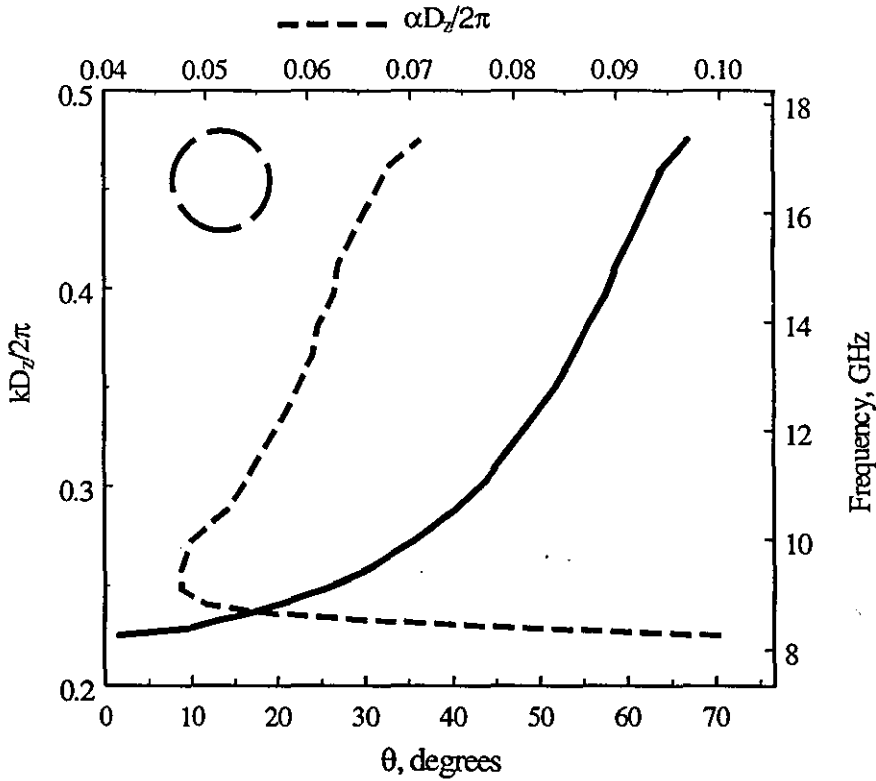


Figure 4.7: Frequency scanning of the radiation angle for the uniform leaky waveguide measured from the broadside.

#### 4.2.4 Parametric study on $\varphi$ -dipole arrays

In this Section the design parameters dipole length, number of elements in  $\varphi$  and the periodicity in  $z$ , are varied. The impetus is to study the effects of these parameters on the propagation behaviour of the FSG. The different designs are marked A, B, C, D and E and their parameters are shown in Table 4.1.

	Case A	Case B	Case C	Case D	Case E
$N$	4	6	6	2	2
$D_\varphi$	12.33	8.22	8.22	24.66	24.66
$L$	11	7.8	7.85	23.55	23.55
$D_z$	8.22	8.22	2.355	2.355	8.22
$w$	0.822	0.822	0.2355	0.2355	0.822

$N$  number of elements in  $\varphi$

$D_\varphi$  periodicity in  $\varphi$  \*

$L$  length of the dipole \*

$D_z$  periodicity in  $z$  \*

$w$  width of the dipole \*

\*  $D_\varphi, L, D_z, w$  are measured in mm

Table 4.1: Parameter variations for the five cases of FSGs with  $\varphi$ -dipoles modelled.

## CASE A

Fig. 4.8 shows, the complex propagation curves for the dimensions of Fig. 4.3 and one where the dipoles have been reduced in length (from 11.75mm to 11mm). The periodicities in  $z$  and  $\phi$  are kept as before:  $D_z = 12.33\text{mm}$  and  $D_\phi = 12.33\text{mm}$  respectively. The effect is that both the higher cut-off of the surface wave mode and the cut-off of the hybrid  $\text{EH}_{11}$  mode, have been shifted at higher frequencies i.e. the higher cut-off for the small dipole array is at 12 GHz, about 0.7 GHz higher than the one for the longer dipole. The cut-off frequency of the  $\text{EH}_{11}$  is at 13 GHz whereas, at 13.75 GHz, the short dipole resonates and  $\alpha$  goes to a minimum. This is because the smaller dipole resonates at higher frequencies. In both cases the ratio dipole length to wavelength of resonance is about 0.5.

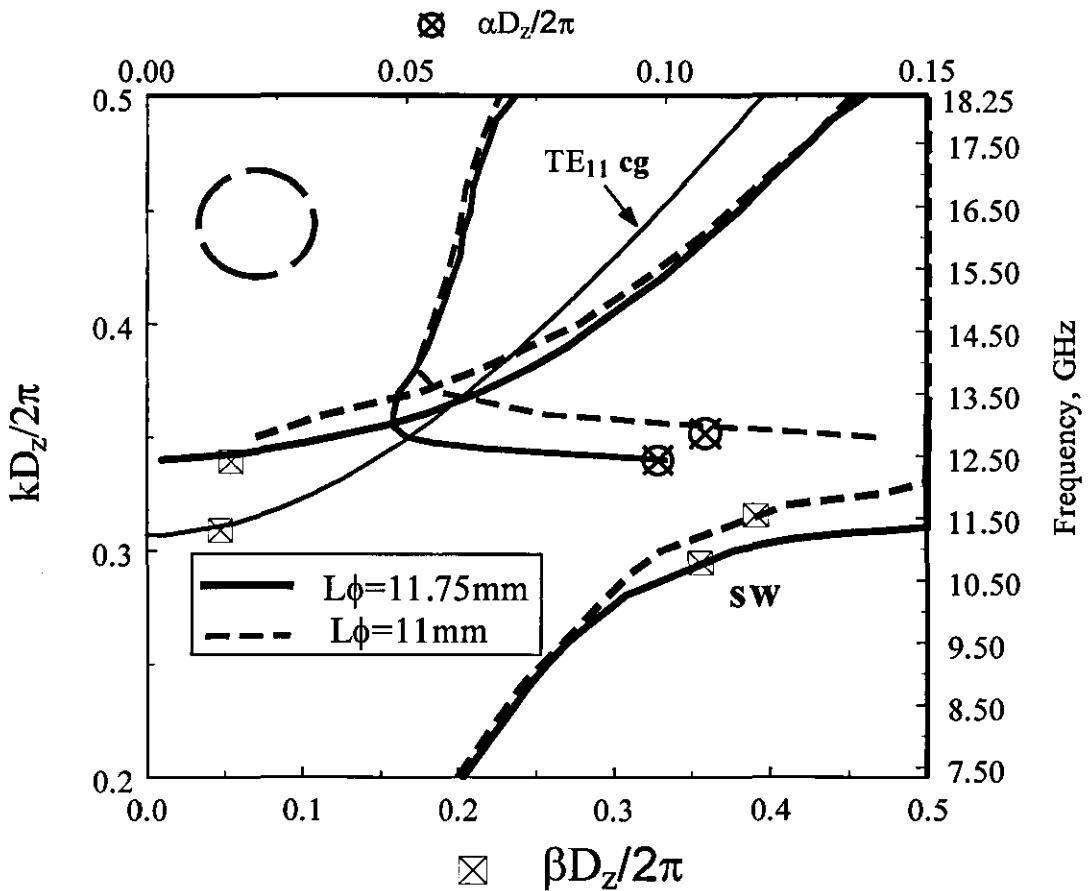


Figure 4.8: Complex propagation constant for  $\phi$  dipole arrays of different length.

CASE B

By increasing the number of elements around  $2\pi$ , the size of the dipoles can be reduced. For the results shown in Fig. 4.9, 6 dipoles are fitted around the circumference ( $D_\phi = 8.22\text{mm}$ ). The ratio  $L/D_\phi$  is kept as before ( $=0.952$ ), thus the new length is 7.8mm. The resonance for the hybrid  $\text{EH}_{11}$  mode is shifted at 17 GHz and the upper cut-off for the surface wave mode is shifted at 14.6 GHz. Additionally, comparison of the  $\alpha$  curves in Fig. 4.9, indicates lower attenuation at resonance for the case of  $D_\phi = 8.22\text{mm}$

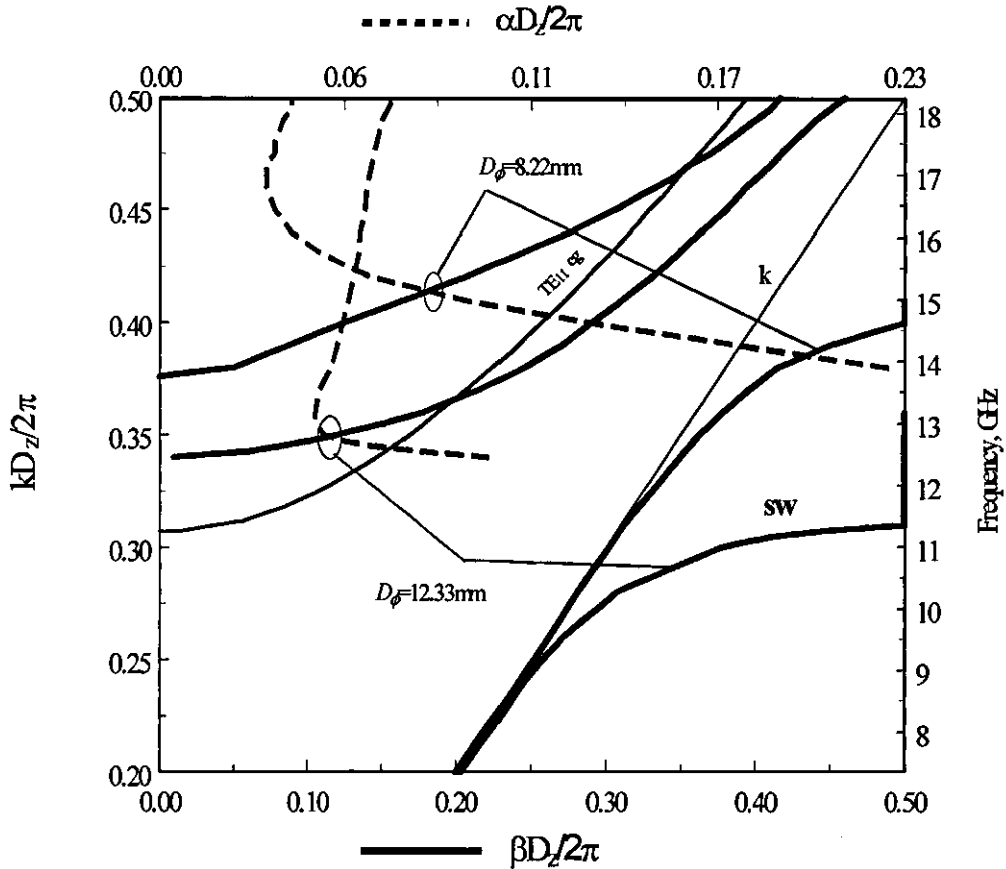


Figure 4.9: Real propagation and attenuation constant for two  $\phi$  dipole arrays with different periodicities in  $\phi$ .  $L / D_\phi = 0.95$ ,  $D_z = 8.22\text{mm}$ ,  $w = 0.1 D_z$ .

## CASE C

Next the periodicity in  $z$  for the 6 dipole array is decreased resulting in closer packing of the elements. Fig. 4.10 shows predicted results for the complex propagation constant when the parameters are:  $D_\phi = 8.22\text{mm}$ ,  $L = 7.85\text{mm}$  and  $D_z$

$= 0.3r_0 = 2.355\text{mm}$ . The condition  $\frac{D_z}{\lambda} = 0.5$  is met at about 64 GHz. The surface wave which propagates at low frequencies, reaches a higher cut-off due to the effect of the periodicity at 19 GHz. The following three leaky wave modes are the hybrid  $H$ -type modes  $\text{EH}_{11}$ ,  $\text{EH}_{12}$  and  $\text{EH}_{13}$ . The attenuation constant at cut-off frequency for each of these modes, is very large. These cut-off frequencies could not be derived due to numerical deficiencies of the model, e.g. the starting point for the  $\text{EH}_{11}$  curve is at 15 GHz for which  $\beta/k = 0.4$  and  $\alpha/k = 0.25$ .

The  $E$ -type hybrid modes are highly attenuated and therefore, not plotted. The case is similar to that of the ring FSG of Chapter 3.

The element resonance for the  $H$ -type modes are identified in the familiar way, by determining the minima of  $a$  curve. For the  $\text{EH}_{11}$  mode the element resonates at 25 GHz, 37.5 GHz and 50 GHz. The ratios  $\frac{D_z}{\lambda}$  for these frequencies are about 0.2, 0.3 and 0.4 respectively. For the  $\text{EH}_{12}$ , mode the first resonance is at  $\frac{D_z}{\lambda} = 0.3$  and the second resonance at  $\frac{D_z}{\lambda} = 0.44$ . For the  $\text{EH}_{13}$  mode the resonance is found at  $\frac{D_z}{\lambda} = 0.48$ .

Summarising observations from the previous paragraph, one can say that closer packing of elements shifts the resonance of the dipole array at higher frequencies. By reducing the periodicity in  $z$ , more frequencies are included until the condition  $D_z / \lambda = 0.5$  is met. For each hybrid mode, the dipole resonates more than once.

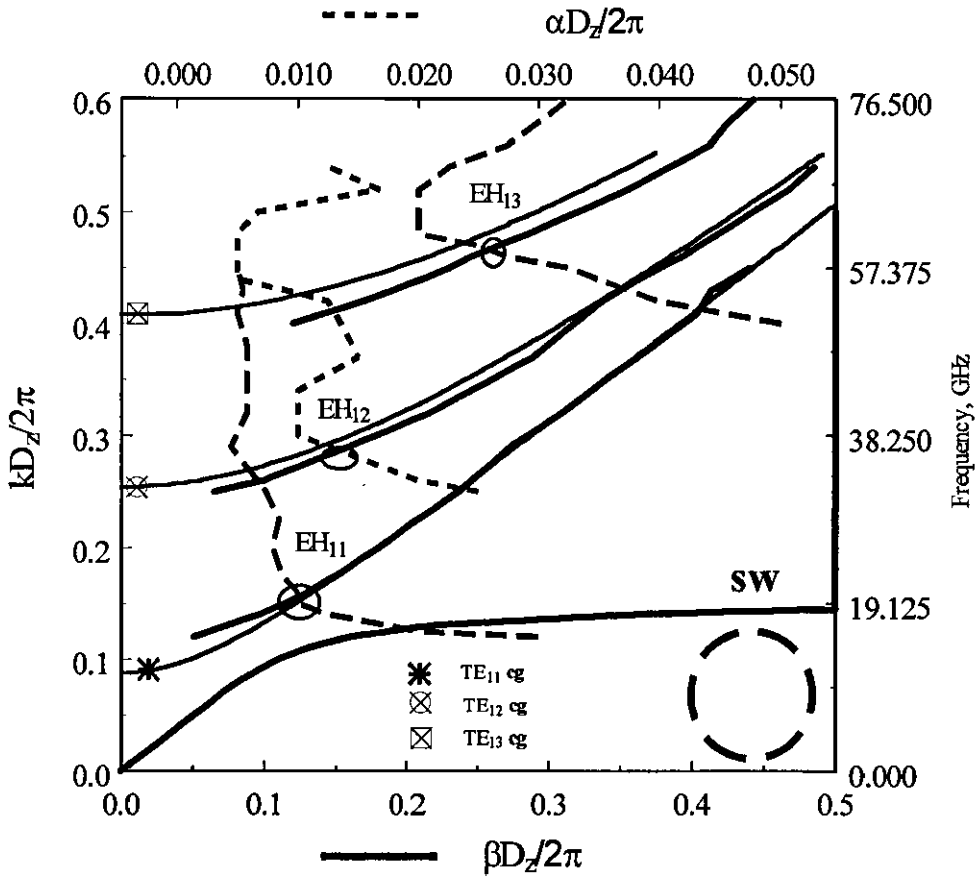


Figure 4.10: Complex propagation constant for FSG with  $\varphi$ -dipole arrangements ( $D_\varphi = 8.22\text{mm}$ ,  $L = 7.85\text{mm}$ ,  $D_z = 0.3r_0 = 2.355\text{mm}$ ,  $r_0 = 7.85\text{mm}$ )

CASE D

The dipole is increased in length. Two dipoles are placed around the circumference which results in a periodicity of 24.66 mm. The periodicity in  $z$  is 2.355mm. The dipole length extends to the 95 % of the periodicity in  $\varphi$  ( $= 23.5\text{mm}$ ).  $\lambda_r = \frac{L}{2}$  gives a frequency  $f_r = 2.55$  GHz. Fig. 4.11 shows the predicted real part of the propagation constant for the modes propagating inside the FSG. In the same graph the corresponding TE and TM modes of the complete cylinder are also plotted. The

imaginary part of the propagation constant for these modes is shown in a different graph in Fig. 4.12. The surface wave reaches a higher cut-off condition at about 12.8 GHz. The cut-off for the  $\text{EH}_{11}$  mode is found at 10.4 GHz whereas, the cut-off of the  $\text{TE}_{11}$  mode of the complete cylinder is at about 11.3 GHz. The resonance for this mode is very close to the cut-off frequency, at a wavelength which is about  $4\lambda_r$  (10.5 GHz). In Fig. 4.13, the area near the cut-off of the first  $\text{EH}_{11}$  mode in Fig. 4.12 has been enlarged to depict the resonance.

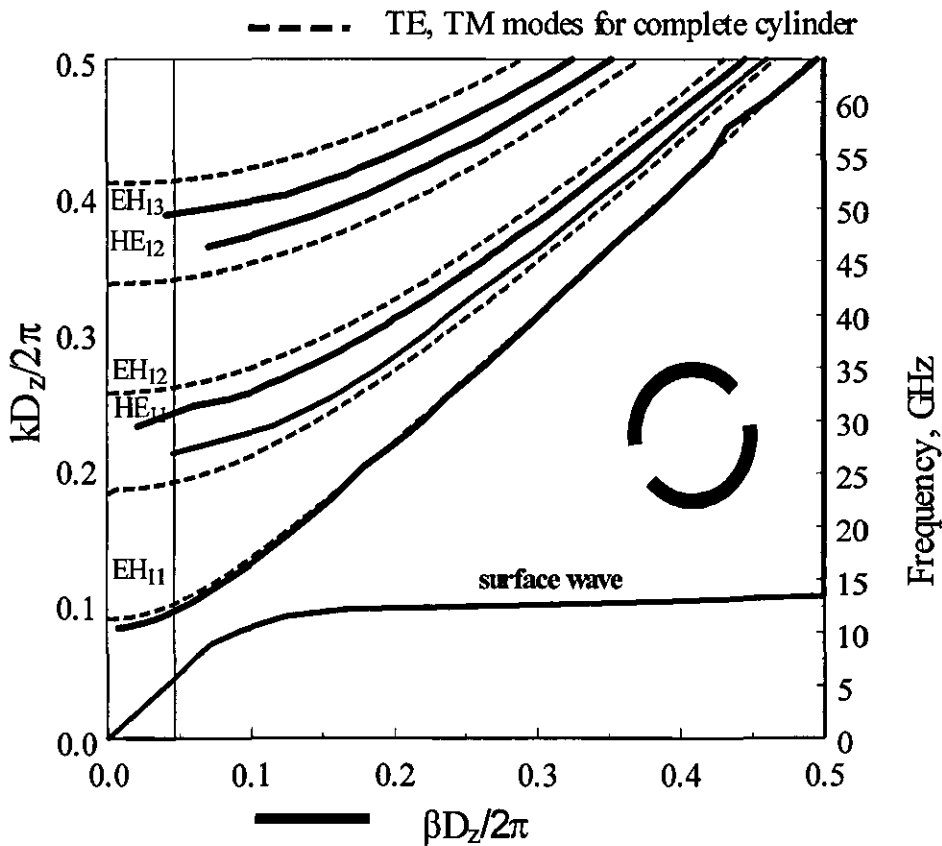


Figure 4.11:  $\beta$  curves for FSG with two dipoles and the complete cylinder.

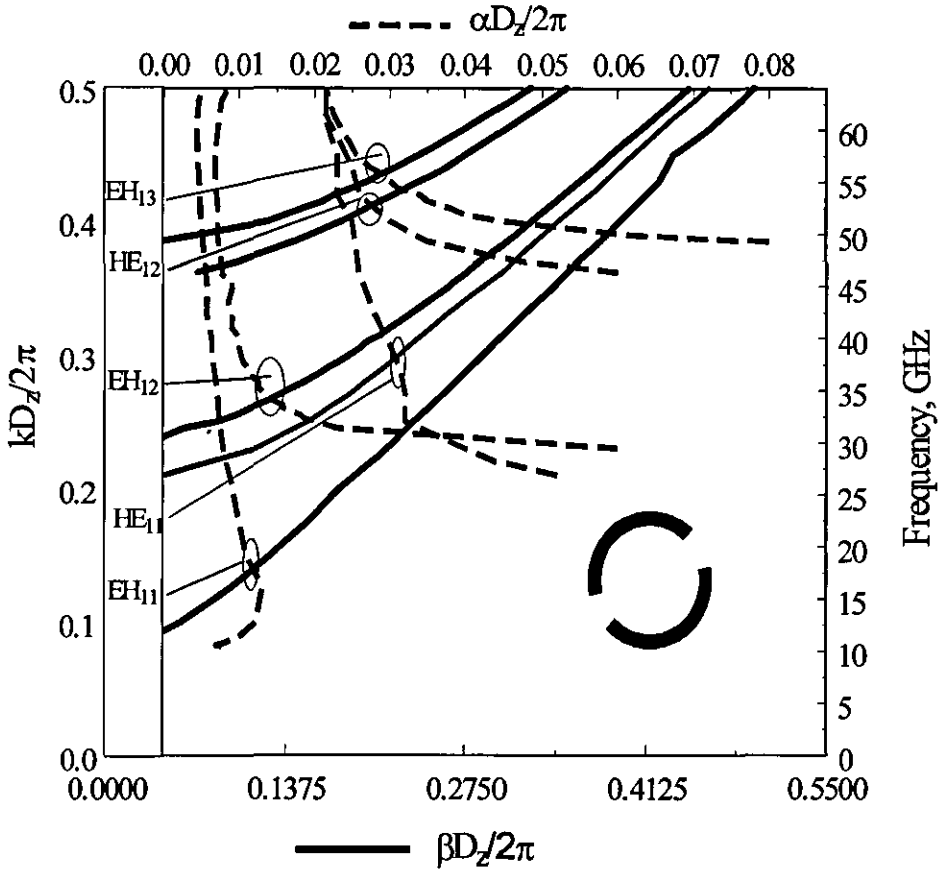


Figure 4.12:  $\beta, \alpha$  curves of the complex hybrid modes inside the FSG with two dipole



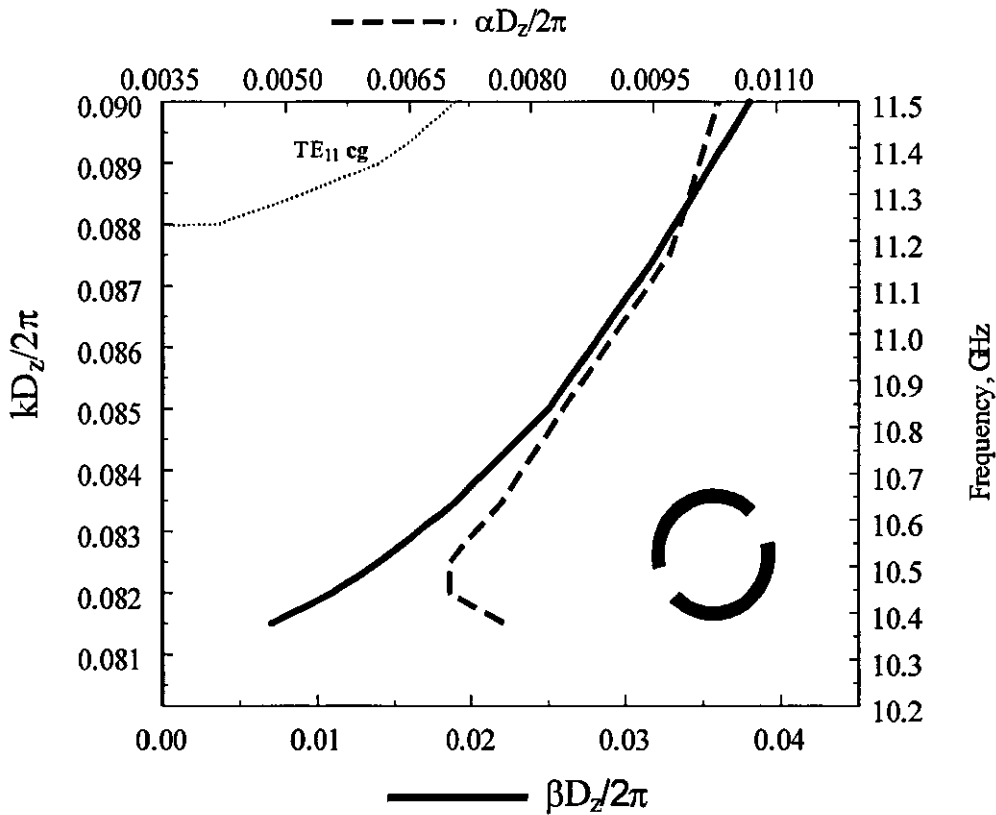
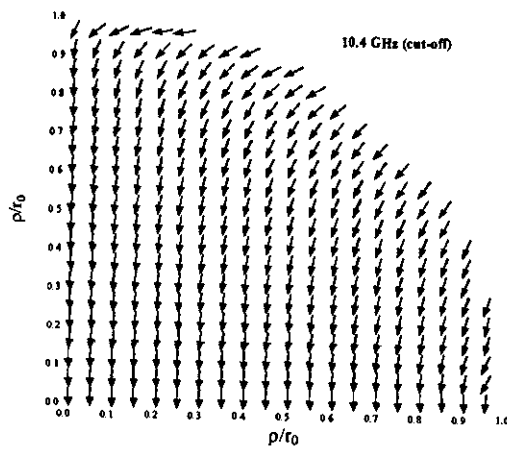


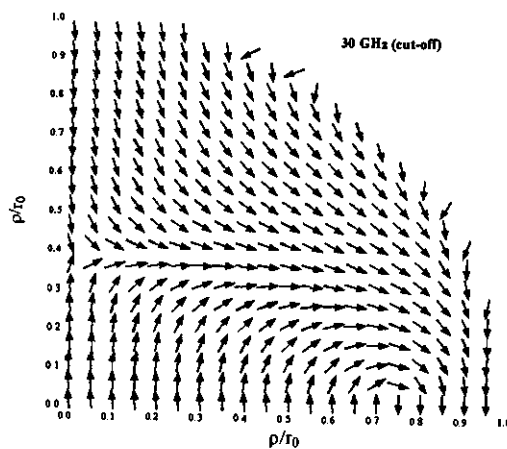
Figure 4.13: Near the cut-off region of the first leaky wave mode,  $EH_{11}$ , of the dipole arrangement of Figs 4.11 and 4.12. The dotted line is the cut-off of the  $TE_{11}$  mode in the complete guide.

The following graph, illustrates the transverse electric field lines for the first three hybrid  $H$ -type modes at cut-off frequency. Similarities with the field line patterns of  $TE_{11}$ ,  $TE_{12}$ , and  $TE_{13}$  became apparent from this graph. It should be noted that the discrepancies of the lines near the boundary for  $(\rho = r_0)$  are due to the fact that the boundary condition on the conductor is not entirely satisfied and current bases and Floquet modes need to be included in the field calculations.

$EH_{11}$



$EH_{12}$



$EH_{13}$

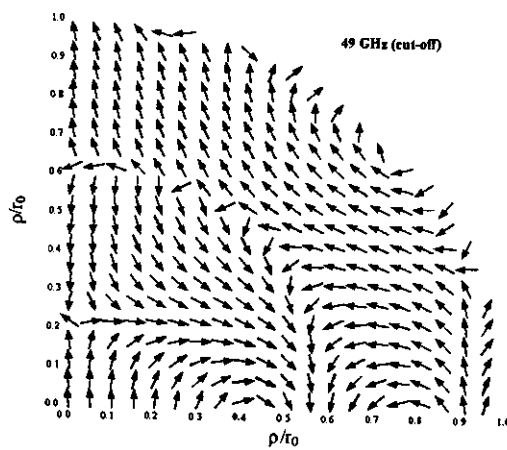


Figure 4.14: Transverse Electric field patterns for the first three hybrid  $H$ -type modes for the FSG of Fig 4.10.

In Fig. 4.12 both  $E$  and  $H$  -type hybrid modes have been shown. It is evident, that at all frequencies, the attenuation of the  $HE_{11}$  is at least 4 times greater than that of the  $EH_{11}$ . Another interpretation of the above argument is, that dipole arrays tend to transmit the polarisation orthogonal to the strips and reflect the polarisation parallel with the strips. The case is similar to the strip-grids which was discussed in Section 3.2.5. The less attenuated modes, have the main  $E$ -field component aligned along the dipole length and the main  $H$ -field component orthogonal to the dipoles.

A similar explanation can be given based on the fact that current flows mainly in the  $\phi$  direction ( $H$ -field is along  $z$ ). By increasing the element width, a substantial current will also flow in the  $z$  direction hence,  $E$ -type modes can also be guided. The latter is quantified in Fig. 4.15, which shows the predicted values for the attenuation factor of the  $EH_{11}$  and the  $HE_{11}$  modes against  $w/D_z$ . In this case, three roof -top functions were used to represent the current in the  $z$  direction. It is evident that as  $w$  increases, the attenuation of the  $HE$  modes decreases faster than that of the  $EH$  modes. The element geometry though, deviates from a dipole array, to that of an array of square patches.

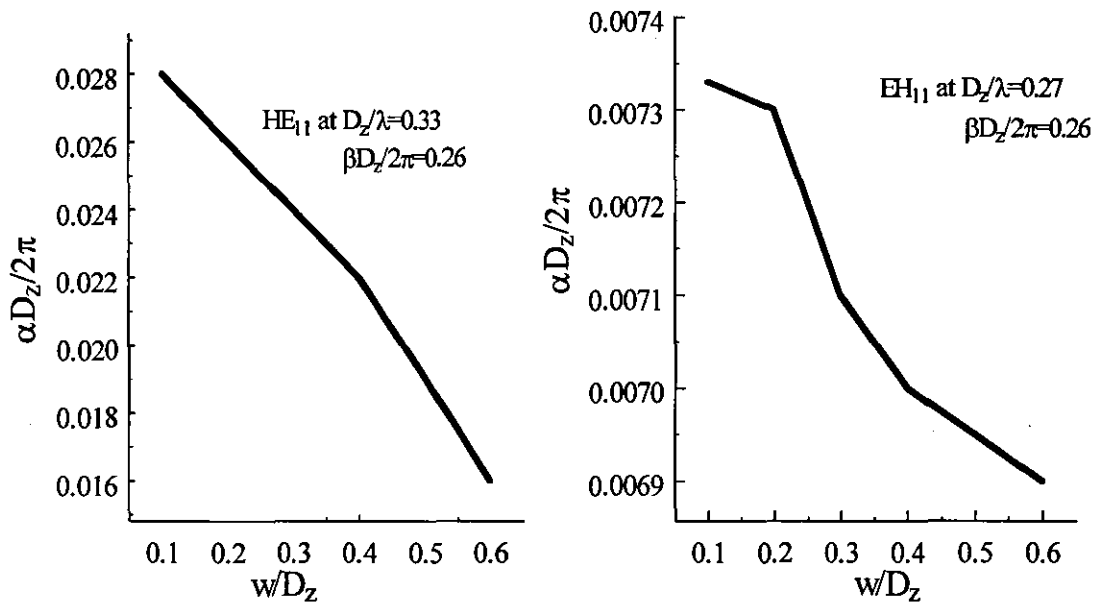


Figure 4.15: Attenuation factor  $\alpha$ , strip width for the  $HE_{11}$  and  $EH_{11}$  modes

Summarising observations on case D, one can point that all cut-off frequencies of the EH modes are below the cut-off frequencies of the TE modes of a complete guide. For the HE modes though, the cut-off frequencies are above the corresponding to the TM modes of the complete guide.

#### *CASE E*

Fig. 4.16 shows the real and imaginary parts of the propagation constant for two dipole arrays with  $D_\phi = 24.66\text{mm}$  and  $L = 23.5\text{mm}$ . The difference lies in the periodicity of the arrays along the propagation axis. The continuous line represents dispersion curves for  $D_z = 2.355\text{mm}$  and the dotted for  $D_z = 8.22\text{mm}$ . The  $\beta$ - $k$  diagrams are with respect to  $D_z = 8.22\text{mm}$ . The surface wave mode results are almost identical. For  $D_z = 2.355\text{mm}$  the  $\text{EH}_{11}$  mode has the cut-off frequency at 10.4 GHz and the resonance at 10.5 GHz. For the other periodicity, the cut-off frequency and resonance are at 8.9 GHz and 9.1 GHz respectively. The conclusion in this case is, that decreasing  $D_z$  while keeping the same length, shifts the cut-off and resonance at lower frequencies. More pronounced, is the difference in the attenuation factor which is shown in Fig. 4.16b. As,  $D_z$  decreases the attenuation falls. If  $D_z = 0$ , the attenuation approaches zero (i.e. guidance of EH modes) [6].

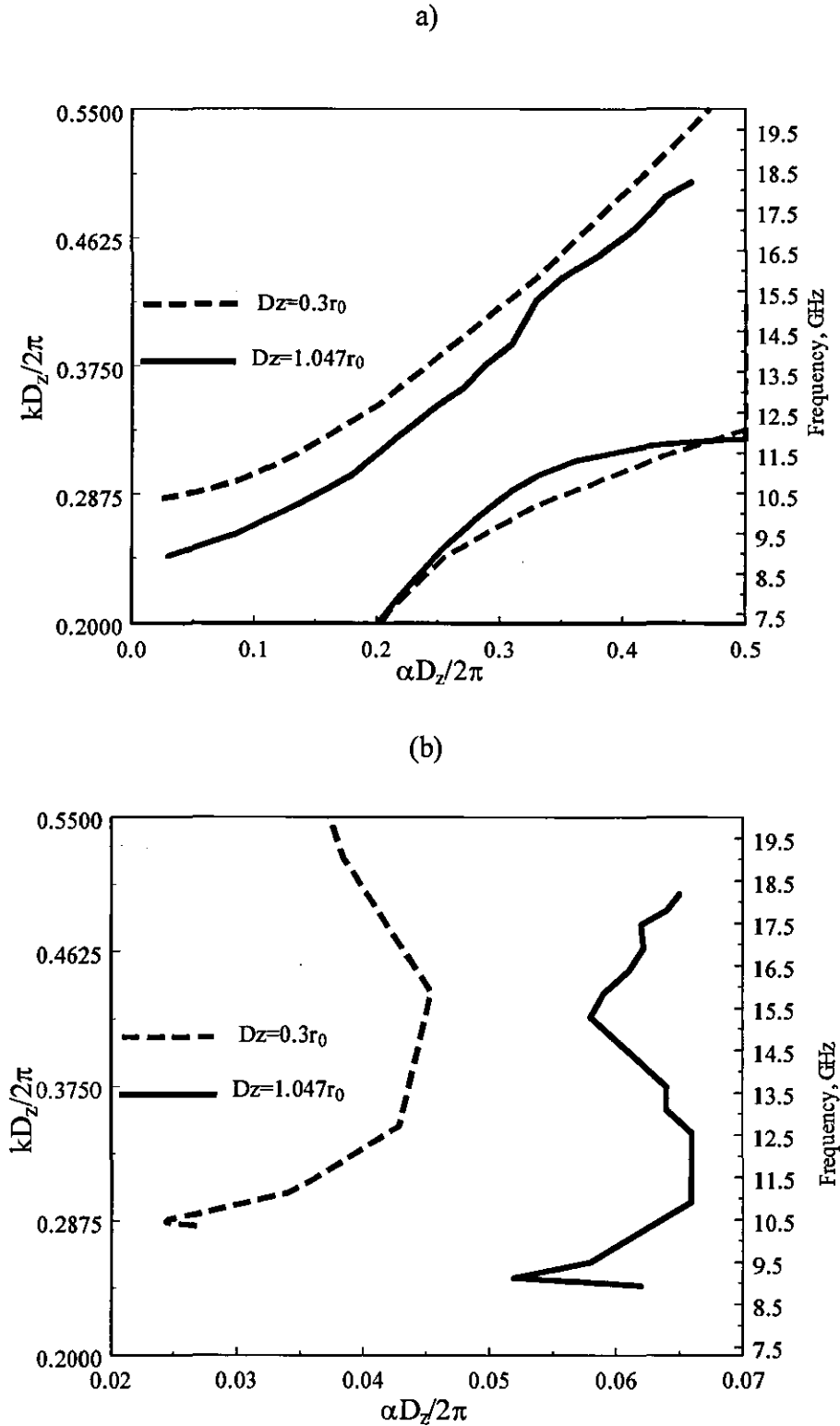


Figure 4.16: Real propagation constant (a) and imaginary part (b), for two dipole FSG with different periodicities in  $z$  ( $D_z = 1.047r_0$  and  $D_z = 0.3r_0$  when  $D_\phi = 24.66\text{mm}$  and  $D_\phi/L = 1.05$ )

### 4.3 FSG with $z$ -dipoles

The FSG with dipoles placed in the direction of propagation, is shown in Fig 4.17. The dipoles have a length  $L$  in  $z$ , narrow width  $w$  in  $\phi$  and negligible radial thickness. The radius of the waveguide is 7.85mm.

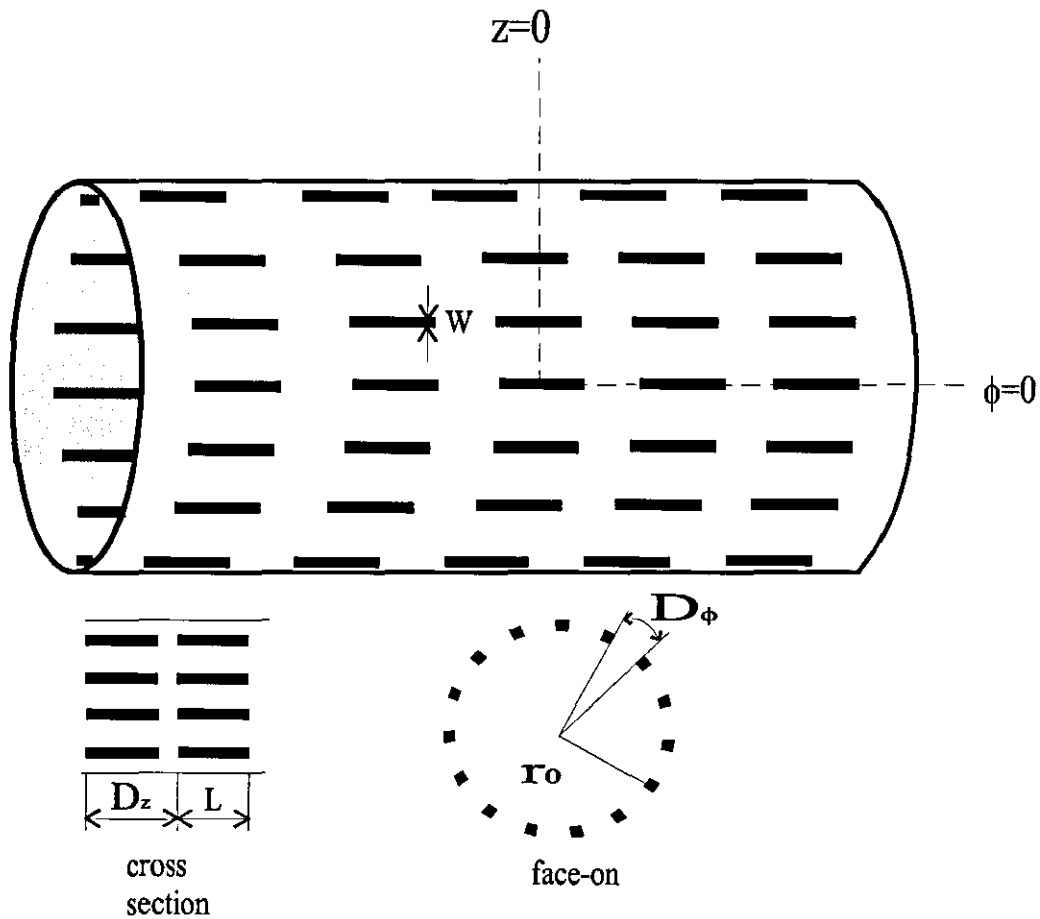


Figure 4.17: Geometry of cylindrical Frequency Selective Guide with  $z$ -directed dipoles.

### 4.3.1 *Roof-top functions and convergence ratios*

Roof top basis functions are employed to approximate the currents on the  $z$  dipole. The expansion follows directly from Section 4.2.1. In the  $z$  direction, the dipole is discretised to seven equally sized segments;  $K = 7$  and  $S = 1$ . Six  $z$ -directed roof top bases represent the current flowing along the length. The  $\varphi$ -current component, is represented by seven roof -top functions.

In all the simulations for  $z$ -dipole arrays, 13 roof-top bases and  $31 \times 31$  Floquet modes are sufficient to achieve convergence for  $\beta\text{-}ja$ .

### 4.3.2 *Numerical results for representative arrays*

In this Section predicted results for the complex propagation constant are presented for different  $z$ -dipole FSG designs. According to the number of elements in  $\varphi$ , the designs are designated case A and B. 10 elements are arranged around  $\varphi$  in case A and 20 in case B.

#### *CASE A*

Plotted in Fig. 4.18 are predicted results for the propagation and attenuation characteristics of FSG with the following parameters are:  $D_z = 8.22\text{mm}$ ,  $L/D_z = 0.952$ ,  $D_\varphi = 4.932\text{mm}$ ,  $w = 0.1 D_\varphi$ . The first solution represents the unattenuated TEM mode. The same mode was obtained for the free standing strip grating FSG, discussed in Chapter 3 (Section 3.2.3).

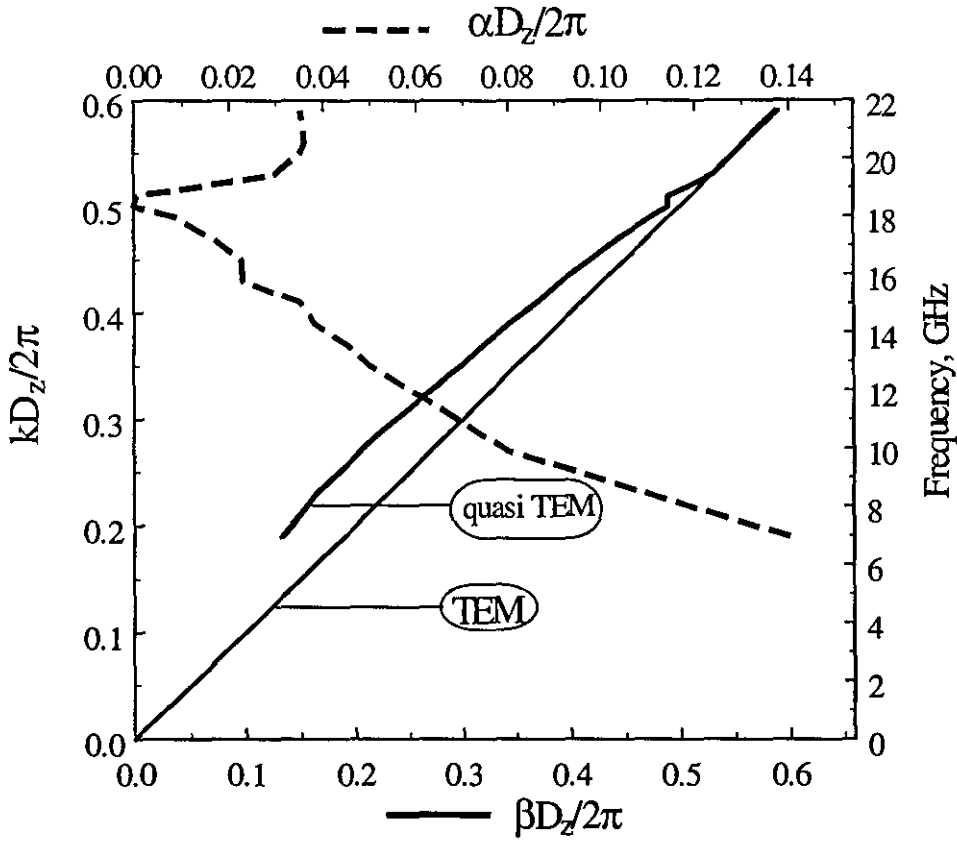


Figure 4. 18: Solution for the complex propagation constant of z-dipole FSG.

The other solution, represents a complex wave which is shown for frequencies above 7 GHz. At this frequency, the attenuation is extremely high ( $107 \text{ Np m}^{-1}$ ). Below this frequency (7 GHz), the attenuation increases, exceeding the graph limits. However, simulations at lower frequencies were performed. From the predicted data, it was evident that the mode does not possess a cut-off frequency, but emerges at a speed greater but close to the speed of light. As the frequency increases the attenuation factor decreases. However, the rate of descent is slow compared to that of fast leaky waves discussed previously (e.g. FSG in Chapter 3, and  $\phi$  dipole FSG in Section 4.2). There is no evidence of resonant behaviour for this mode until  $\beta D_z / 2\pi = 0.5$  ( $D_z / \lambda = 0.505$ ), where the attenuation goes to zero. A sudden zero or minimum in the attenuation appears to be the general



periodic structures when  $\beta$  approaches  $k$  and  $D_z / \lambda \cong 0.5$  [7]. This mode is referred in this thesis as quasi (complex) TEM. In a separate diagram, Fig 4.19, the complex propagation constant for the first fast wave mode is shown. The curves correspond to two different dipole lengths: 7.825mm and 7.07mm. For the longer dipole the cut-off frequency of the  $HE_{11}$  mode is at 22 GHz and the resonance is at 23 GHz. For the other dipole, the cut-off of the mode is at 22.5 GHz and the resonance at 23.2 GHz. Both  $HE_{11}$  curves appear below the  $TM_{11}$  line of the complete guide. Plotting the transverse electric field lines for the  $HE_{11}$  mode at cut-off, reveals the TM properties of the hybrid mode.

$H$ -type modes are highly attenuated and therefore, not plotted. The case is similar to the  $z$ -strip FSG discussed in Chapter 3 (Section 3.2.5).

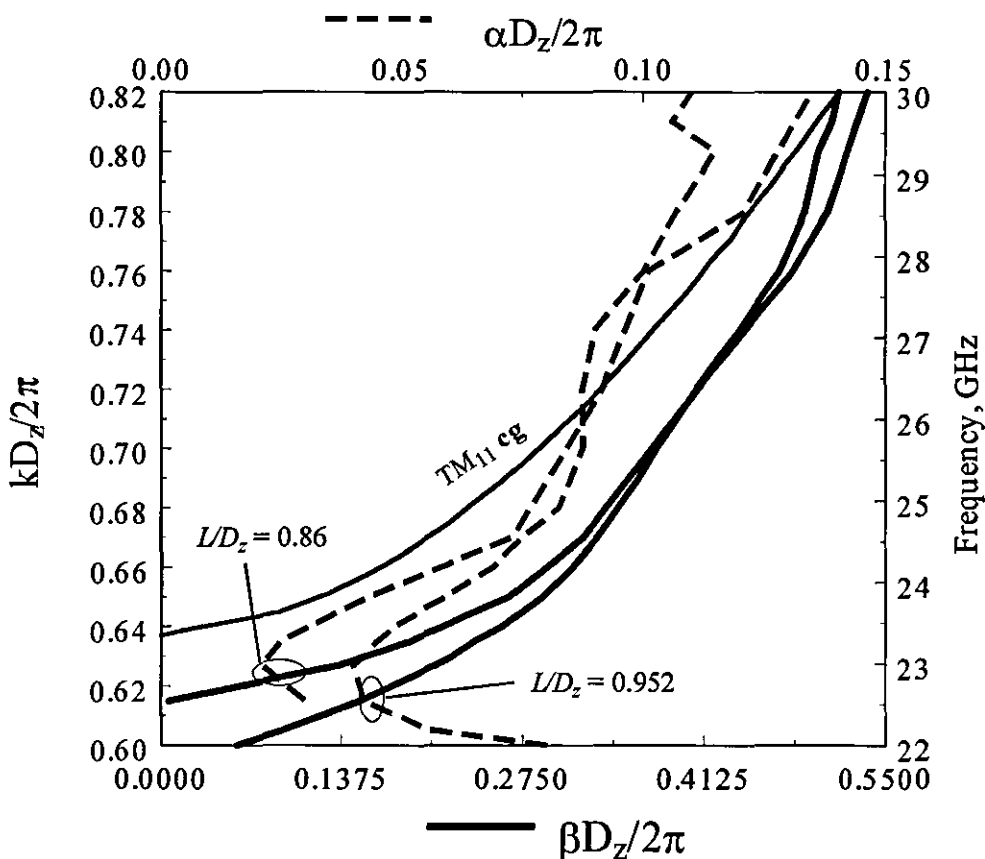


Figure 4. 19: The first hybrid  $HE_{11}$  leaky wave mode for a  $z$ -dipole arrangement. The periodicity in the  $\theta$  and  $\phi$  direction is 8.22mm and 4.932mm. Results are shown for two different dipole lengths.

## CASE B

The number of elements around  $\varphi$  is increased by a factor of 2. The parameters are:  $D_z = 8.22\text{mm}$ ,  $L/D_z = 0.912$ ,  $L = 7.5\text{ mm}$ ,  $D_\varphi = 2.465\text{mm}$ ,  $w = 0.2 D_\varphi$ . Fig. 4.20 shows the propagation and attenuation constant for the first hybrid  $\text{HE}_{11}$  mode. The mode has a cut-off at 23.5 GHz and it crosses the  $\text{TM}_{11}$  line at 24.75 GHz. At this frequency the attenuation factor has almost a zero value ( $\alpha = 0.23\text{ Np/m}$ ). The transverse electric field lines of the mode, are shown in Fig. 4. 21. The mode holds strong TM properties at cut-off. Another resonance is found at 28.1 GHz, where the curve of real  $\beta$  crosses the  $\text{TM}_{11}$  line for the second time. The attenuation factor however, is relatively high at this point.

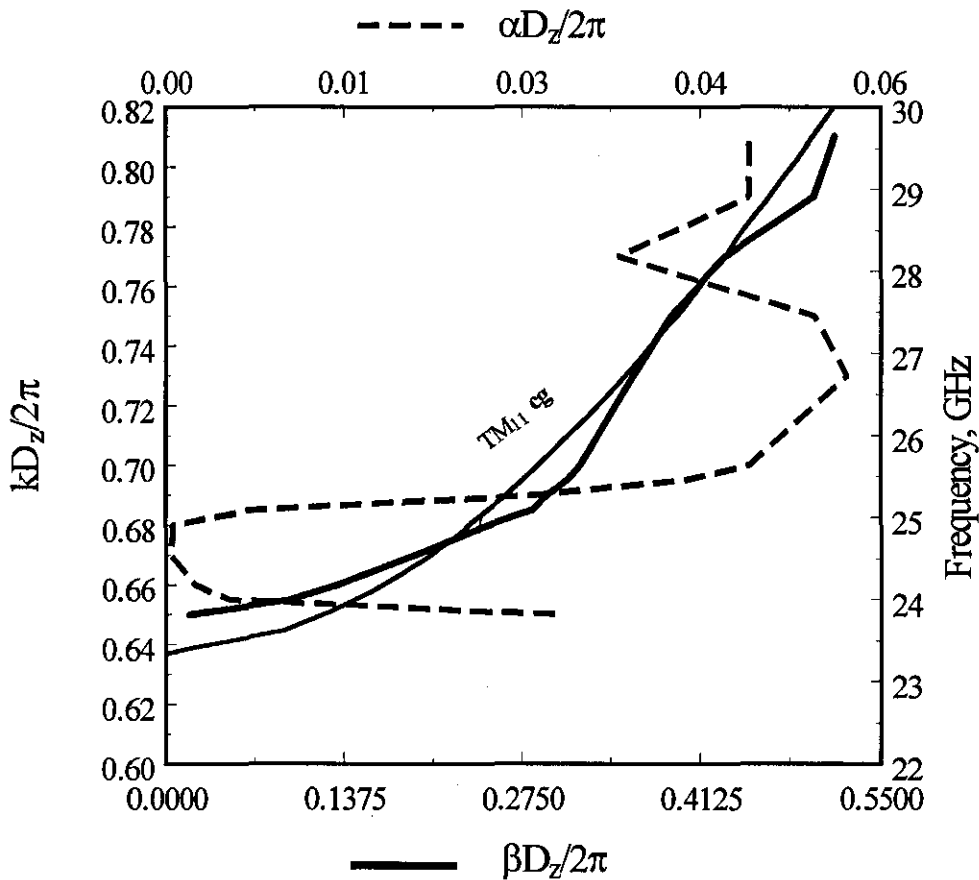


Figure 4. 20:  $\text{HE}_{11}$  mode for  $D_z=8.22\text{mm}$  and  $D_\varphi=2.45\text{mm}$ . The length is 7.5mm and the width is  $0.2D_z$ .

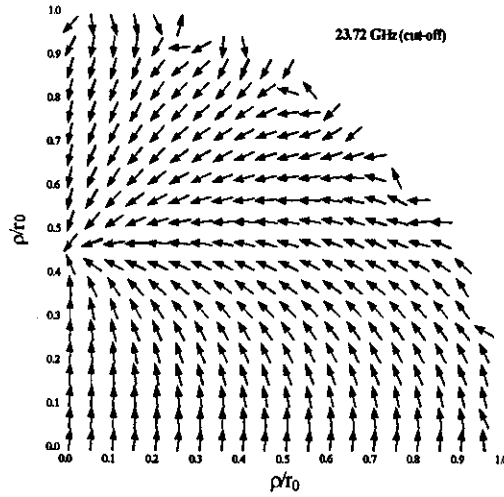


Figure 4. 21: Transverse electric field lines of  $HE_{11}$  mode of case B at cut-off.

Comparing results from cases A and B, it is evident, that the attenuation for the propagating modes is reduced when the periodicity in  $\varphi$  is reduced.

### 4.3.3 The grating lobes

Since the Bragg frequency  $\frac{D_z}{\lambda} = 0.5$  is exceeded, the -1 space harmonic may become fast and contribute to the radiating fields (see also Appentix B). The complex propagation constant for the -1 harmonic can be found according to the

$$\text{Floquet relation: } k_{z-1} = \beta - ja - \frac{2\pi}{D_z}.$$

Fig. 4.22, shows the Brillouin,  $\beta$ - $k$ , curves for the basic (0 order) harmonic and the -1 harmonic, for the z-dipole FSG of case B. The  $\beta_{-1}$  curve is identical with that of  $\beta$  and simply shifted in the direction of the  $\frac{\beta D_z}{2\pi}$ -axes by -1. It is evident that

immediately after resonance, the curve of  $\beta_{-1}$  crosses the line of  $-k$  and becomes fast ( $|\beta_{-1}/k| < 1$ ). As a result, another radiating beam will emerge which belongs to the -1 harmonic. The beam radiates in the backward quadrant as long as  $\beta_{-1} < 0$  (radiation angle between  $-90^\circ$  and  $0^\circ$ ). The angle of the grating lobe is given by  $\theta_{-1} = \sin^{-1} \frac{\beta_{-1}}{k}$ .

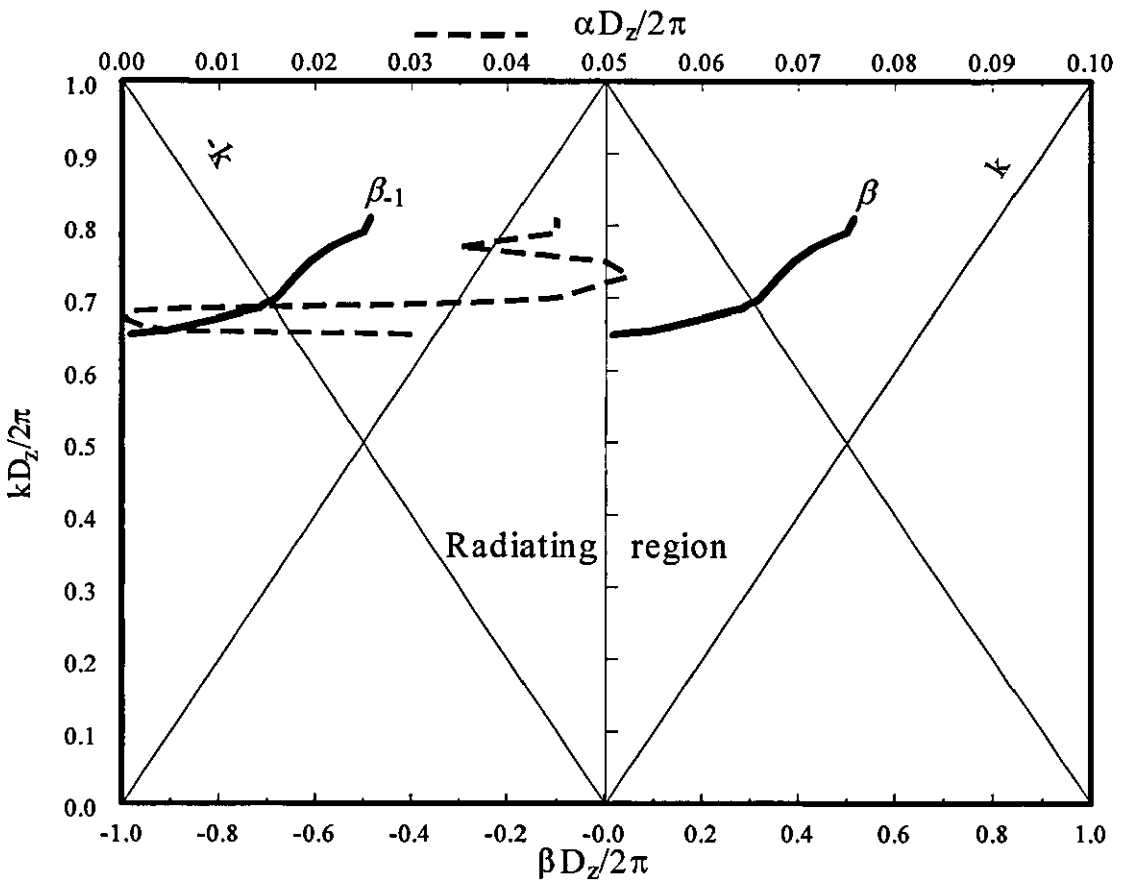


Figure 4. 22:  $\beta$ - $k$  diagrams for the basic and the -1 leaky harmonics, for the FSG with  $z$ -dipoles ( $D_z = 8.22\text{mm}$  and  $D_\phi = 2.45\text{mm}$ ,  $L = 7.5\text{mm}$   $w = 0.2D_z$ ).

#### 4.4 Closing remarks

This Chapter has dealt with open FSGs with dipole arrays. Using the two dimensional analysis of Chapter 2, the current on the dipole is expanded in two dimensional basis functions. Predicted results for the complex propagation constant are given for representative geometries. Their stability is verified with the aid of convergence tests. Several effects are addressed including, lattice geometry, leakage properties and element resonance. The latter can be considered as the most important feature of the dipole geometries.

Summarising the propagation behaviour of transverse dipoles, there are two types of modes that can be excited: unattenuated surface waves and fast leaky wave modes. The surface wave is the dominant mode at low frequencies and is excited by the discontinuity of the interface due to the dipoles. A stop band appears for the surface wave when the Bragg condition is met. Fast waves appear before the surface wave stop band. These modes are hybrid and radiate energy in free space (leaky). The singular polarisation behaviour of the  $\phi$ -dipoles means that only the  $H$ -type modes are properly excited. These modes resemble TE modes. It was pointed that the other set of modes (TM like), can also propagate by increasing the dipole width. The similarities with the designs of FSG with rings of Chapter 3 are obvious.

The leakage constant is frequency depended. The elements resonate at frequencies which are close to  $L/2$ , near which the attenuation drops and more energy is guided within the FSG. The cut-off frequency (and the resonance frequency) of the  $\text{EH}_{11}$  mode, can be lowered by increasing the dipole length. The advantage is that the FSG maintains its size (alternative ways to lower the cut-off of a mode would be to increase the FSG radius). By decreasing the separating distance in  $z$ , the attenuation can be lowered. Finally, other resonant frequencies are found in wavelengths multiple of  $L/4$ . In those resonances however, the attenuation constant is not significantly reduced.

In the case of  $z$ -directed dipole FSGs, the basis functions are expressed similarly to the  $\phi$  dipoles, by exchanging the role of  $\phi$  and  $z$ . There are three solutions to the characteristic equation. The TEM and the  $\text{HE}_{11}$  are in agreement with the solutions

of the FSG with longitudinal strips of Chapter 3 (Section 3.3). However, there is a frequency where the element resonates and the attenuation decreases. The resonant frequency depends on the length of the dipole and the periodicity in  $\varphi$ . When more elements are included around  $\varphi$ , both the resonance and the cut-off frequencies of the  $HE_{11}$  mode are shifted at higher frequencies. For a design with 20 elements in  $\varphi$ , the attenuation drops to zero at resonance and the  $HE_{11}$  mode is guided. Immediately after resonance, the -1 harmonic becomes fast and contributes to the leakage. The condition for the presence of grating lobes, is the periodicity to be half the wavelength. The other solution represents a complex quasi TEM. The attenuation constant for this mode goes to zero near the Bragg condition, when  $\beta$  approaches  $k$ .

*References*

- [1] LOCKYER, D., MOORE, C., SEAGER, R. D., SIMPKIN, R. and VARDAXOGLU, J. C.: 'Couple dipole arrays as reconfigurable Frequency Selective Surfaces', *Electron. Lett.*, Vol. 30, 1994, pp. 1258-1259.
- [2] VARDAXOGLU, J. C.: 'Frequency Selective Surfaces-analysis and design', 1997 Research Studies Press, Taunton, UK.
- [3] MITTRA, R. and JONES, K. E.: 'Theoretical Brillouin ( $k$ - $\beta$ ) diagrams for monopole and dipole arrays and their application to log-periodic antennas', *IEEE Trans. On Antennas Propagat.*, Vol. AP-12, Sept. 1964, pp.533-539.
- [4] POTHARAZU, P. K., and JACKSON, D. R.: 'Analysis and design of a leaky-wave EMC dipole array', *IEEE Trans. On Antennas Propagat.*, Vol 40, No. 8, Aug. 1992, pp.950-958.
- [5] HERPER, J. C., HESSEL, A., and TOMASIC, B.: 'Element pattern of axial dipole in a cylindrical phased array, Part I: Theory', *IEEE Trans. On Antennas Propagat.*, Vol. Ap.-33, No. 3, March. 1985, pp.259-272.
- [6] KISHK, A. A and KILDAL, P.: 'Asymptotic boundary conditions for strip-loaded scatterers applied to circular dielectric cylinders under oblique incidence', *IEEE Trans. On Antennas Propagat.*, Vol. 45, No. 1, Jan. 1997, pp.51-56.
- [7] JACOBSEN, J.: 'Analytical, numerical, and experimental investigation of guided waves on a periodically strip-loaded dielectric slab', *IEEE Trans. On Antennas Propagat.*, Vol. AP-18, No. 3, May 1970, pp. 379-388.

# CHAPTER 5

## Cylindrical FSG with square-loop elements

### *5.1 Introduction*

In this Chapter, the investigation of FSG with square loop elements is presented. The geometry can result from the combination of the  $\varphi$  and  $z$  dipole arrays presented in Chapter 4. It has been shown, that the operating hybrid modes inside the dipole FSG, are associated with the dipole's resonance and polarisation behaviour. With the square loops, the electric field can be polarised in both directions. The FSG geometry is discussed in Section 5.2. Section 5.3 deals with the roof-top functions expansion, in order to express the current on a square loop. With the view to minimise computational effort, a technique is introduced and



discussed for the roof-top bases. In Section 5.4 predicted results are shown, for the complex propagation constant of representative arrays. A variety of square loop arrays is chosen (cases A, B, C), in order to explain the effect of the size of the elements and the periodicity, on the propagation behaviour. The complex propagation constant is utilised to obtain the currents and fields and plot the mode patterns. In Section 5.4.1, the performance of the model is examined by checking the boundary condition for the tangential  $E$ -fields. The hybrid factor, which is a prime factor in designing balanced antenna feeds, is calculated and discussed in Section 5.4.2. In Section 5.4.3, the predicted dispersion curves are shown and discussed in comparison with the dipoles' FSG. In Section 5.4.4, results for representative square loop arrays with different periodicities are shown. In Section 5.4.5, the performance and accuracy of the model are tested by measurements, for a particular design. The last Section, 5.5, is concerned with closing statements and suggestions for the applications of the square loop array.

## 5.2 Square-loop geometry

Fig. 5.1 shows a cylindrical FSG with square-loop elements. The radius of the waveguide is 7.85mm. The structure is unbounded in the  $z$  direction and has a natural periodicity of  $2\pi$ . The element consists of four equally sized arms, each of length  $L$ .  $D_\phi$  and  $D_z$  are equal and define the dimensions of the unit cell. The general theoretical analysis described in Chapter 2, is applied here, in order to model the FSG, with some modifications in the roof-top function expansion method.

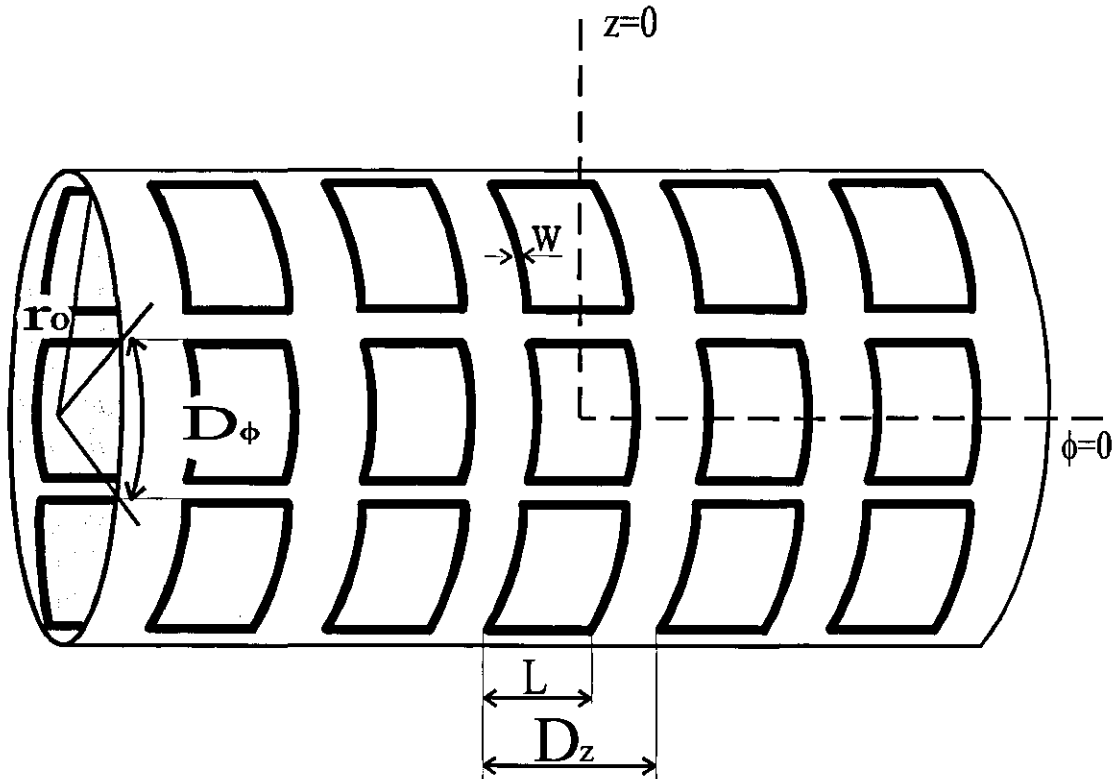


Figure 5.1: Geometry of cylindrical Frequency Selective Guide with square loop elements.

### 5.3 Current functions on the square-loop

The current on the element is approximated in a subsectional manner, as discussed in Chapter 2, (Section 2.5.2), for a conducting element. The bases on the square loop are shown graphically in Fig. 5.2. Each current component is expanded as a set of 30 roof-top functions. The representation has been suggested by Rubin et. al. [1], for a MoM analysis of the scattering from infinite periodic arrays. With 30 bases for each current, the dimension of the impedance matrix is  $60 \times 60$ . The latter are prohibitively large, in a sense that the iterative procedure becomes impractical, due to excessive computational requirements. Additionally, there are restrictions in the size of the element since, the width of each arm has to be  $2/7$  of its length (as is the case of Fig. 5.2 with seven bases in each arm). To simulate elements with smaller

widths, or perform convergence tests, the number of roof-top functions should be increased; resulting to a further increase in computational demands. As an example, with 9 segments on each arm, the total number of roof-top functions is 84. For 84 bases and 961 Floquet modes 70min of CPU time was needed, to obtain a point on the dispersion curve.

The above adversities can be reduced by using the roof-top functions illustrated in Fig. 5.3. Each arm is divided into seven equal segments. Six roof-top functions represent the current flowing along the length. These are centred at  $z = \pm(K-1)\Delta z/2$ ,  $\varphi = (S+0.5)\Delta\varphi/2$ , for the  $\varphi$  directed arm or, at  $\varphi = \pm(S-1)\Delta\varphi/2$ ,  $z = (k+0.5)\Delta z/2$  for the  $z$  arm. In the roof-top basis functions which represent the current terms across the width, the triangular function is defined in one increment  $\Delta z(\Delta\varphi)$  (as opposed to  $2\Delta z(\Delta\varphi)$ ). These functions are centred at points  $z = \pm(k-1)\Delta z/2$ ,  $\varphi = S\Delta\varphi/2$  and  $\varphi = \pm(S-1)\Delta\varphi/2$ ,  $z = k\Delta z/2$ . In total, there are 22 roof-top bases for each current component and the dimension of the impedance matrix is  $44 \times 44$ .

Two factors which can be considered as limitations of the above expansion are: a) the discontinuity embedded by the different size roof-top functions at the arm junction (area A, in Fig. 5.3) and b), the width to be 1/7 of the arm. When trying to perform a convergence test with more currents, the physical size changes as the width of the element changes. For example, if  $K = S = 9$  and  $K = S = 7$ , the difference in the area covered by the bases is 10%.

The only convergence tests performed for square loop arrays were for the number of Floquet modes. For the number of currents, convergence tests were impractical to apply. As explained earlier in this Section, finer segmentation of the square loop arm, results to a large impedance matrix and changes the size of the element. In all simulations for square loop arrays, convergence was ensured when 961 Floquet modes were used (31 modes per Floquet number). When the number of Floquet terms increased to  $61 \times 61$ , the difference in the results was found to be insignificant. With 961 Floquet terms, approximately 3 minutes of CPU time in the VPX machine is needed to obtain a point on the dispersion curve.

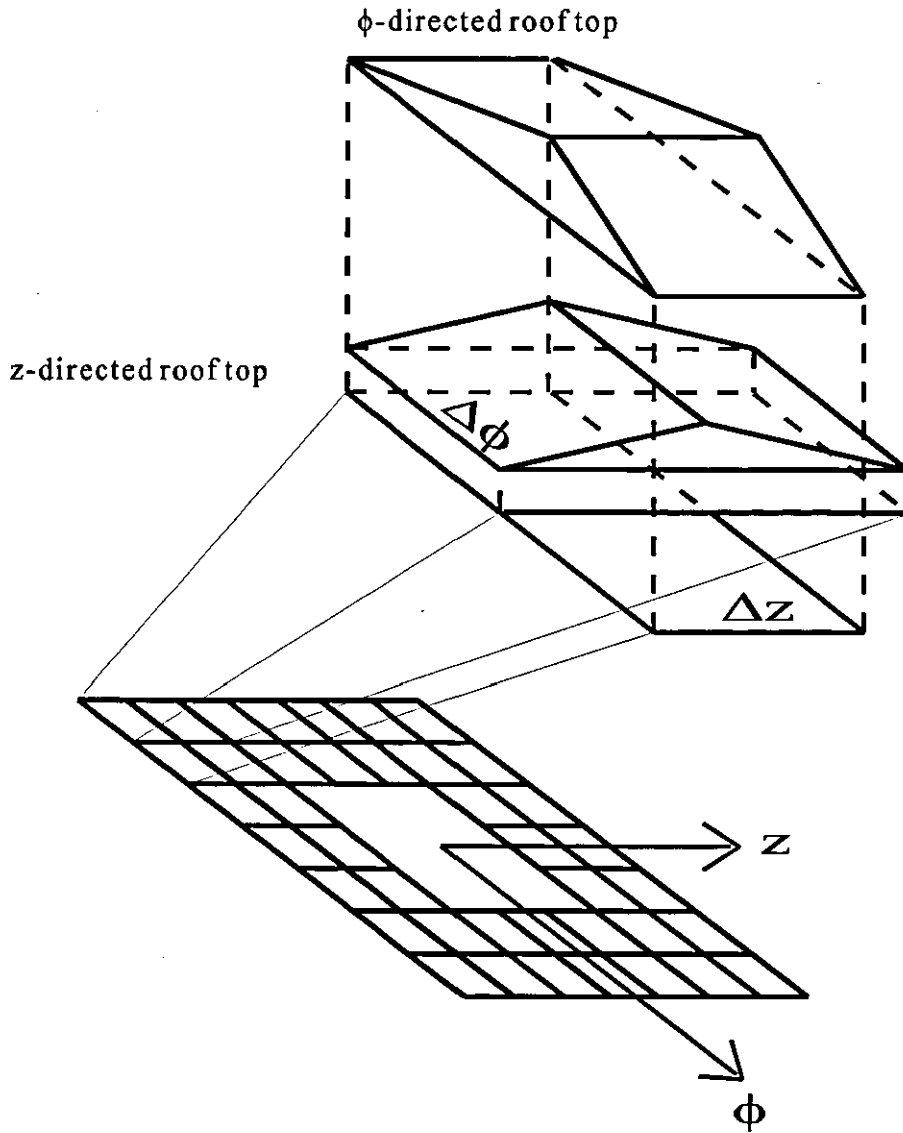


Figure 5.2: Roof-top functions representing the current on the square loop.

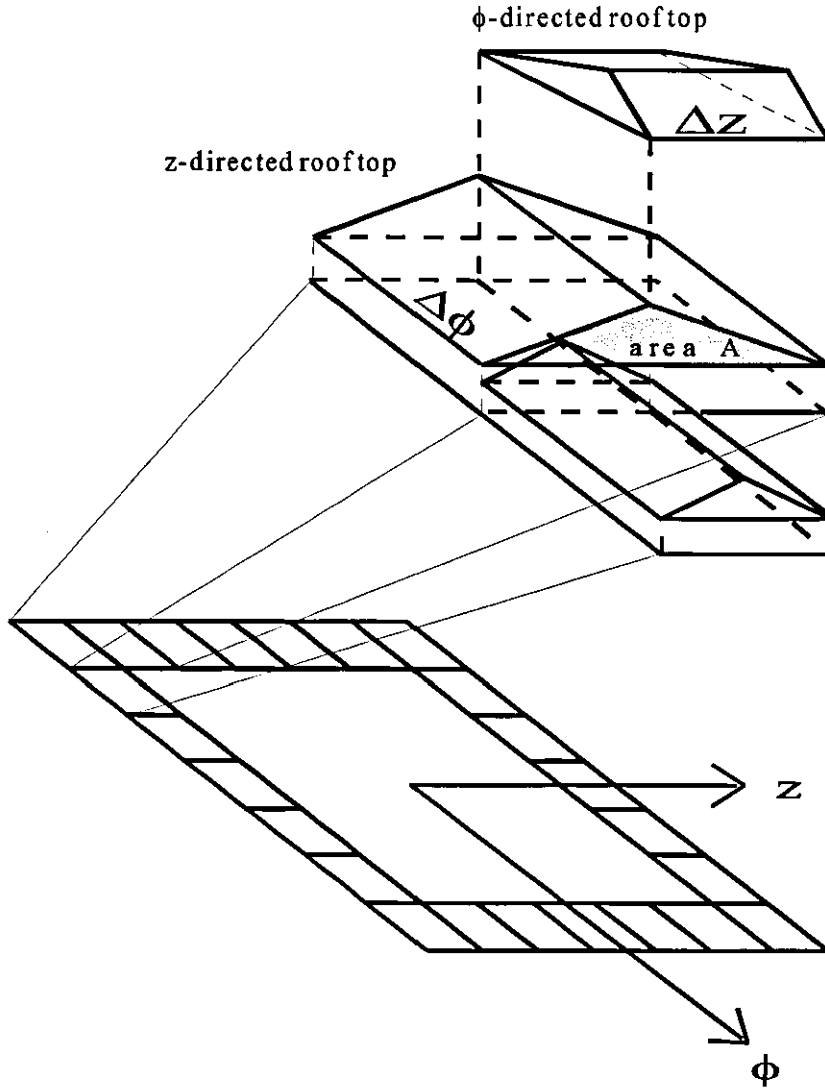


Figure 5.3: Roof-top functions approximate representation for the current on the square loop. The bases have different size.

#### 5.4 Numerical results for representative arrays

##### CASE A

Fig. 5.4 shows the dispersion characteristics for the lowest order hybrid modes of an FSG with square loops. There are 10 elements fitted around the circumference of the guide. Each arm of the square loop is 95% of the periodicity;  $D_\phi = D_z = 0.62831$   $r_0 = 4.932\text{mm}$  and  $L=4.68\text{mm}$ . The width  $w$  is  $0.668\text{mm}$ . At low frequencies, the dominant mode is a surface wave excited by the discontinuity at the interface due to the square loop array. Similarities to the surface waves excited for the FSG with rings or transverse dipoles (numerical examples in Chapter 3 and Chapter 4 respectively), are obvious. The surface wave starts at 0 frequency and becomes loosely bound, as it approaches a higher cut-off condition; due to mode coupling effect. The coupling occurs at 19.2 GHz, when the -1 backward travelling harmonic propagates with the same rate as the dominant forward 0 harmonic i.e.  $-k_{z-1} = k_{z0}$  (see also Appendix B). The first fast wave mode has a cut-off at 13.75 GHz. It is a complex wave ( $\text{EH}_{11}$ ) and the plotting of the transverse electric field lines at cut-off, reveals strong TE characteristics. At cut-off, the leakage constant for the mode, is high and decreases rapidly as frequency increases. It reaches the lowest value (zero) at 20.1 GHz, the frequency which is identified as the resonance. At resonance the wave sees the structure as a complete reflective wall and its energy is guided within the waveguide. This is justified since  $\beta$  has the value for the  $\beta$  of the  $\text{TE}_{11}$  of a closed cylinder ( $\text{TE}_{11}$  and  $\text{EH}_{11}$  curves are crossed). The relation between element arm length and wavelength at resonance is:  $L = 0.315 \lambda_r$ . After resonance, the attenuation constant increases with frequency and the FSG switches back to a leaky wave antenna. The next mode is the hybrid  $\text{HE}_{11}$  mode which starts propagating at 23 GHz. For this mode, the attenuation constant holds relatively large values even at resonance. The latter occurs at 24 GHz. In the same graph, the  $\text{TM}_{11}$  curve is also shown for the complete guide. The cut-off of the  $\text{HE}_{11}$  mode, is below to that of the  $\text{TM}_{11}$  for a complete cylinder, and the curves never meet.

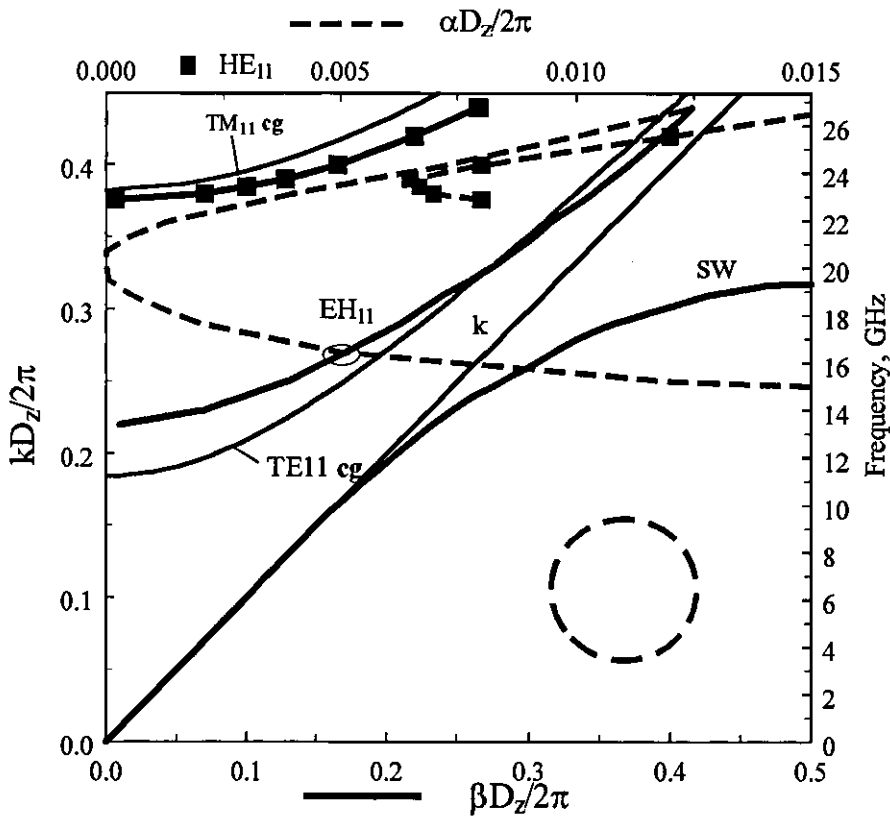


Figure 5.4: Propagation and attenuation plots for an FSG with 10 square loops along  $\varphi$ . ( $D_\varphi = D_z = 4.932\text{mm}$ ,  $L = D_z / 1.05$ ,  $r_0 = 7.85\text{mm}$ ,  $w = L/7$ ).

Fig. 5.5 illustrates the attenuation in  $\text{dBm}^{-1}$  for the first hybrid mode, the  $\text{EH}_{11}$ , as a function of frequency. Between 19.5 GHz and 20.7 GHz, the attenuation drops to zero as a result of the resonance. The guidance bandwidth is

$$BW = \frac{\Delta f}{f_c} = \frac{1.2}{20.1} \approx 6\%$$

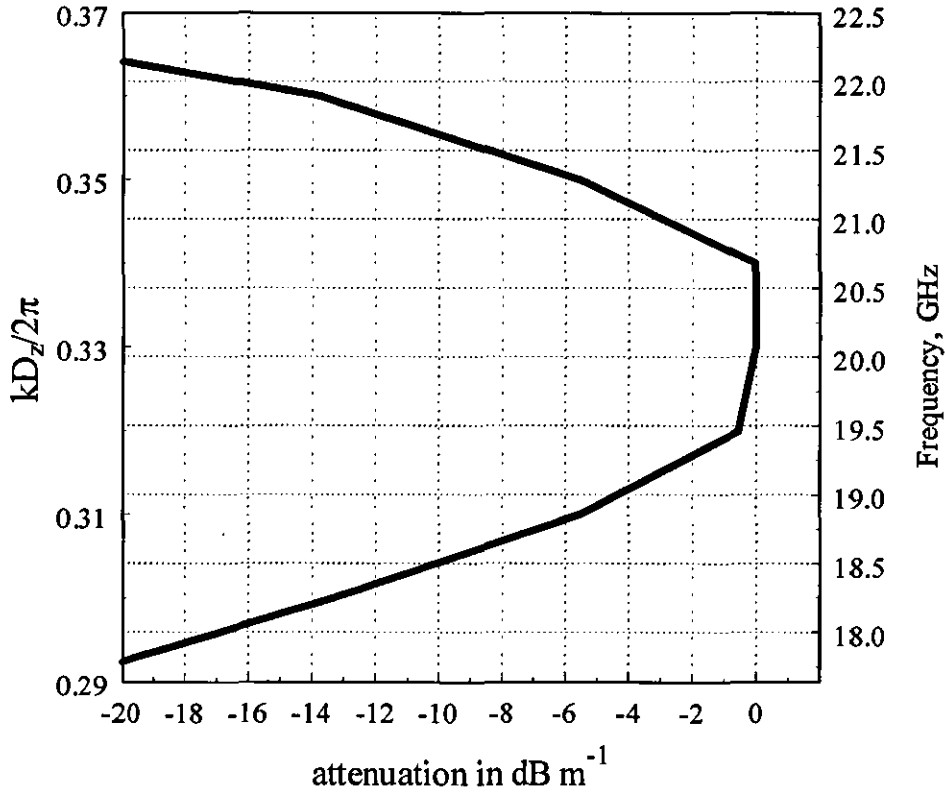


Figure 5.5: Expanded version of the attenuation for the  $EH_{11}$  mode of case A.

### CASE B

Fig. 5.6 shows the dispersion curves, of FSG with different sized elements to that of case A. The periodicity is kept at 4.932mm, but the length of the square loop arm is reduced to 83.3% of the periodicity. The width of the square loop is 0.587mm. To depict the resonance, only a part of the dispersion curve for the  $EH_{11}$  mode is plotted. The FSS wall resonates at 24 GHz and the  $EH_{11}$  mode is strongly guided within the FSG. The ratio square loop arm length to wavelength of resonance is,  $L = 0.328 \lambda_r$ , which is about the same as for that of case A.



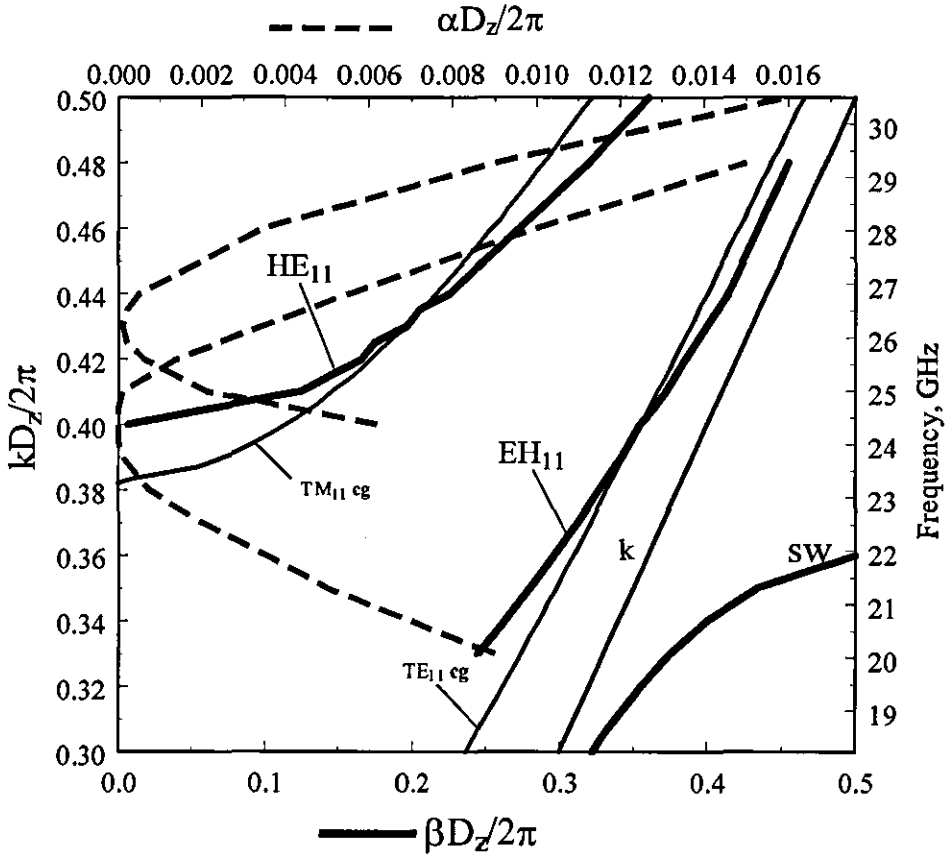


Figure 5.6: Complex propagation plots for FSG with elements of different length than that of case A ( $D_\phi = D_z = 4.932\text{mm}$ ,  $L = 4.11\text{mm}$ ,  $r_0 = 7.85\text{mm}$ ,  $w = 0.58\text{mm}$ ).

The other fast wave is the  $HE_{11}$  hybrid mode. The resonance for this mode is found at 26 GHz; the frequency the attenuation goes to a minimum. At the same frequency, the  $\beta$  curve of the  $HE_{11}$  mode, crosses the  $TM_{11}$  line of the complete cylinder. Also at the same frequency, the  $EH_{11}$  mode has become leaky, i.e. the FSG is guiding one mode while radiating another (multimode operation).

The surface wave mode starts at 0 frequency and becomes loosely bound at 18 GHz. At approximately 21 GHz, the surface wave reaches the higher cut-off.

The complex propagation constant is known and the fields inside a cross section of the FSG can be calculated by the method described in Chapter 2 (Section 2.8). The simulation is run with 22 roof-top functions for each current, and 961 Floquet harmonics. Fig. 5.7 illustrates the plotted transverse electric field lines for the hybrid  $\text{EH}_{11}$  mode at three different frequencies near resonance. Below the resonant frequency the hybrid mode is leaky and exhibits strong TE properties ( $H$ -type). At resonance, the  $E_z$  component almost vanishes and the mode becomes pure TE. It is notable, that in the plots above cut-off, the electric field lines are less curved than the lines of the  $\text{TE}_{11}$ ; almost linearly polarised in a Cartesian  $x$ -axis. There are discrepancies of the lines near the boundary at  $\rho = r_0$ . The discrepancies appear because the condition for the tangential electric field to vanish over the conductor is not entirely satisfied. In the next Section a boundary condition checking is performed.

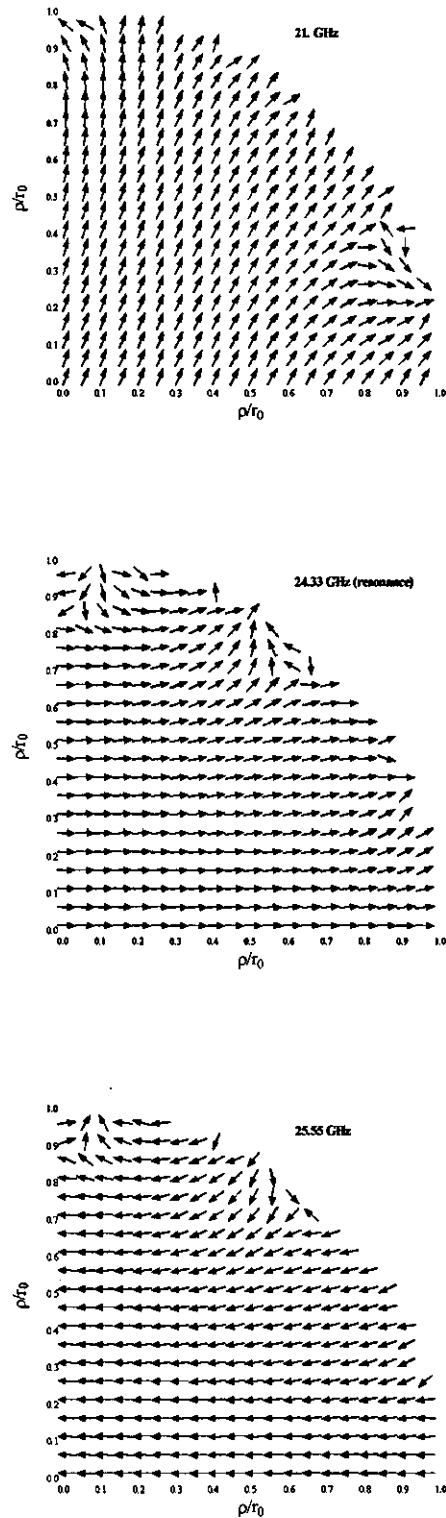


Figure 5.7: Transverse electric field line patterns of  $\text{EH}_{11}$  mode at various frequencies near cut-off for the FSG of case B.

### 5.4.1 *Boundary condition checking*

The boundary condition that enforces the total electric field to be zero over the conductor, must be satisfied for all cases and all solutions of  $\beta\text{-}ja$ , to ensure the validity of the predictions. In Fig. 5.8, the dominant transverse  $E$ -field component of the  $\text{EH}_{11}$  mode for case B, at cut-off, is shown. The fields are calculated for all  $\varphi$  between 0 and  $2\pi$  and  $z = -L/2$ . 22 bases are used for each current and 961 Floquet harmonics. The unit cell centred at the origin, extends from  $-18^\circ$  to  $18^\circ$  and the  $\varphi$  directed arm of the element, extends from  $-15^\circ$  to  $15^\circ$ . The main component of the electric field is the azimuthal, since the polarisation is TE. This component is plotted for one period. It is evident, that the component has the lowest values over the conductor but is not zero especially, near the edges. Following observations discussed in Chapter 3 (Section 3.2.6), the present amount of current functions and Floquet modes is adequate to guarantee convergence of the solutions for the complex propagation constant. However, these are not enough to entirely satisfy the boundary condition. The problem may be addressed in the same way, as in the one dimensional case, by increasing the number of roof-top functions, i.e. finer discretization of the conducting area. Then, the number of Floquet modes must be increased until convergence is ensured. The penalty to pay when performing such tests, is added computational time. In the case of the square loop array, these requirements become excessive and therefore, not performed.

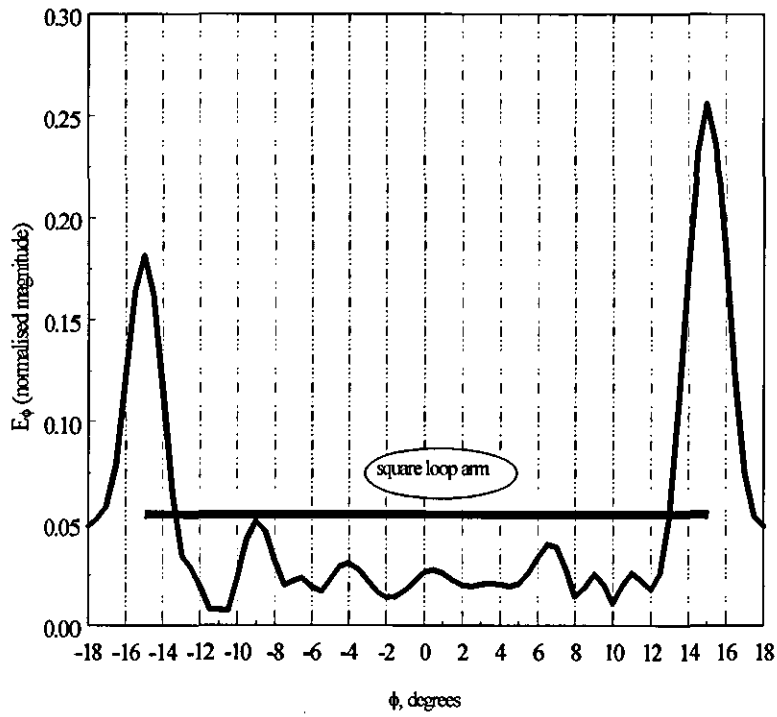


Figure 5.8: Field amplitude for the  $\phi$ -electric field component computed at the boundary for  $z = -L/2$  and  $\phi = -D_\phi/2$  to  $D_\phi/2$ . ( $D_\phi = D_z = 4.932\text{mm}$ ,  $L = D_z/1.2$ ,  $r_0 = 7.85\text{mm}$ ,  $w = L/7$ ,  $D_z/\lambda = 0.4$ ).

### 5.4.2 *The hybrid factor*

In this paragraph, the hybrid factor is discussed, aiming to examine future applications of the FSG with square loops, as an antenna feed. In reference [2], the importance of the hybrid factor is highlighted in determining the radiation from corrugated waveguides with circular cross section. The corrugated waveguide makes an excellent antenna feed, due to the ability to provide the hybrid  $HE_{11}$  mode with low cross-polar field components. This is possible if the transverse electric field lines are linearly polarised. For linear polarisation, the hybrid balanced condition must be satisfied and  $\beta/k$  to approach 1.

Assuming only the lowest order mode ( $p, q = 0$ ) propagates, the hybrid factor is defined as  $\Lambda = \frac{b_{00}^-}{a_{00}^-}$ . Hybrid balanced condition is reached when  $\Lambda \equiv 1$ . In Fig. 5.9 and Fig. 5.10,  $|\Lambda|$  is plotted against frequency for the first two hybrid modes of case B.

The hybrid factor for the  $EH_{11}$  starts from a relatively large value which is the case for modes with strong TE properties (for TE modes  $\Lambda \rightarrow -\infty$ , [2]). At resonance this value increases significantly as the FSS wall becomes totally reflective and the mode turns to a pure TE. After resonance, the hybrid factor for the mode decreases as attenuation increases.

For the  $HE_{11}$  mode, the hybrid factor has a small value near cut-off and exhibits strong TM properties (for TM modes  $\Lambda = 0$ , [2]). At resonance, the hybrid factor, drops to zero as the  $H_z$  component vanishes. Twice before resonance and once after resonance, the hybrid balanced condition is met. The ratio  $\beta/k$  after resonance is 0.5. Since the condition  $\beta/k = 1$  is not met, the advice is to increase the radius of the FSG, while keeping the periodicity and element dimensions. Thereby, lowering the cut-off of the  $HE_{11}$  mode whilst, keeping the same resonance. The latter is a suggestion for future work.

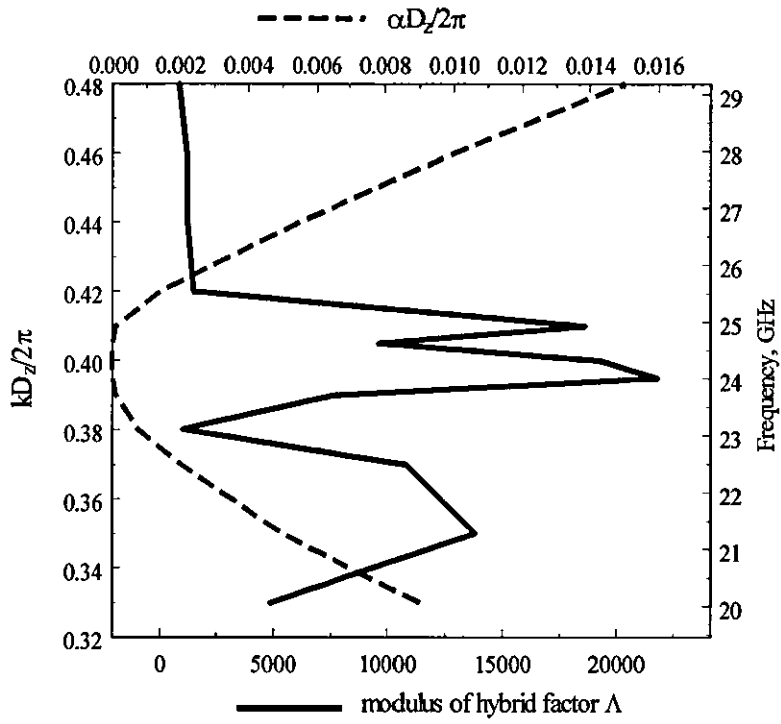


Figure 5.9 Hybrid factor for the  $EH_{11}$  mode

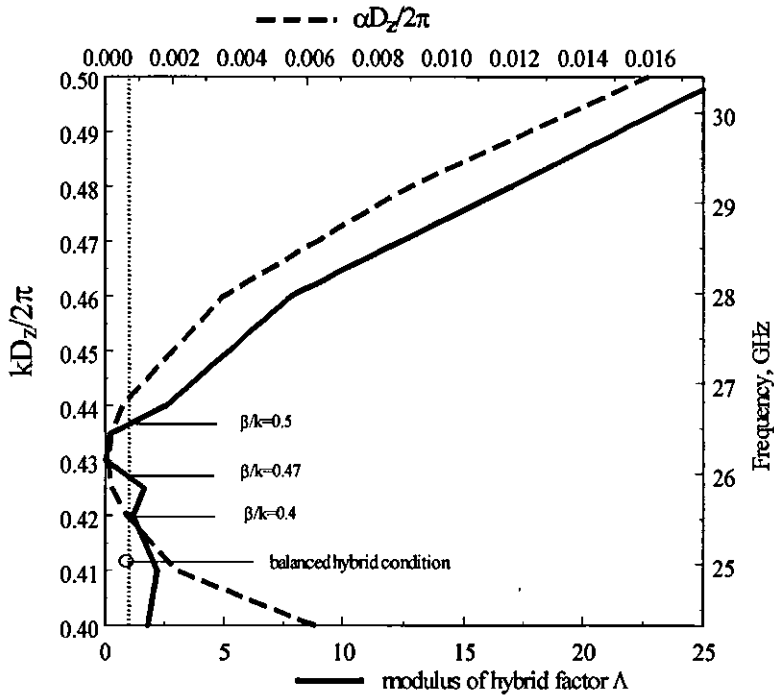


Figure 5.10 Hybrid factor for the  $HE_{11}$  mode

### 5.4.3 *Square loop results compared with results from dipole arrays*

In Fig. 5.11 the dispersion characteristics of two representative arrays are shown for comparison: one is with square loops and the other with dipoles. In each case, the periodicities in both  $z$  and  $\varphi$  are 8.22mm. The dipole length is equal to that of the square loop arm. It can be observed, that the cut-off of the first mode for the square loop geometry, is at lower frequencies compared to that of the dipole array. This is justified since, the array of square loops becomes resonant at  $L \cong \lambda_r / 3$  whilst, the array of dipoles resonates at wavelengths for which  $L \cong \lambda_r / 2$ . The effect is similar on the upper cut-off frequencies for the surface waves. For the square loop array, the surface wave stop band appears at a lower frequency than that of the dipole. What is most notable though, is the difference in the attenuation factor which is significantly smaller for the square loop array in the area near resonance. As more conductor is included in the area of the unit cell, it is reasonable to say that the approach of a complete wall for the square loops is better than that of the dipoles so, the guidance is better. Finally, due to the symmetry of the square loop, both the TE and TM polarisations are properly excited.



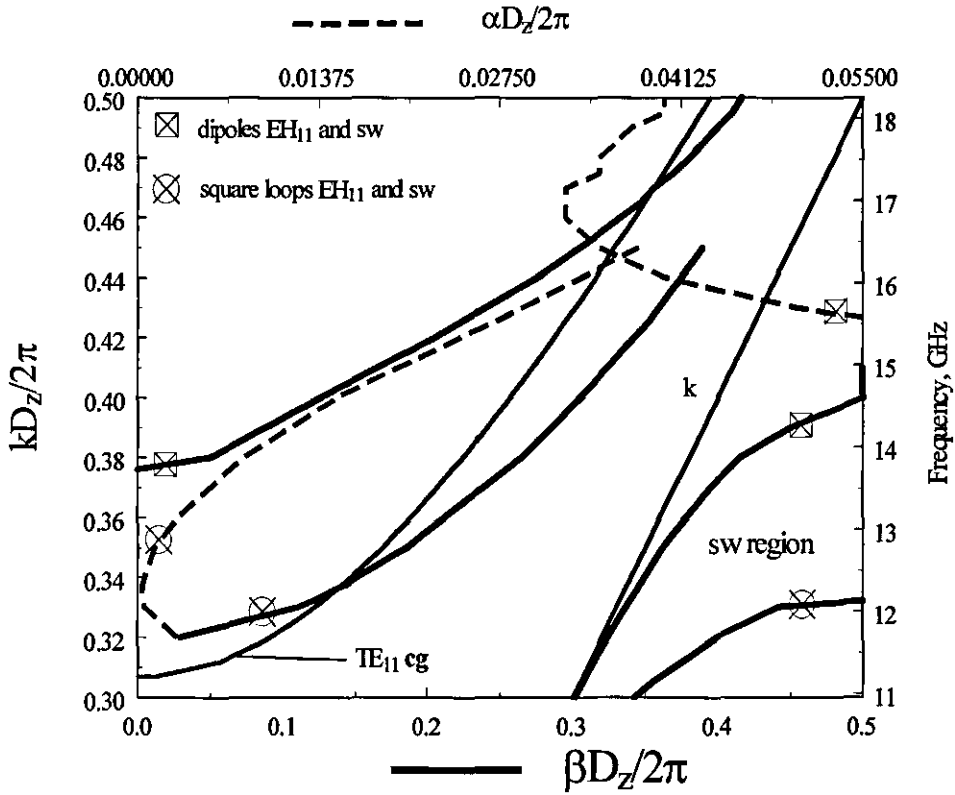


Figure 5.11: Dispersion diagrams for FSG with 6 square loops and those of 6 dipoles of same length in  $\phi$ . ( $D_\phi = D_z = 8.22\text{mm}$ ,  $r_0 = 7.85\text{mm}$ ,  $w = L/7$ ,  $D_z/\lambda = 0.4$ ,  $D_z/L = 1.05$ )

**5.4.4 Square loop array with different periodicity**

This Section aims to discuss the effects of the periodicity on the propagation, inside an FSG with square loops. The geometry is chosen so that 6 square loops can be fitted around the FSG circumference ( $D_z = 8.22\text{mm}$ ). There are two different sizes of elements. For the first, the ratio  $\frac{D_z}{L} = 1.05$  and the results are shown in Fig.

5.12. The second has a ratio  $\frac{D_z}{L} = 1.2$  whose results are shown in Fig. 5.13. In

both cases the width is  $w = \frac{L}{7}$  and  $r_0 = 7.85\text{mm}$ . Using observations from cases A

and B, the wavelength of resonance can be calculated beforehand according to  $\lambda_r = \frac{L}{3}$ . In so doing, the resonances are expected at 12.5 GHz, and 14.5 GHz for case A and B respectively (i.e. lowering of the resonance).

CASE C ( $D_z/L = 1.05$ )

Predicted results for the complex propagation constant of the first mode are shown in Fig. 5.12 for the frequencies between  $\frac{D_z}{\lambda} = 0.15$  to 0.45. The surface wave approaches an upper cut-off at 12.12 GHz and the resonance for the first guided/leaky  $EH_{11}$ , is at 12.23 GHz.

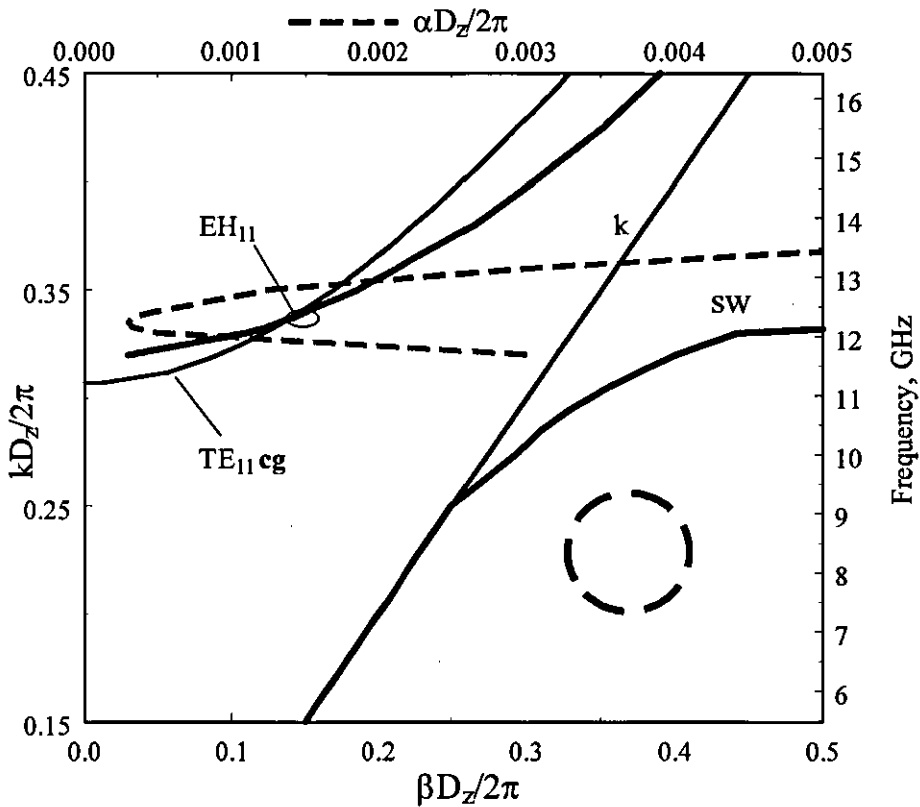


Figure 5.12: Dispersion diagrams for FSG with 6 square loops in  $\phi$ . ( $D_\phi = D_z = 8.22\text{mm}$ ,  $L = 7.82\text{mm}$   $r_0 = 7.85\text{mm}$ ,  $w = L/7$ ,  $D_z/\lambda = 0.4$ ).

CASE D ( $D_z/L = 1.2$ )

For this geometry, the stop band for the surface wave appears at 13.7 GHz. The resonance for the hybrid  $EH_{11}$  mode is at 14.9 GHz. At this frequency, the attenuation is small but not zero. Part of the  $\alpha$  curve (between point A and B) is shown in Fig 5.14, translated in  $\text{dBm}^{-1}$ . It is evident that even at resonance, there is still  $4.75 \text{ dBm}^{-1}$  radiation loss.

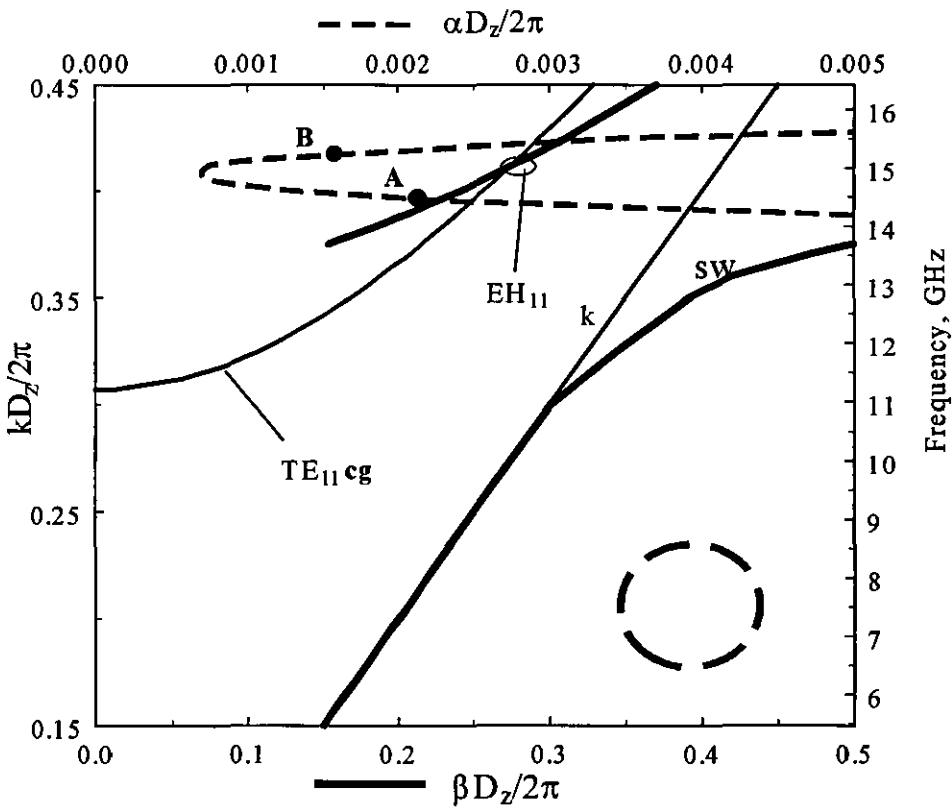


Figure 5.13: Dispersion diagrams for FSG with 6 square loops in  $\varphi$ .  
 ( $D_\varphi = D_z = 8.22\text{mm}$ ,  $L = 6.85\text{mm}$ ,  $r_0 = 7.85\text{mm}$ ,  $w = L/7$ ).

Finally, it is worth pointing out, that there is a good agreement between the predicted resonance and the one computed by the model.

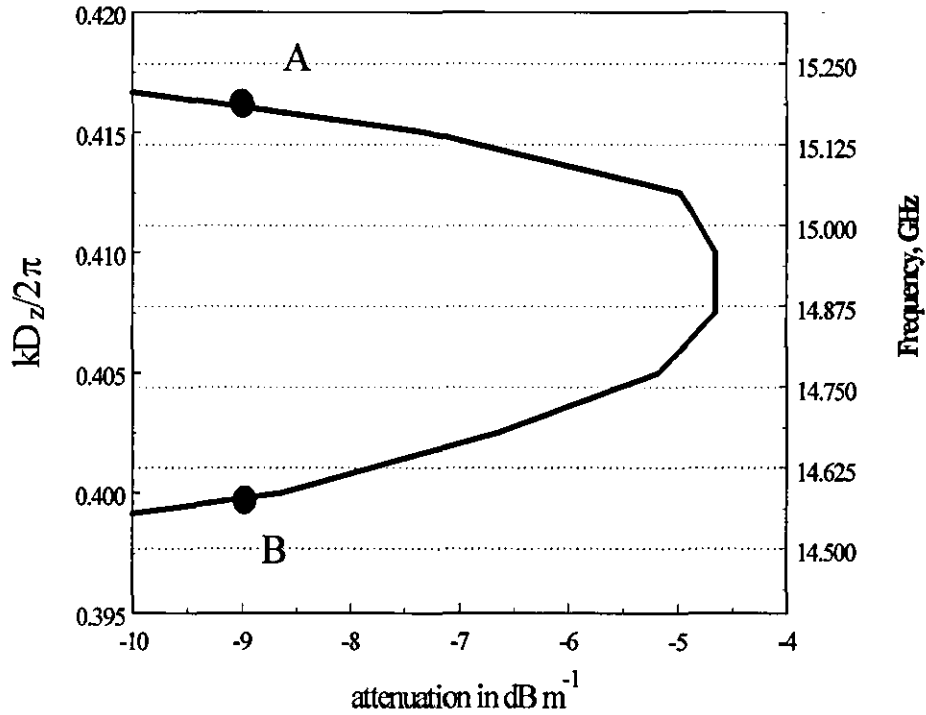


Figure 5.14 Attenuation in dBs per meter for the curve of Fig. 5.13 between points A and B.

#### 5.4.5 Measured results

In an attempt to validate some predicted results, an FSG was fabricated and measured in an anechoic chamber by a member of the Antennas and Microwaves Group at Loughborough University (see Acknowledgements). A *J*-band waveguide fed the FSG with a  $TE_{11}$  mode. The operating frequency range for the  $TE_{11}$  mode in the *J*-band is 12-16 GHz. Since, the resonance of the  $EH_{11}$  is at 15 GHz, for case D, the latter was chosen for testing. The square loop elements were printed through a lithographic process on a thin (.071mm) dielectric with dielectric constant  $\epsilon_r = 3$ .

The printed surface was rolled to a 7.85mm radius and 30cm long cylinder. There are 36 periodic cells included in that length and at least 12 wavelengths. It should be mentioned that in FSS studies, the analysis of surfaces of electric size greater than 10 wavelengths is carried out under the assumption that they are infinite in extent [3]. Fig. 5.15 shows the predicted and measured results for the propagation constant  $\beta$  and the attenuation constant  $\alpha$  for the excited  $\text{EH}_{11}$  mode. The results are normalised with respect to the periodicity. Measurements for  $\beta$  are obtained by measuring the angle of the main radiating lobe  $\theta$  and then use the relation  $\beta = k \sin \theta$ . It can be observed, that there is an excellent agreement between the predicted and measured results for  $\beta$ . In order to measure the attenuation, a short circuit was placed on the other end of the FSG. The reflected wave due to the short circuit, appears as a secondary lobe in the backward direction. The radiation  $N$  in dBs, of the secondary lobe at peak, was measured and the attenuation constant was obtained according to

$$N = e^{-\alpha l}$$

where  $l = 30\text{cm}$  is the length of the FSG. As illustrated in Fig. 5.15, the difference between the predicted and the measured resonant frequency is about 100 MHz. Other differences, occur for the values of the attenuation. It is evident that, throughout the frequency range, there is more leakage measured than predicted. This can be justified as follows 1) Manufacturing difficulties: it proves difficult to have an FSG where the radius is kept constant throughout its length and the structure to be perfectly curved. Other imperfections which occur in the process of printing the elements with the exact dimensions to those of the model. 2) Losses in the dielectric which are not taken into account by the model. Moreover, there is some energy scattered at the junction of the FSG with the feed. When a reflective surface was placed near the feed junctions, the receiving signal was stronger. 3) Inaccuracies of the model. Such inaccuracies may involve errors due to the truncation in the double summation of the number of bases, the number of Floquet terms and the approximation for the roof-top functions. Unfortunately, it is impractical to perform convergence tests properly as, the computing demands when the number of bases is increased are massive. 4) Inaccuracies of the measurements

at resonance. When the FSG is guiding, less energy radiates outside, so that the level of the reflected secondary lobe is very small. As seen in Fig. 5.15, there is a discrepancy in the measurements just after the resonant frequency.

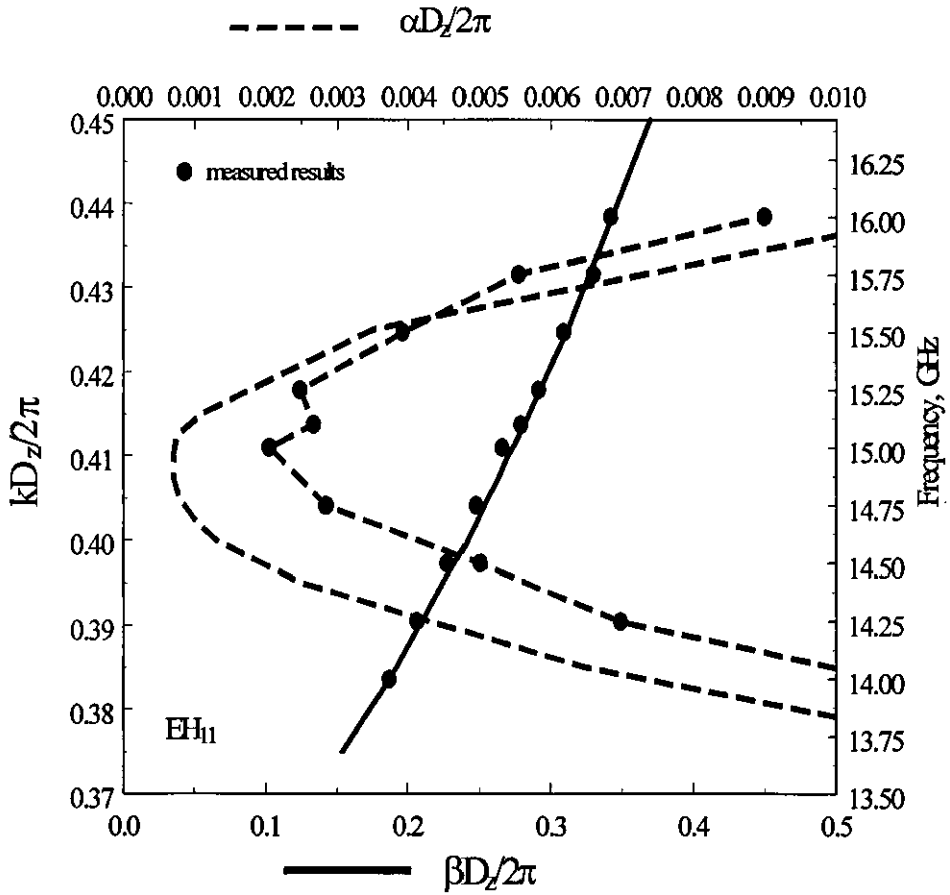


Figure 5.15: Measured and predicted results for the complex propagation constant for the FSG of case D.

### ***5.5 Conclusions***

In this Chapter, FSGs with square loop geometry have been studied. The theoretical model presented in Chapter 2 has been applied with the necessary modifications to the roof-top expansion to account for the more complicated element geometry. The efficiency of the model, in terms of computing requirements, is improved by introducing different sized roof- top functions. At low frequencies, the FSG behaves as a surface wave structure. Due to the periodicity, this surface wave stops propagating. Fast hybrid leaky wave modes can then carry the energy. There are frequencies where the FSS resonates and there is excellent guidance. The FSG can be designed to guide in a desirable frequency by choosing the correct element size. Additionally, the FSG is suitable to operate with two modes (one is guided and the other is radiating). For the  $HE_{11}$  mode, balanced hybrid condition is met in the area near resonance. To meet the condition for symmetrical mode pattern, it is advised to increase the radius.

*References*

- [1] RUBIN, B. and BERTONI, H. L.: 'Reflection from a periodically perforated plane using a subsectional current approximation', IEEE Trans. On Antennas Propagat., AP-31, No. 6, Nov. 1983, pp. 829-836.
- [2] CLARRICOATS, P. J. B., OLVER, A. D.: 'Corrugated horns for microwave antennas', Peter Peregrinus Ltd., 1984.
- [3] STYLIANOU, A.: 'Iterative computation of scattering from finite and multi-layer frequency selective surfaces', Ph. D. thesis, Loughborough University, June 1992.



# CHAPTER 6

## Conclusions and future considerations

In order to find the mode content of cylindrical FSGs, a boundary value problem was solved with two conditions. The first condition required that the structure is double periodic and the second, that the structure is open. By considering modal Floquet expansion and complex fields, the two former conditions became inclusive in the analysis. The fields were represented by space harmonics and in the inner region, each harmonic represented a localised standing wave. In the outer region, the space harmonics represented travelling waves. Other requirements were for the model to have an unlimited degree of freedom, in incorporating any element geometry. Therefore, the current on the conducting elements was expressed as a set of subdomain basis functions, the roof-top basis functions. Since the roof-top bases

represent current quantities over a small part of the conductor, accurate approximation of the current on any element can be achieved, by increasing the number of bases.

An eigen-value equation was derived by applying the electromagnetic boundary conditions in conjunction with a spectral representation of the current. Two systems of algebraic equations were obtained by applying MoM to the eigen-value equation. One system was solved for the complex propagation constant and the other for the currents and aperture fields. It became apparent from the analysis, that two important features required special attention:

1. The choice of the transverse wavenumber from the double value dispersion relation. Sometimes, the choice of the wavenumbers represents leaky waves which do not satisfy the radiation condition (improper solutions).
2. The use of asymptotic expansions for Bessel functions in order to overcome numerical difficulties.

The study began with modelling FSGs of infinitely long strips and transverse rings. Examining one dimensional cases proved useful, as it lessens the computational demands in understanding, the propagation inside cylindrical FSGs and the efficiency of the model. In pursuit of an easy to obtain solution, the imaginary part was removed from the complex propagation constant and the problem was solved for the real  $\beta$ . Numerical results for particular designs showed that the polarisation of the elements was dominating the type of the propagating modes. Longitudinal strips gave rise to hybrid modes with TM properties whereby, rings sustained the TE-like hybrid modes. Additionally, a TEM mode can propagate along the metal line of the strips whereas, the discontinuity due to the rings excites a surface wave. The values for  $\beta$  were not affected when the attenuation was searched for, mostly because the elements' separating distance was small compared to the wavelength. Solving for the attenuation, showed that the fast waves inside FSGs, radiate energy continuously, i.e. leaky wave antennas. The numerical stability for  $\beta - ja$ , was verified

by increasing the number of bases and the number of Floquet harmonics. The convergence for the propagation constant was easily accomplished whereas, the boundary condition checking proved that more currents and Floquet modes were needed to satisfy the condition.

Since this study aimed to serve, as a precursor to the study of FSGs with resonant elements, the effects of changing the periodicity and the strip widths were not examined and could be considered for future work.

The investigation, continued with FSGs with dipole elements. Results showed similar behaviour to the one dimensional case, as the less attenuated modes had the  $E$ -field parallel with the dipoles. In addition, a guiding region appeared due to the element resonance. The guidance can be reinforced by arranging the elements close to each other. As it is closely associated with the element's length, the guidance can be frequency controlled. Increasing the element's length, resulted in lowering the cut off frequencies of the modes. For the FSG with two dipoles in  $\phi$ , it was found that the  $TE_{11}$ -like mode, starts propagating at a lower frequency than that of a complete guide. For the FSG with  $z$ -dipoles, the periodicity was such that, both the zero and the first higher order mode became leaky at the same frequencies. In order to use the FSG for single beam scanning, the advice is to reduce the periodicity in  $z$ .

For the FSG with square loop elements dual polarisation is achieved at wave guidance. The simulations predicted a surface wave region, a guiding region and leaky wave regions. The predicted regions, agreed well with experimental knowledge for wave guidance in hollow rectangular tube made from an FSS with square loop elements. The guidance of the dominant  $EH_{11}$  mode is excellent at frequencies where the element resonates. The resonant wavelength can be predicted beforehand, since it was consistently as one third of the square loop arm. The resonant wavelength and the predicted values for the complex propagation constant agreed very well with measurements for a particular design. The next higher order mode, is the  $HE_{11}$  mode, which is also guided at a higher resonance. The FSG can

be used as an alternative to corrugated feeds provided, the  $HE_{11}$  mode is balanced. For the feed to be balanced, the hybrid factor should be 1, and the phase constant of the mode to approach the propagation constant in free space. The first condition was found to be satisfied but was met close to the cut off. A solution would be to increase the radius of the FSG and lower the cut-off frequency of the mode. If one needs to use the FSG simultaneously both as a guide and an antenna, bandwidths and band spacing ratios become important. The latter observations were not addressed quantitatively in this thesis and could be aspects of future work.

In terms of choosing the proper element and size geometry the answer is dependent on the application needs. This thesis showed that in terms of guidance the square loop element is superior to the dipole. However, dipole arrays can also find applications in leaky wave antennas and they are easier to model. For a dipole application, the advice would be the elements to be close to each other in order to lower the attenuation and avoid interference from grating lobes. Other considerations for future work, could begin with the calculation of the near fields or far fields, and the co-polar or cross-polar components, so as to evaluate a particular leaky wave antenna. A research project already has been initiated to study the feeding of the FSG and model the transitions of the fields in a junction.

# APPENDICES

***APPENDIX A General wave analysis in cylindrical co-ordinates:  
an overview***

From Maxwell's equations the electric and magnetic field intensities in a source free lossless and homogeneous medium can be expressed in terms of magnetic and electric vector potentials  $\underline{F}$  and  $\underline{A}$  respectively. Each one of these vector potentials satisfies the general vector wave equation [1,2]

$$\nabla(\nabla \cdot \underline{V}) - \nabla \times (\nabla \times \underline{V}) = -k^2 \underline{V} \quad (\text{A.1})$$

Where  $\underline{V}$  is either  $\underline{A}$  or  $\underline{F}$  and  $k$  is the wavenumber of the medium. TM or TE wave excitation in the  $z$  direction is defined, by assuming the only component of the above vector wave potentials, in the  $z$  direction of the standard cylindrical coordinate system  $\rho, \varphi, z$ . Then the wave equation is reduced to the scalar Helmholtz differential equation. The differential equation can be solved in the cylindrical coordinate system by the standard method of separating the variables. Solutions then take the form of a product which are the wave potentials. They represent cylindrical plane waves. Here, they are denoted as  $\Xi$  where,

$$\text{Helmoltz:} \quad (\nabla^2 + k^2)\Xi = 0$$

and

$$\Xi(\rho, \varphi, z) = B_n(\rho)\Psi(\varphi, z) \quad (\text{A.2})$$

Bessel functions represent the solutions in  $\rho$

$$B_n(k_\rho \rho)$$

$B_n(k_\rho \rho)$  for an unbounded media represents inward or outward travelling waves; for a closed structure it represents standing waves.  $\Psi(\varphi, z) = e^{jn\varphi} e^{-jk_z z}$  are plane

waves in  $\varphi$  and  $z$ . The solutions to the differential equation, must satisfy the dispersion relation defined as

$$k_\rho^2 = k^2 - k_z^2 \quad (\text{A.3})$$

must be satisfied.  $k = \frac{2\pi}{\lambda}$  is the free space wavenumber and  $k_\rho$  is the propagation constant along the radial axis  $\rho$  and is incorporated in the argument of the Bessels. It should be noted that all wave quantities expressed here are time varying as  $e^{-j\omega t}$ ; a factor which will be assumed from this point onwards. The electric and magnetic fields can now be written as a combination of TM and TE waves in the  $z$  direction

$$\underline{E} = \underline{E}_A^{(TM)} + \underline{E}_F^{(TE)} = -\nabla \times \underline{F} - j\omega\mu\underline{A} - \frac{j}{\omega\epsilon}\nabla(\nabla \cdot \underline{A}) \quad (\text{A.4})$$

In the above expression it is assumed that

$$\underline{A} = A_z \hat{u}_z \text{ and } \underline{F} = F_z \hat{u}_z$$

and

$$\underline{E} = E_\rho(\rho, \varphi, z) \hat{u}_\rho + E_\varphi(\rho, \varphi, z) \hat{u}_\varphi + E_z(\rho, \varphi, z) \hat{u}_z$$

The symbol  $\hat{u}$  denotes a unit vector. Solving (A.4) and separating  $\underline{E}$  to its component parts yields

$$E_z = -j\omega\mu A_z - j \frac{1}{\omega\epsilon} \frac{\partial^2 A_z}{\partial z^2} \quad (\text{A.5})$$

$$E_\varphi = \frac{\partial F_z}{\partial \rho} - j \frac{1}{\omega\epsilon\rho} \frac{\partial^2 A_z}{\partial \varphi \partial z} \quad (\text{A.6})$$

$$E_\rho = -\frac{1}{\rho} \frac{\partial F_z}{\partial \rho} - j \frac{1}{\omega\epsilon} \frac{\partial^2 A_z}{\partial \rho \partial z} \quad (\text{A.7})$$

Similarly

$$\underline{H} = \underline{H}_A + \underline{H}_F = \nabla \times \underline{A} - j\omega\varepsilon\underline{F} - \frac{j}{\omega\mu} \nabla(\nabla \cdot \underline{F}) \quad (\text{A.8})$$

So

$$H_z = -j\omega\varepsilon F_z - j \frac{1}{\omega\mu} \frac{\partial^2 F_z}{\partial z^2} \quad (\text{A.9})$$

$$H_\phi = -\frac{\partial A_z}{\partial \rho} - j \frac{1}{\omega\mu\rho} \frac{\partial^2 F_z}{\partial \phi \partial z} \quad (\text{A.10})$$

$$H_\rho = \frac{1}{\rho} \frac{\partial A_z}{\partial \rho} - j \frac{1}{\omega\mu} \frac{\partial^2 F_z}{\partial \rho \partial z} \quad (\text{A.11})$$

### References

- [1] BALANIS, C. A.: 'Advanced engineering electromagnetics', Wiley, N.Y. 1989.
- [2] HARRINGTON, R. F.: 'Time harmonic electromagnetic fields', Ch. 5, McGraw Hill, New York 1961.



### ***APPENDIX B: Grating lobes and mode coupling effect***

As already mentioned (Section 2.7), the radiation from an open structure which is also periodic, is solely associated with fast harmonics. At some frequencies these harmonics may become dominant. The number of the radiating beams equals the number of harmonics which satisfy the condition:

$$\left| \frac{k_{zq}}{k} \right| < 1 \quad (\text{B.1})$$

Moreover, the knowledge of the complex propagation can yield the angles of the radiating beams i.e. the angle  $\theta_q$  of the  $q^{\text{th}}$  radiating beam is found by the use of the approximate formula, [1]

$$\theta_q = \sin^{-1} \frac{k_{zq}}{k} \quad (\text{B.2})$$

$\theta_q$  is the angle of the peak of the beam measured from broadside as shown in Fig. B.1

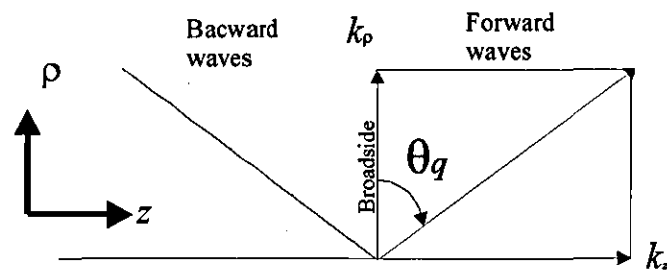


Figure B.1: Angle of the radiating lobe

There are frequencies where the spectral harmonics couple in pairs. As a result a higher cut-off occurs similar to that in a closed structure. For instance the -1 backward travelling harmonic propagates couples with the dominant forward travelling 0 harmonic when the condition  $|k_{z-1}| = |k_{z0}|$  is satisfied. The latter is met when  $\beta \frac{D_z}{2\pi} = 0.5$  and is referred as the Bragg condition. The condition  $k \frac{D_z}{2\pi} = 0.5$ , also is referred as Bragg condition. It defines a threshold frequency above which, higher order harmonics, may enter the visible spectrum (fast waves) and become dominant. The radiating beams which belong to higher order harmonics, are also referred as grating lobes or, higher order diffracted waves [2].

### *References*

- [1] COLLIN, R. E. and ZUCKER, F. J. E. 'Antenna Theory, Part 2', Ch. 19, Appendix B, McGraw-Hill, New York 1969.
- [2] LI, R. C. M. and OLINER, A. A.: 'Scattering resonances on a fast-wave structure', IEEE Trans. On Antennas Propagat., AP-13, No. 6, Nov. 1965, pp 948-959.

### ***APPENDIX C: Asymptotic expansions for Bessel functions***

According to numerical recipes the most powerful asymptotic expressions for the Bessel functions are the uniform asymptotic expansions. These expansions involve the use of Airy functions which in turn are difficult to evaluate. Instead, the Bessel functions can be written in terms of the modified Bessel functions of integer order and of complex argument [1]

$$I_{n_p}(z_q^-) = e^{-n_p \pi j / 2} J_{n_p}(j z_q^-) \quad -\pi < \arg z_q^- \leq \pi \quad (\text{C.1})$$

$$K_{n_p}(z_q^+) = -\frac{1}{2} \pi j e^{-n_p \pi / 2} H_{n_p}^{(2)}(-j z_q^+) \quad -\frac{\pi}{2} < \arg z_q^- \leq \pi \quad (\text{C.2})$$

In the previous expressions  $I$  and  $K$  are the modified Bessel functions of first kind.  $j$  is the imaginary unit number. According to step1 in Section 2.9, the Bessel functions are incorporated in the field coefficients by dividing all the relative expressions with the Bessel function. Therefore, the required asymptotic expressions are for the following ratios

$$\frac{J'_{n_p}(z_q^-)}{J_{n_p}(z_q^-)} \quad (\text{C.3})$$

and

$$\frac{H_{n_p}^{(2)}(z_q^+)}{H_{n_p}^{(2)}(z_q^+)} \quad (\text{C.4})$$

Following the relative properties of the Bessel function, Eqns. (C.3) and (C.4) can be written as

$$\frac{J'_{n_p}(z_q^-)}{J_{n_p}(z_q^-)} = -j \frac{I'_{n_p}(-jz_q^-)}{I_{n_p}(-jz_q^-)} \quad (\text{C.5})$$

The prime denotes the derivative of the Bessel (or modified Bessel) function with respect to the whole argument in parenthesis. According to [1]

$$\frac{I'_{n_p}(z)}{I_{n_p}(z)} = \frac{(1+z^2)^{1/2} \left\{ 1 + \sum_{l=1}^{\infty} \frac{v_l(t)}{n_p^l} \right\}}{z \left\{ 1 + \sum_{l=1}^{\infty} \frac{u_l(t)}{n_p^l} \right\}} \quad (\text{C.6})$$

Similarly, for the second order Hankel functions the connecting relation is

$$\frac{H_{n_p}^{(2)}(z_q^+)}{H_{n_p}^{(2)}(z_q^+)} = j \frac{K'_{n_p}(jz_q^+)}{K_{n_p}(jz_q^+)} \quad (\text{C.7})$$

and

$$\frac{K'_{n_p}(z)}{K_{n_p}(z)} = - \frac{(1+z^2)^{1/2} \left\{ 1 + \sum_{l=1}^{\infty} (-1)^l \frac{v_l(t)}{n_p^l} \right\}}{z \left\{ 1 + \sum_{l=1}^{\infty} (-1)^l \frac{u_l(t)}{n_p^l} \right\}} \quad (\text{C.8})$$

In the previous expressions  $z = \frac{-jz_q^-}{n_p}$  or  $z = \frac{-jz_q^+}{n_p}$  and both asymptotic

expressions hold for  $|\arg z| \leq \frac{1}{2}\pi - \varepsilon$ ,  $\varepsilon$  is an arbitrary positive number. Also

$t = 1/\sqrt{1+z^2}$ , and the polynomial components are defined up to the fourth order as

$$\begin{aligned}
u_0(t) &= 1 \\
u_1(t) &= (3t - 5t^3) / 24 \\
u_2(t) &= (81t^2 - 462t^4 + 385t^6) / 1152 \\
u_3(t) &= (30375t^3 - 369603t^5 + 765765t^7 - 425425t^9) / 414720 \\
v_0(t) &= 1 \\
v_1(t) &= (-9t + 7t^3) / 24 \\
v_2(t) &= (-135t^2 + 594t^4 - 455t^6) / 1152 \\
v_3(t) &= (-42525t^3 + 451737t^5 - 883575t^7 + 475475t^9) / 414720
\end{aligned} \tag{C.9}$$

The previous expressions can be tested against the values returned by the NAG routines, (within the NAG limits). Fig. C.1 shows the ratio  $asv/asr$  plotted (a) for large arguments and (b) large orders, where,

$$asv = \left| \frac{J'_{n_p}(z_q^-)}{J_{n_p}(z_q^-)} \right|$$

is calculated by asymptotic expansions for the Bessel functions, and

$$ngv = \left| \frac{J'_{n_p}(z_q^-)}{J_{n_p}(z_q^-)} \right|$$

is calculated by the appropriate NAG routine. As shown in Fig. C.1, the difference is negligible even when the order of the Bessel function is zero ( $n_p = 0$ ) or, when the argument of the function has the smallest value ( $q=0$ ). In both cases though, both the order and the argument are always within the calculating capacity of the NAG routines.

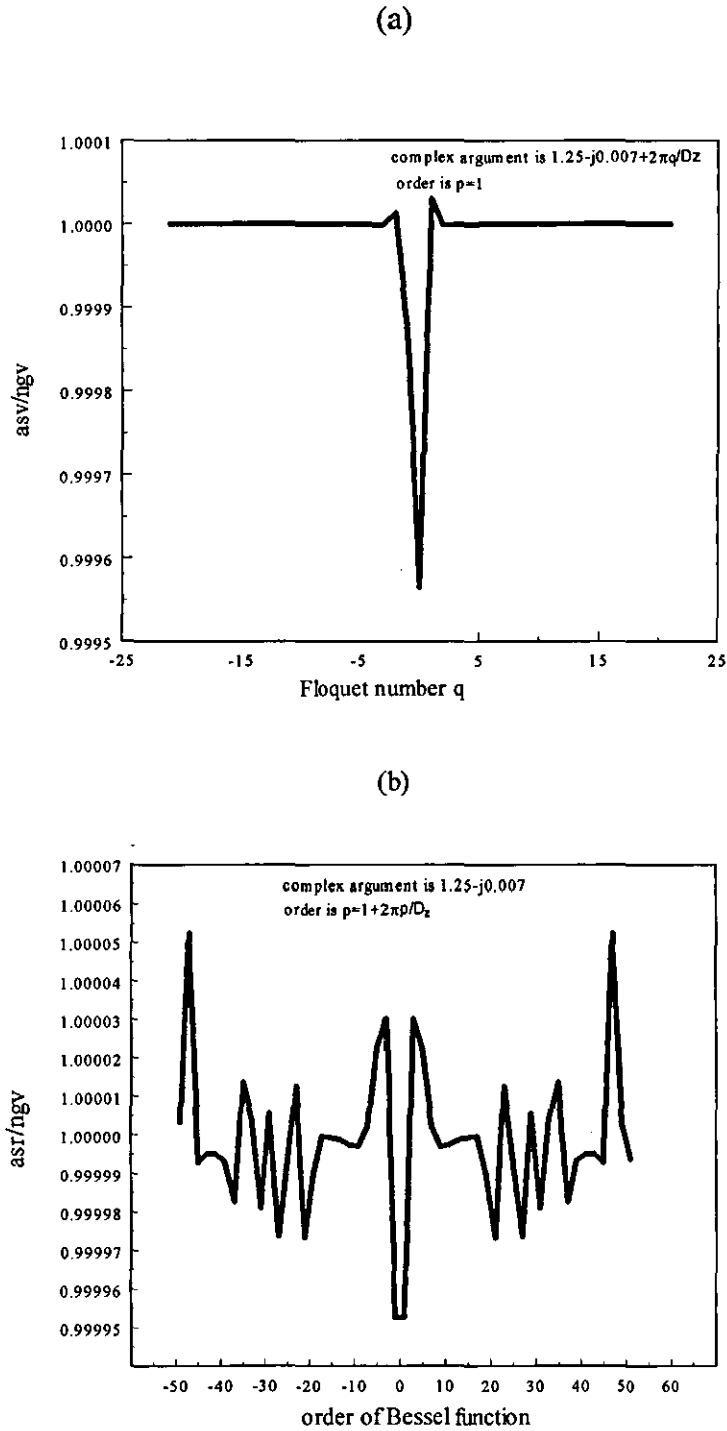


Figure C.1: Bessel functions (a) of large arguments and (b) of large orders calculated using asymptotic expansions and normalised to the values returned by the NAG routines. The argument values are calculated by the dispersion relation and for the parameters:  $D_z/\lambda = 0.4$ ,  $D_z = 8.22\text{mm}$ ,  $z_0 = 1.25 - j 0.007$ ,  $k_{z0} = (0.38 - j 0.004) k$ .

*References*

- [1] ABRAMOWITZ, M. and STEGUN, I.: 'Handbook of mathematical functions', Dover Publications, Inc., New York, 1954.

